Thermomagnetic Convection in a Differentially Heated Flow Loop

by
Mattias Stava

Master of Science
Thesis in Process Technology

Institute of Physics and Technology
University of Bergen

June 2020

Abstract

An electrically nonconductive colloidal suspension, where magnetic nanoparticles are dispersed in a carrier liquid, constitutes a ferrofluid. Ferrofluids have unique features, where the fluid properties can be altered. When a ferrofluid is exposed to a thermal gradient and an external magnetic field, the induced body force is not uniform over the whole magnetic field. This produces a thermomagnetic pumping force. This pumping force requires no moving parts and leads to a phenomenon called thermomagnetic convection. Thermomagnetic convection is mainly utilized in cooling applications where the ferrofluid is used as a heat transfer medium. However, these ferrofluid features also have potential in industrial or healthcare applications and have been of interest to many researchers.

The object of this thesis is to characterize the thermomagnetic convection through a flow loop in terms of finding the optimum fluid concentration and magnetic field strength. The experiments were conducted with the apparatus in two different orientations, horizontal and vertical. With the apparatus in a horizontal orientation, different applied thermal gradients were also investigated. A ferrofluid of low-cost is proposed in this thesis by the use of Fe_2O_3 nanoparticles, which possess strong magnetic properties.

The results from this study confirmed that the fluid flow of a ferrofluid could be controlled by the magnetic field and the thermal gradient. Additionally, a self-regulating feature was found, where the fluid velocity increased at a higher thermal gradient. This self-regulating feature can replace the need for sensors in applications where the fluid velocity must be controlled to obtain sufficient cooling.

With the apparatus in the vertical orientation, the fastest fluid velocity of 90.9 mm/s was obtained with a concentration 1.5 wt.% and a solenoid current of 1.26 A (2.3×10^4 A/m). If only natural convection had been present at this experimental case, the fluid velocity had been equal to 11.7 $\pm$ 2.2 mm/s. Thus, the fluid velocity from thermomagnetic convection increased by 676.9 $\pm$ 1.3 % compared to the fluid velocity from the natural convection.

With the apparatus in the horizontal orientation, the fastest fluid velocity of 13.06 $\pm$ 2.39 mm/s was obtained with a concentration of 2.0 wt.%, a solenoid current of 1.26A and a heat flux of 6961 W/m^2. This fluid velocity corresponds to the most substantial influence of thermomagnetic convection with the applied heat flux of 6961 W/m^2. With the applied heat flux of 5695 W/m^2, the fastest fluid velocity of 8.77 $\pm$ 1.40 mm/s was obtained with a concentration of 1.5 wt.% and a solenoid current of 1.26A. This corresponds to the most substantial influence of thermomagnetic convection with the latter applied heat flux.

Acknowledgments

I would like to express my gratitude and appreciation to my supervisors Professor Pawel J. Kosinski of the Department of Physics and Technology at University of Bergen, and Professor Boris V. Balakin of the Department of Mechanical and Marine Engineering at Western Norway University of Applied Sciences. Their genuine interest in the project, excellent guidance, useful comments and passionate participation has been remarkable. They were also very encouraging and helpful throughout the thesis.

I would also like to express my gratitude to friends and family, and the co-students Ørjan Strand, Marthe Braut, Lisbeth Espedal and Njål Frafjord for their support and contribution in useful discussions, which created a good working environment. A special thanks go to my girlfriend for her continuous encouragement during my studies.

My sincere thanks also go to Halvard Thon for his assistance with the production of ferrofluid, and the Malvern Mastersizer machine. Chief engineer Rachid Maad also deserves recognition for his technical support in the nanoparticle laboratory and interesting discussions.

Nomenclature

C_p	Specific heat capacity	[J/kg·K]
E	Total energy per unit mass	[J/kg]
H	Magnetic field intensity	[A/m]
I	Radiative heat flux	[W/m^2]
K	Anisotropy constant	[Jm^3]
K_{bend}	Characteristic bend coefficient.	
$L(\alpha)$	Langevin function	
M	Magnetization	[A/m]
P	Pressure	[Pa]
Q	Thermal power	[W]
Re	Reynolds number	
S_E	Energy source per unit volume	[J/m^3]
T	Temperature	[°C, K]
T_c	Curie temperature	[°C, K]
V	Volume	[m^3]
W	Energy of a particle	[J]
Z	Height/elevation	[m]
$\dot{m}$	Mass flow rate	[kg/s]
$\overline{f}_n$	Volume frequency	
d	Diameter	[m]

f	Friction factor	
f^{Kelvin}	Kelvin body force	[N/m^3]
f_0	Neel relaxation frequency constant	[GHz]
f_n	Number frequency	
g	Gravitational acceleration	[m/s^2]
k_b	Boltzmann's constant	[N·m·K^{-1}]
m	Magnitude of the magnetic dipole moment	[A·m^2]
n	Number density	[m^{-3}]
u	Velocity	[m/s]
x	Susceptibility	

Abbreviations

AMG	Algebraic multigrid
CFD	Computational Fluid Dynamics
CFL	Courant–Friedrichs–Lewy
DASC	Direct absorption solar collector
Emf	Electromotive force
FF	Ferrofluid
ID	Inner diameter
OD	Outer diameter
PSD	Particle size distribution
PTFE	Polytetrafluoreten
PVP	Polyvinylpyrrolidone
SDS	Sodium dodecyl sulfate
SLS	Static light scattering
STL	Stereolithography

Greek Symbols

η	Viscosity	[Pa·s]
Γ	Torque	[Nm]

μ_0	Vacuum permeability	$[4\pi \times 10^{-7}$ H/m]
ϕ	Magnetic volume fraction	
π		[3.14159]
ρ	Density	[kg/m^3]
σ	Stress tensor	[N/m^2]
τ	Relaxation time	[s]
θ	Angle	[rad]

Subscripts

B	Brownian
d	Domain
N	Neel
s	Saturation

Contents

Chapter 1

Introduction

1.1 Introduction

In almost all industries, the power density of electronic systems is increasing. For example, computers get more powerful and smaller. However, an increase in the power density in an electrical device causes the temperature of the device to increase, which limits the performance. Thus, the amount of power density increase in electrical devices is mainly thermally limited [33]. Many different thermal management solutions have been tested to address this problem. Regardless, the different proposes have usually come with reliability issues such as weight, space, cost, power density and maintenance drawbacks.

The use of a fluid to cool electric systems is well known and widely applied. Thermal management techniques, such as microjet and spray, have good cooling efficiency. A mechanical pump is required to circulate the fluid in these systems. This requirement introduces numerous downsides such as reliability and mechanical limitations, which include vibration, noise, leakage, power consumption and maintenance on moving parts.

Cooling systems without a mechanical pump are very promising in electronics, aerospace, and renewable energy. Field-induced flow systems have been attractive for researchers, due to no moving parts in the system. Field-induced flow systems obtain pumping force from interactions between electromagnetic fields and the fluid [52].

The study of various electromagnetic fields and fluid interactions are divided into three main categories [52]:

- Electrohydrodynamics

- Magnetohydrodynamics
- Ferrohydrodynamics

Electrohydrodynamics deals with electric force effects, which utilize the dielectric or Coulomb force acting on a low electrical conductivity fluid. Such systems have simple structures and no moving parts, but the system is limited to fluids with low electrical conductivity [68]. Magnetohydrodynamics deals with the interactions between magnetic fields and fluid conductors of electricity. When an electrical current flows at an angle to the direction of an applied magnetic field, the fluid experiences a force arising from the Lorentz force. Thus, the fluid in a magnetohydrodynamic system is limited to fluids with very high electrical conductivity [52][68]. Conversely, the choice of fluid in ferrohydrodynamics is not limited by the electrical conductivity.

Ferrohydrodynamics (FHD) describes the mechanics of fluid motion influenced by forces of magnetic polarization [52]. The magnetic polarization force produces the body force in FHD, which requires magnetizable material with an applied magnetic field gradient present. This body force is known as the Kelvin body force [49][7]. A simpler fluid control system design, which provides enhanced reliability, simplicity and compactness, has its basis from FHD [8][52]. This simpler control system design will be addressed below.

Motivated by the objective of converting heat to work with no moving parts, ferrohydrodynamics began to be developed in the early to mid-1960s. Over the years, colloidal magnetic fluids, also known as ferrofluids, became more available on the market and many other applications of these fluids with the effects from FHD were recognized. Thermomagnetic convection is one of these applications [52], which utilizes the temperature sensitivity of the FF under the presence of an applied magnetic field gradient.

When a colloidal mixture contains dispersed magnetic nanoparticles suspended in a nonmagnetic carrier fluid, it constitutes a fluid termed ferrofluid (FF) [8][45]. Magnetic nanoparticles have a nominal size between 1 and 100 nanometer [62], and typical substances are iron, cobalt, nickel, manganese, copper or zinc. Conventional liquid carriers are oil, kerosene, diester, hydrocarbon, fluorocarbon or water [52]. The FF is magnetized by an external applied magnetic field, which tends to align the magnetic dipole moment of the particles with the direction of the applied magnetic field. A stronger applied field causes more of the magnetic dipoles to be aligned with the direction of the field. Finally, all the magnetic dipoles are aligned with the field direction, and saturation magnetization is reached. Furthermore, an increase in fluid temperature causes a decrease in the magnetization because thermal agitation tends to disrupt the dipole moment alignment with the field. Thus, the strength of the magnetization depends on the applied magnetic field strength and fluid temperature [7][52][29]. The properties of the FF can also be altered by the external

magnetic field strength, such as thermal conductivity and viscosity, to achieve a specific design requirement [2].

When the FF has a temperature gradient and is in the presence of an applied magnetic field, it will experience a stronger magnetization in the low-temperature region than in the high-temperature region. This change in magnetization across the magnetic field gives rise to a net thermomagnetic driving force, which produces a fluid flow. The colder fluid will be driven towards the heated region. This is the principle of thermomagnetic convection [52].

Utilizing the FFs as a heat transfer medium is the main application of the phenomenon of thermomagnetic convection. In electromagnetic and electronic devices, FFs in the presence of a magnetic field gradient have been exploited to improve the heat transfer, due to the produced thermomagnetic convection [68][30][12]. In comparison to a mechanical pump, thermomagnetic convection requires no moving parts. This provides enhanced reliability, simplicity and compactness. A cooling system based on thermomagnetic convection is especially useful in remote and hazardous areas, where maintenance on a pump would have been difficult and expensive. Examples of such areas are subsea, offshore and space equipment. Thermomagnetic convection has a particular advantage for space applications, because natural convection cooling systems are not possible in space due to the absence of gravity [8].

The possibility of using FF in solar installations have been demonstrated in some research [44][3][11][10]. To harvest solar energy by the use of nanofluids, direct absorbing solar collectors (DASC) are used due to better efficiency compared to nondirect absorbing solar collectors. In DASC, solar radiation is absorbed by the particles within the fluid [3]. In addition to magnetic properties, FF has the flowability like other nanofluids and has improved thermal properties compared to the base fluid [9]. A significant number of studies report the thermomagnetic convection with FF in thermal systems without optical absorption of radiation [11]. Most of them are based on computational fluid dynamics [11]. Considering the efficiency of the photothermal light absorption, defined as a ratio of the harvested heat to the incident radiant heating, Balakin and Kutsenko [10] found that the absorption efficiency increased about 30% at the magnetic gradient of 240 kA/m^2 relative to the benchmark without magnetic effects. Alsaady et al. [3], investigated the effect of the FF Fe_2O_4 on a DASC. They found that using FF as a heat transfer fluid in combination with a magnetic field could increase the thermal efficiency with 12%. Additionally, they found that FFs showed much better efficiency than conventional heat transfer fluids at higher temperatures. However, they only used the magnetic field to alter the thermal properties of the FF, and a mechanical pump was used to produce fluid flow. To our knowledge, the possibility of utilizing the phenomenon of magnetic convection to obtain fluid flow in a DASC has not yet been investigated. Thus, further research on characterizing the thermomagnetic convection with optical

absorption of radiation is needed.

Several numerical and experimental studies on thermomagnetic convection of FFs have been conducted [69][12][67][41][38][8][33][13]. Research on cooling applications which utilizes thermomagnetic convection are promising and has made progress. Nevertheless, more investigation of these systems are needed, to achieve proper correlation between the imposed magnetic field, the fluid flow and the temperature distribution of the FF [9][45]. Different FFs have been investigated to achieve optimum performance, but they are often industrial limited due to the high cost [60].

In this thesis, an investigation was first done on a thermomagnetic cooling system where natural convection was present. Secondly, an investigation was done on a DASC with thermomagnetic convection and no natural convection present. The objective in both investigations was to characterize the thermomagnetic convection in a differentially heated flow loop, to achieve a proper correlation between the imposed magnetic field, the fluid flow and the temperature distribution of the FF. The performance of the former and latter system was determined from recorded temperatures of the system, which was used to calculate the corresponding velocity of the fluid flow. Both analytical calculation and numerical simulation have been used to estimate the fluid velocity. The operated FF was decided to be Fe_2O_3-water, as an alternative to the more expensive industrial limited FFs. Regardless, Fe_2O_3 possesses strong magnetic properties and enhanced thermal properties compared to the base fluid (water). In addition, few researchers have investigated the use of the FF Fe_2O_3-water in such systems [60].

1.2 Specific objectives

The specific objectives of this thesis were to:

- Design an experimental lab set-up.
- Investigate the stability of the FF, when it comes to chemical additives and concentration.
- Investigate how the FF concentration and magnetic field strength influenced the thermomagnetic convection, while natural convection was present. The focus was:
  - Measured temperature differences.
  - Estimated fluid velocity from both analytical calculations and computational fluid dynamics.
- Investigate how the FF concentration, magnetic field strength and the applied heat flux influenced the thermomagnetic convection, while no natural convection was present. The focus was:
  - Measured temperature differences.
  - Estimated fluid velocity from analytical calculations.

Chapter 2

General Theory

2.1 Nanoparticles and Nanofluids

Nanoparticles are particles with nominal size between 1 and 100 nm [62]. The particles consist of closely packed atoms, often arranged into a spherical assembly. Nanofluids are composed of a suspension of these particles in a base fluid. The base fluid is usually water, oil or glycol. The use of surfactants is common to prevent settling and clumping of particles [8]. Nanofluids have superior thermophysical properties with improved conductive and convective heat transfer properties, compared with the base fluid [8][31][51]. Consequently, there has been a rapid growth in research articles about nanofluids [62] since they were proposed by Choi and Eastman [17] in 1995.

Nanofluids have unique features which are different from fluid dispersion of millimetre or micrometre sized particles [5]. Due to decreased particle size, the surface-to-volume ratio becomes larger. This improves the thermal properties and the suspension stability [70][53][57]. Thus, nanofluids are beneficial for heat transfer applications [5][54].

2.2 Ferrofluids

When a colloidal mixture contains dispersed magnetic nanoparticles suspended in a nonmagnetic carrier fluid, it constitutes a category of nanofluid called ferrofluid (FF) [8][45]. These FFs differ from nanofluids by their magnetic properties and thermo-physical characteristics. Properties such as thermal conductivity, viscosity and thermomagnetic convection can be controlled and optimized by an external magnetic field [2]. FF has enhanced stability compared with fluids of larger magnetic particles (μm or mm), and will not undergo large changes in rheological properties

(i.e. liquid to solid transition) during exposure of an external magnetic field. The FF will consequently remain flowable in the presence of a magnetic field, even when the magnetic field is increased to the point where the FF reaches magnetic saturation [52].

The suspended particles in FFs are single domain nano-scaled magnetic particles (constant magnetization across the particle) [32], and can consist of a broad range of either ferro- or ferrimagnetic materials. Ferrite particles are often used to create FFs, and are a class of ferromagnetic materials represented by the general formula $M^{2+}OFE^{3+}O_3$. The letter M represents a metal such as iron, cobalt, nickel, manganese, copper, zinc or a combination of them [30]. A range of properties for the FF can be obtained through the choice of different metal particles [52]. Because of the single-domain nanoparticles, the FFs will have a magnetic behaviour termed superparamagnetism. In a low magnetic field, superparamagnetic fluids are magnetized to a greater extent compared to paramagnetic fluids [52]. Hence, their magnetic susceptibility is larger than for paramagnetic fluids.

There are several methods to prepare nanofluids, but they can mainly be categorized into either a one-step or two-step process [61]. The one-step process consists of simultaneously producing and dispersing the particles in the base fluid. The FF is synthesized to the desired volume fraction and particle size [71][61]. This method does not require the procedure of drying, storage, transportation and dispersion of nanoparticles. The agglomeration of nanoparticles is minimized, and it is an increase in the fluid stability [37]. The most significant disadvantage for this method is the impurities that will exist in the FF because of incomplete reaction or stabilization [71]. In the two-step method, nanoparticles are first produced as a dry powder by chemical or physical processes to a preferred size and shape. Next, the particles are dispersed into the base fluid at the desired volume fraction. Intensive magnetic force agitation, ultrasonic agitation, high-shear mixing, homogenizing and ball milling are normally used, to enhance particle mixing. The result will be a cleaner FF with fewer impurities, but the process is more energy-consuming. Since the industry has already scaled up the nanopowder synthesis techniques, this two-step process is more economical and more used than the one-step process [5]. A significant drawback of this process is that the particles easier aggregate, due to the high surface area and surface activity.

2.3 Physical properties

This section describes some physical properties of great importance, regard to formulating and interpreting the hydrodynamic description of FFs. Some physical properties that have evident influence are magnetization change in a field of shifting orientation or intensity and shear stress versus the rate of strain (viscosity) [52][2].

2.3.1 Magnetization

FF samples consist of a collection of individual single-domain ferromagnetic particles, each with its embedded magnetic dipole moment. Ideally, there is no interaction between the particles in a FF. The particles are randomly oriented in the absence of an applied magnetic field, and the net magnetization of the FF is zero. When a magnetic field is applied, the direction of the magnetic dipole moment of the particles will attempt to be parallel to the applied magnetic field direction. This is described by the magnetic dipole moment that rotates towards the minimum energy direction, which is parallel to the magnetic field. However, the thermal agitation tends to partially overcome this parallel alignment for low or moderate magnetic field strengths [52]. The number of particles that are parallel aligned with the magnetic field increases with increasing magnetic field strength. The fluid magnetization is the density of magnetic dipole moments that are aligned with the magnetic field direction. All of the particles will be completely parallel aligned to the magnetic field at very high magnetic field strength, and saturation magnetization (M_s) is reached.

FFs will have a magnetic behaviour termed superparamagnetism. Superparamagnetic fluids will have a larger magnetization in a low magnetic field compared with paramagnetic fluids [52]. Langevin's classical theory is adopted to describe superparamagnetic relationships. It describes the magnetization as a function of the magnetic field. Negligible particle-particle magnetic interaction was assumed [52][22].

The magnitude of the magnetic dipole moment is defined as the domain magnetization of the bulk material multiplied by the volume of the particle. If spherical particles are assumed, the magnetic dipole moment is [52][22]:

$$m = M_d V = M_d \frac{1}{6} \pi d^3, \tag{2.1}$$

where m and M_d is the magnitude of the magnetic dipole moment and the domain magnetization of the material, respectively. The energy of the particle is found by stating that the required mechanical work to rotate a particle an angle θ, is equal the energy of the particle [52][22]:

$$W = \int_0^\theta \vec{\Gamma}\, d\theta = \mu_0 m H \int_0^\theta \sin\theta\, d\theta = \mu_0 m H (1 - \cos\theta). \tag{2.2}$$

Here, W and Γ are the energy of the particle and torque respectively. The magnetic dipole moment tends to align itself with the magnetic field. The thermal energy counteracts this behaviour and randomizes the spatial orientation. Thermodynamics describes this situation by using Boltzmann statistics [52]:

$$n = e^{-W/k_B T}, \tag{2.3}$$

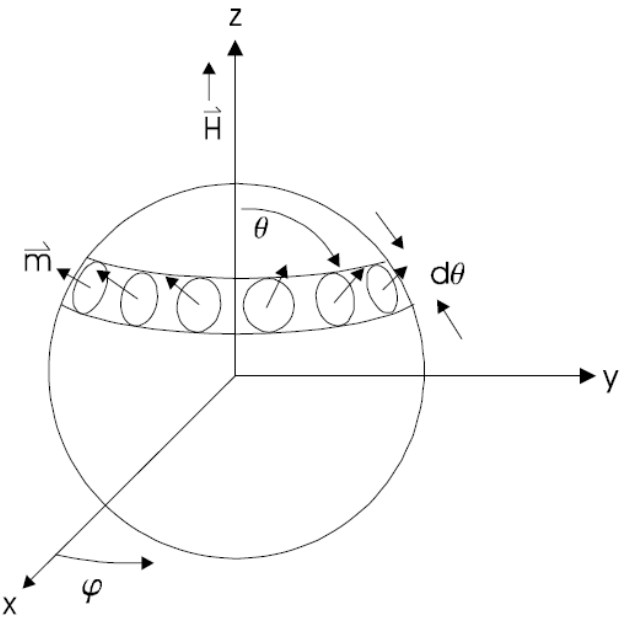

Figure 2.1: Sphere with radius R, enclosing dipoles who contribute to the net magnetization of a body [22].

where n is the number density of dipoles, k_B is Boltzmann's constant and T is the temperature in kelvin. By substituting Eq. (2.2) into Eq. (2.3), gives the following equation for the number density of dipoles:

$$n = e^{-\mu_0 mH/k_B T} e^{\mu_0 mH\cos\theta/k_B T} = n_0 e^{\mu_0 mH\cos\theta/k_B T}, \tag{2.4}$$

where $n_0 = e^{-\mu_0 mH/k_B T}$ is the amplitude of the number density of the magnetic dipoles when the magnetic field is zero [52].

From Figure 2.1, the magnetic dipole moment in the x and y-direction over the sphere will cancel each other out. The magnetic dipole moment and subsequently, the net magnetization will be parallel to the direction of the applied magnetic field, in this case, the z-direction. The magnetization of the z-direction M_z is expressed by the differential expression [22]:

$$dM_z = \frac{mn}{\frac{4}{3}\pi R^3}\cos\theta r^2 \sin\theta \; dr d\theta d\varphi. \tag{2.5}$$

By substituting n defined in Eq.(2.4) into Eq.(2.5) and integrating over the volume of the sphere, the Langevin function for superparamagnetic magnetization behaviour of a FF is obtained:

$$\frac{M}{\phi M_d} = \frac{M}{M_s} = L(\alpha) = \coth\alpha - \frac{1}{\alpha}, \quad (\alpha = \frac{\mu_0 mH}{k_B T}). \tag{2.6}$$

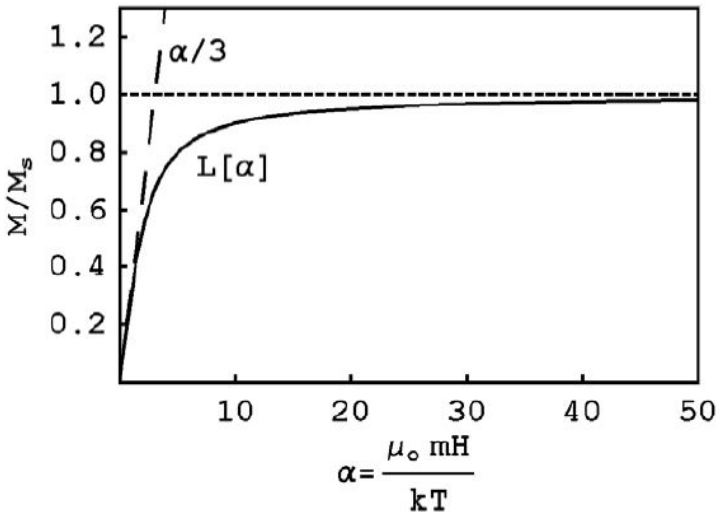

Figure 2.2: Low-field and high-field asymptotes plottet from the theoretical Langevin equation (2.6).

The magnetization M of the FF has a direction parallel to the applied magnetic field. ϕ is the magnetic volume fraction, described by the ratio of the volume of magnetic particles to the volume of the liquid carrier. M_d is the domain magnetization of the bulk magnetic particle, and $M_s = \phi M_d$ is the saturation magnetization of the FF. The low-field and high-field asymptotes of the Langevin equation (2.6) can be seen in Figure 2.2, and is written by using Taylor series expansion valid for small and large values of α respectively [22]:

$$\lim_{\alpha \to 0} L(\alpha) = \frac{M}{M_s} \approx \frac{\alpha}{3} = \frac{\pi \mu_0 M_d H d^3}{18 k_B T}, \tag{2.7}$$

$$\lim_{\alpha \to \infty} L(\alpha) = \frac{M}{M_s} = 1 - \frac{1}{\alpha} = \left(1 - \frac{6 k_B T}{\pi \mu_0 M_d H d^3}\right). \tag{2.8}$$

Eq. (2.7) and Eq. (2.8) implies that the magnetization of a FF is a function of the external magnetic field strength and the temperature, and is showed in Figure 2.2.

2.3.2 Susceptibility

The low field asymptotes of the Langevin equation (2.7) express a linear relationship between the magnetization M and the field H. The initial slope of the magnetization curve in Figure 2.2, is defined as the magnetic susceptibility x, which is described

in Eq. (2.9).

$$x = \frac{M}{H} = \frac{\pi\mu_0 M_d M_s d^3}{18k_B T} = \frac{\pi\mu_0\phi M_d^2 d^3}{18k_b T} \tag{2.9}$$

The initial magnetic susceptibility measures the magnetic response of a material in an applied magnetic field of low strengths [26][52]. All materials have magnetic susceptibility, where paramagnetic materials have positive values, and diamagnetic materials have negative values. A large value of x gives a strong material magnetic response when affected by a magnetic field. Conversely, a small value of x gives a weak material magnetic response when affected by the same magnetic field. Examination of Eq. (2.9) has concluded that the same approximation is accurate for high temperatures [52][22][33]. In addition to temperature, the volume fraction of magnetic particles ϕ and the size of the particle d will have a significant impact on the initial magnetic susceptibility.

2.3.3 Relaxation mechanisms

The magnetic moment in the FF can be relaxed (rotated) into parallel alignment with the magnetic field by two distinct mechanisms. This happens after the applied magnetic field is changed. The first mechanism is Brownian relaxation, where the relaxation occurs by physical rotation of the particle in the fluid. This mechanism is dominant at larger particle sizes. The second mechanism is Neel relaxation, where the relaxation occurs due to rotation of the magnetic moment vector within the particle [66][52]. The latter mechanism is more dominant at smaller particle sizes. Brownian- and Neel rotation are shown in Figure 2.3.

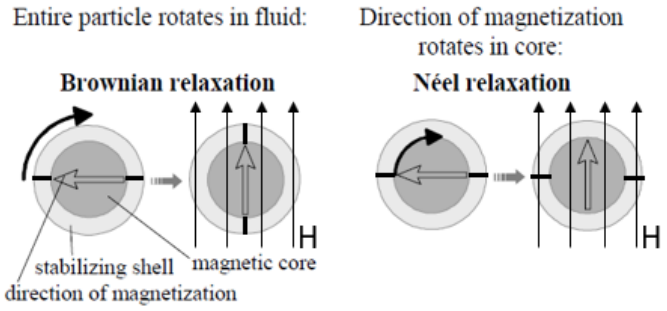

Figure 2.3: Magnetic Relaxation Mechanism [66].

The Brownian relaxation time (τ_B) and Neel relaxation time (τ_N) are the time it takes to rotate the magnetic moment of the particle for each mechanism, respectively. Regardless of which mechanism is the fastest, the Brownian and Neel mechanism will lead to a superparamagnetic behaviour in a FF [52]. The former and latter relaxation times are combined in an effective relaxation time (τ). They are all

presented under [64]:

$$\tau_B = \frac{3V\eta_0}{k_B T} \qquad \text{(Brownian relaxation time)}, \tag{2.10}$$

$$\tau_N = \frac{1}{f_0} \exp\left(\frac{KV}{k_B T}\right) \qquad \text{(Neel relaxation time)}, \tag{2.11}$$

$$\frac{1}{\tau} = \frac{1}{\tau_B} + \frac{1}{\tau_N}. \tag{2.12}$$

Here, V is the particle volume (m^3), η the viscosity of the carrier liquid (Pa·s), f_0 the frequency constant of Neel relaxation (10^9 Hz) and K the anisotropy constant of the material. The Brownian and the Neel relaxation time are strongly dependent on the particle size and temperature. Smaller particles or higher temperatures provide faster relaxation times.

2.3.4 Curie Temperature

As the temperature increases in a magnetic material, the ferromagnetic alignment of the magnetic moment is broken by thermal fluctuation. When the temperature has reached the Curie temperature T_c, net magnetization decrease to zero and undergoes a transition to paramagnetic behaviour [14][29]. A FF is composed of very small magnetic nanoparticles which only contains a single magnetic domain. Because there is only one single magnetic domain, a disordering of the magnetic moment within the particle by thermal fluctuation will not influence the magnetic domain in the particle. However, thermal fluctuation can distort the alignment between adjacent particles. Thus, a FF will undergo the same demagnetization with increasing temperature. The behaviour is illustrated in Figure 2.4.

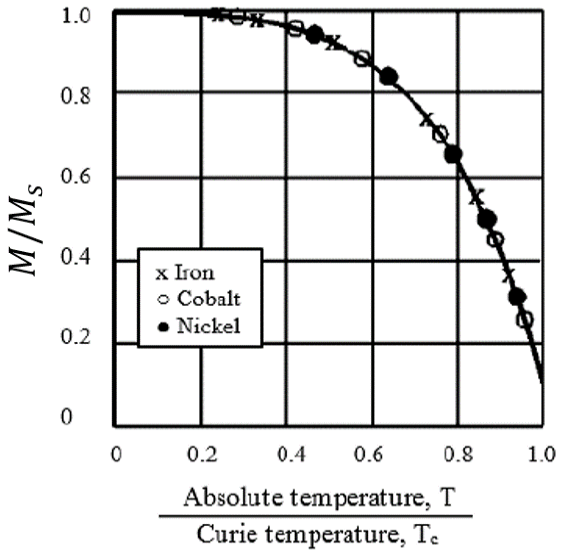

Figure 2.4: Degradation in magnetization as a function of temperature.

2.3.5 Viscosity

When a FF is exposed to a magnetic field, it will remain flowable even at the point where the magnetization of the FF reaches saturation. Nevertheless, the presence of the magnetic field alters the rheology and thermal conductivity of the FF [52][43]. The viscosity will first be discussed in the absence, then in the presence of an applied magnetic field.

In the absence of an applied magnetic field
FFs have a higher viscosity than the original carrier fluid itself. This yields for both cases where the magnetic field is either absent or present. The increased viscosity is described in the same way as for nonmagnetic colloids of solid particles suspended in liquids. The suspended solid particles lead to an increased rate of energy dissipation during viscous flow. Hence, theoretical models for describing the viscosity is available and was first established by Einstein, known as Einstein equation [52][43]:

$$\frac{\eta}{\eta_0} = 1 + \frac{5}{2}\phi. \tag{2.13}$$

The Einstein equation (2.13) expresses the ratio of the mixture viscosity η and the carrier fluid viscosity η_0 as a function of the solids particle fraction ϕ. This relationship is only valid for small concentrations ($\phi \leqslant 5\%$).

In the presence of an applied magnetic field
When an external magnetic field is applied on a FF, an increase in the viscosity

is discovered. The viscosity increase is dependent on the field strength and the direction of the field. The viscosity increase is described by the obstruction of free rotation of the suspended particles in the flow due to the magnetic field [46][24]. The viscosity increase in the FF is more significant with larger particles [22][33].

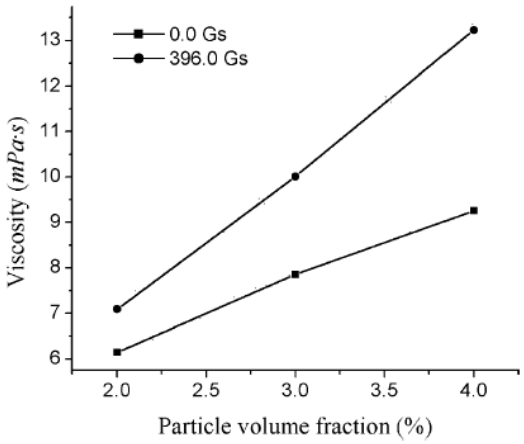

Figure 2.5: Dependence of the viscosity on the particles volume fraction [36].

In a fluid flow with vorticity, the particles will rotate due to the influence of shear force. A magnetic field will cause the particles magnetic moment to line up with the field direction. This change in magnetic moment direction occurs because the particles want to minimize their alignment energy. When the magnetic field direction and the fluid vorticity direction are parallel, the particles can rotate freely, and magnetism exerts a small influence on the viscosity. However, when the directions are perpendicular, the particles magnetic moment tries to be parallel with the magnetic field, to minimize their alignment energy. Furthermore, a mechanical torque arising from the shear force will try to counteract this alignment between the magnetic field and magnetic moment. The competition between the mechanical and magnetic torque gives rise to a hindrance of free rotation of the particles in the fluid flow. As a result, the resistance of fluid flow enhances, and the fluid viscosity increases [55][43][24][46].

There is no sophisticated and accepted theory for accurately predicting the viscosity and thermal conductivity for a FF exposed to an applied magnetic field. Experiments are necessary to determine these parameters [36]. To get insight into how the viscosity change with an applied field, experimental results for the water-based FF Fe_3O_4 are presented [36]. The average particle diameter of the FF is 26 nm. Different properties of the FF with corresponding graphs are reviewed and discussed below:

Particles volume fraction. By adding nanoparticles to the carrier liquid, the viscos-

ity of the fluid will increase, regardless of whether the magnetic field is applied or not. The particle volume fraction is one of the main factors concerning the viscosity of a FF. The extra suspended particles in the fluid causes an increase in the energy dissipation rate during viscous flow [52][36][33]. The effects of particle volume fraction on the viscosity for the FF Fe_3O_4 in the absence and the presence of a parallel magnetic field are presented in Figure 2.5.

Magnetic field strength and direction. From the experimental results in Figure 2.6 and 2.7, it is seen that the viscosity increases with the strength of the applied magnetic field. This is the case for both parallel and perpendicular field direction to the flow. When the magnetic field was perpendicular to the flow, the viscosity increased to a greater extent. This corresponds to the explanation given earlier. At higher volume fractions of magnetic particles, the viscosity increased to a greater extent due to a magnetic field. The relative viscosity in Figure 2.6 and 2.7 refers to the ratio of the FF viscosity in the presence of a magnetic field and the FF viscosity in the absence of a magnetic field [36].

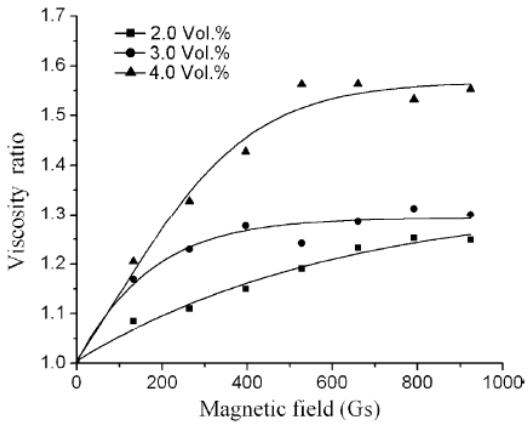

Figure 2.6: Relative viscosity of the FF Fe_3O_4 with parallel magnetic field to the flow [36].

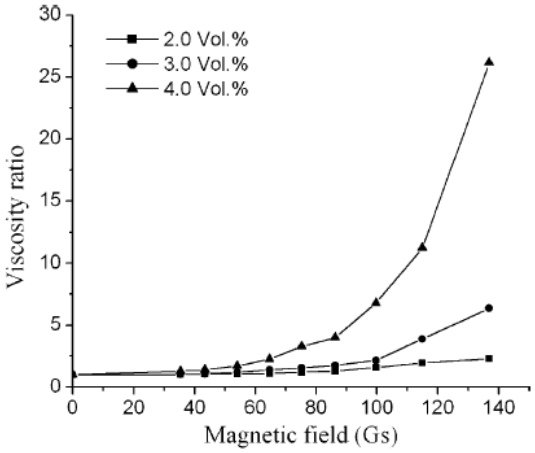

Figure 2.7: Relative viscosity of the FF Fe_3O_4 with perpendicular field to the flow [36].

2.3.6 Effective thermal conductivity

FFs will have enhanced conductivity compared to their carrier fluid without particles, in both the absence and presence of an external magnetic field. An important factor affecting the thermal conductivity is the particle volume fraction. When an applied magnetic field is perpendicular to the temperature gradient, almost no change in the thermal conductivity is found. Conversely, when the magnetic field direction is parallel with the temperature gradient leads to an increase in the thermal conductivity as a function of the magnetic field strength [36][50][2][45]. According to Philip et al. [2], the effective thermal conductivity of a FF could be increased

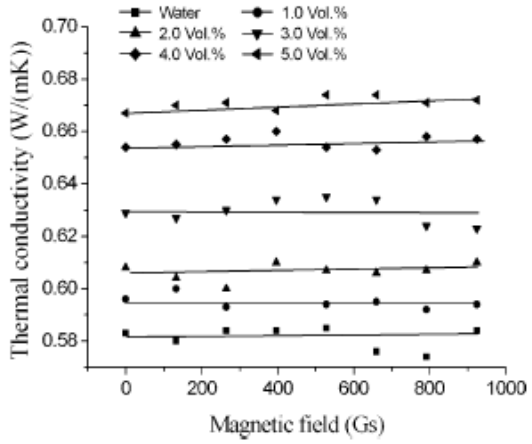

Figure 2.8: Thermal conductivity variation of the FF Fe_3O_4, experiencing a magnetic field perpendicular to the temperature gradient [36].

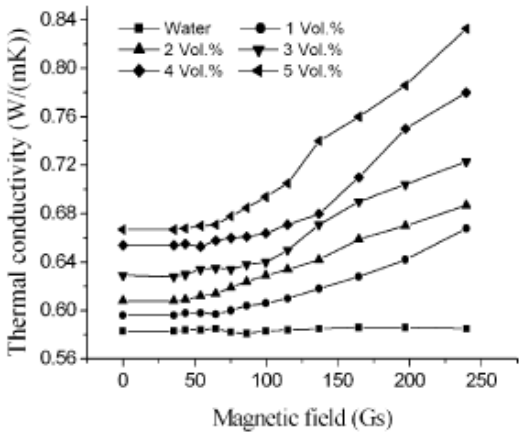

Figure 2.9: Thermal conductivity variation of the FF Fe_3O_4, experiencing a magnetic field parallel to the temperature gradient [36].

by 300%. Figures 2.8 and 2.9 visualize how an applied magnetic field affects the thermal conductivity differently based on the direction of the field [36].

The enhancement in thermal conductivity in Figure 2.9 is explained due to the generated aggregates of particles that appear during exposure of a magnetic field parallel to the temperature gradient. These aggregates form highly conductive paths for heat transfer, because the heat is transferred faster in solid particles than in the carrier fluid. Hence, the field causes the particles to form doublets, triplets and short chains along the direction of the magnetic field. The length of the chain increases with the field intensity and consequently reduces the Brownian motion. Additionally, the spacing between the particles within the chain decrease as the magnetic field intensity increase. When the field direction is parallel to the temperature gradient, chain structures are generated in the same direction parallel to the temperature gradient and provides an effective bridge for energy transportation along the temperature gradient. It should be noted that the thermal conductivity increase due to the presence of a magnetic field, is more remarkable at higher particle concentrations [36][45][2][50].

2.4 Thermomagnetic convection

Ferrohydrodynamics explains the fluid dynamic and heat transfer processes for a homogeneous and incompressible FF in motion during exposure of an applied magnetic field and a temperature gradient. Since the magnetization of the FF is both temperature and magnetic field intensity-dependent, strong thermomechanical coupling exist and will be discussed further in this chapter [33].

The magnetic force per unit volume on a magnetizable fluid is termed the Kelvin body force (f^{Kelvin}). It describes the force per unit volume which acts on a small piece of magnetized material in an inhomogeneous magnetic field given by [7][8]:

$$\vec{f}^{Kelvin} = \mu_0(\vec{M} \cdot \bigtriangledown)\vec{H}_{ex}. \tag{2.14}$$

Here, f^{Kelvin}, μ_0, M and H_{ex} are the Kelvin body force (N/m^3), magnetic permeability of vacuum (N/A^2), magnetization of the FF (A/m) and the external magnetic field (A/m) respectively. The external magnetic field is the field that would be present at a certain location if any dipoles were not there. A magnetic field added by the magnetic dipole moment itself cannot contribute to the total force acting on the magnetic dipole moment due to the conservation of momentum. It is therefore easy to confuse H_{ex} with the field which would be existing if no FF was present (H_0). However according to Aursand et al. [8], H_0 is a good approximation for H_{ex} in terms of the application in Figure 2.10 and in this thesis.

The experimental rig in Figure 2.10 is similar to the setup in this thesis. For such a rig, the magnetic field has two special properties. The magnetic field dominates in one axial direction (H_x), and the field (H_x) does not vary much radially within the pipe. Isotropic magnetization is assumed, which means that the magnetization and the magnetic field are collinear. Because of these special properties and approximations, Eq. (2.14) is reduced to a one-dimensional form given by [7][8][33]:

$$f^{Kelvin} = \mu_0 M \frac{\partial H}{\partial x}, \tag{2.15}$$

where the term $H_{ex} \approx H_0$ is given by the notation H. One of the most interesting applications of ferrohydrodynamics is termed thermomagnetic pumping, also called magnetocaloric pumping [52]. Here, a FF is thermomagnetically pumped using only a static inhomogeneous magnetic field and a temperature gradient. Thus the magnetic field is converted into useful flow work without a mechanical pump. A magnetic field will not produce any flow work by itself and is depending on a temperature gradient being present. Hence, a net pumping force is achieved because of the temperature-dependence of the FF magnetization [8][52][7].

The phenomena of thermomagnetic pumping will be described by the use of the experimental rig in Figure 2.10. It is a pipe that goes through a solenoid with FF flowing inside. The position x of the solenoid stretches from x=0.075 m to x= 0.17 m. A heater is connected to the tube from the middle out of the solenoid (x=0.125 to x=0.225), which establish the thermal gradient. The cold fluid at the left is set into motion due to the magnetic attraction into the interior of the solenoid where the magnetic field strength is strongest. The field gradient $\frac{\partial H}{\partial x}$ and magnetization

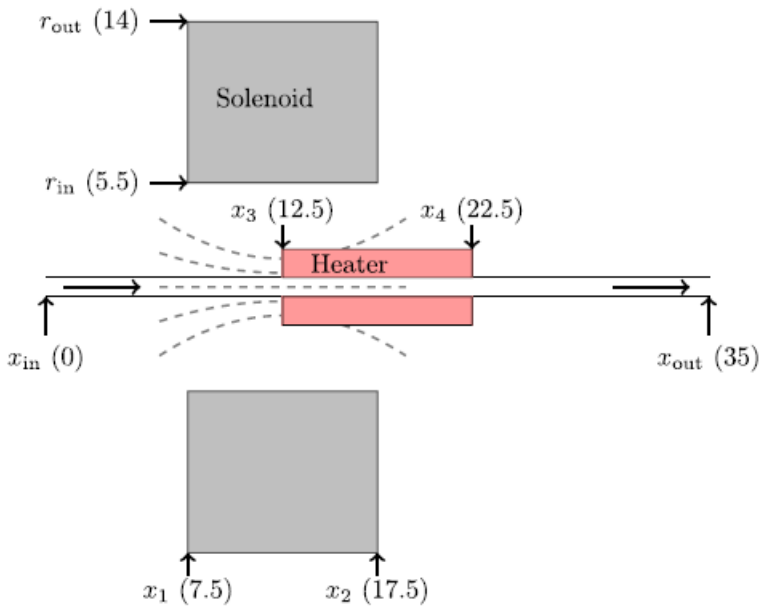

Figure 2.10: A cross-section of the experimental rig. The rig geometry is rotationally symmetric around the pipe axis. With the origin at the left and centre of the pipe, numbers show positions in cm, with vertical and horizontal arrows giving axial and radial positions, respectively. Dashed lines illustrate the magnetic field lines [7].

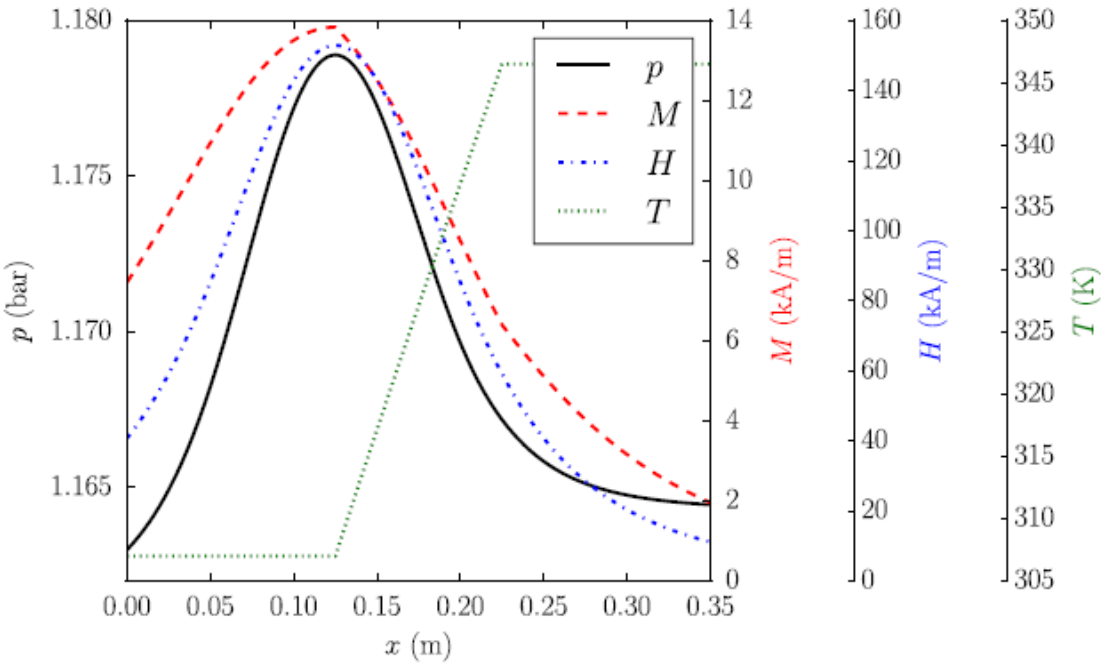

Figure 2.11: Variation of pressure, fluid magnetization, magnetic field and temperature as a function of pipe position x, where $\Delta T = 70$ K and $H_{max} = 153$ kA/m [7].

M are direct along the x-axis, which leads to a Kelvin body force direct along the x-axis. In the middle of the solenoid, the fluid is influenced by the heater. The magnetization is a function of both temperature and magnetic field (M = M(T,H)) [52][36]. Thus, as the fluid gets warmed up by the heater, it approaches the Curie temperature (Figure 2.4), which causes the magnetization to decrease. Hence, the Kelvin body force is smaller on the heated fluid than on the colder fluid. The field gradient $\frac{\partial H}{\partial x}$ is negative on the right side of the solenoid and causes a negative kelvin force. The negative kelvin force is smaller than the positive kelvin force, due to the magnetization reduction. This difference in the positive and negative kelvin force on the left and right side of the solenoid respectively leads to a net pressure difference Δp over the solenoid. This produces a convective motion which is called thermomagnetic convection or thermomagnetic pumping force [8][7][52].

How the pressure (p), fluid magnetization (M), magnetic field (H) and temperature (T) in the experimental rig in Figure 2.10 varies as a function of pipe position (x), is visualized in Figure 2.11.

2.4.1 Application of thermomagnetic convection

The concept explained above can be exploited to a closed flow loop with a circulating FF. Such an energy conversion in a closed flow loop with the presence of an external field shows great potential for application in a great variety of fields, especially in thermal management of electronic systems. Several researchers have investigated the phenomena of thermomagnetic convection [69][12][67][41][38][8][33][13], which proves the enthusiasm for this energy transport system. Results have shown that thermomagnetic convection loops is a simple design, which is silent, self-driven, self-regulating and maintenance-free [33]. A review of some works in this field is presented in the next section.

2.5 Literature review

Mei et al. [41] investigated the influence of a paralleled magnetic field on the thermo-hydraulic performance of the FF Fe_3O_4-H_2O in a circular tube loop. It showed good heat transfer performance. It was found that applying a parallel magnetic field in a temperature gradient could increase the Nusselt number by 22.1%. The design is shown in Figure 2.12.

Lian et al. [38] developed an automatic energy transport device (AETD) shown in Figure 2.13. The FF was a hydrocarbon-based Mn–Zn ferrite magnetic fluid with a volume concentration of about 4.5%. The average diameter of the suspended magnetic particles was about 6.8 nm. The temperature gradient was generated by a heating and heat-rejection section. The heat load on the former section varied

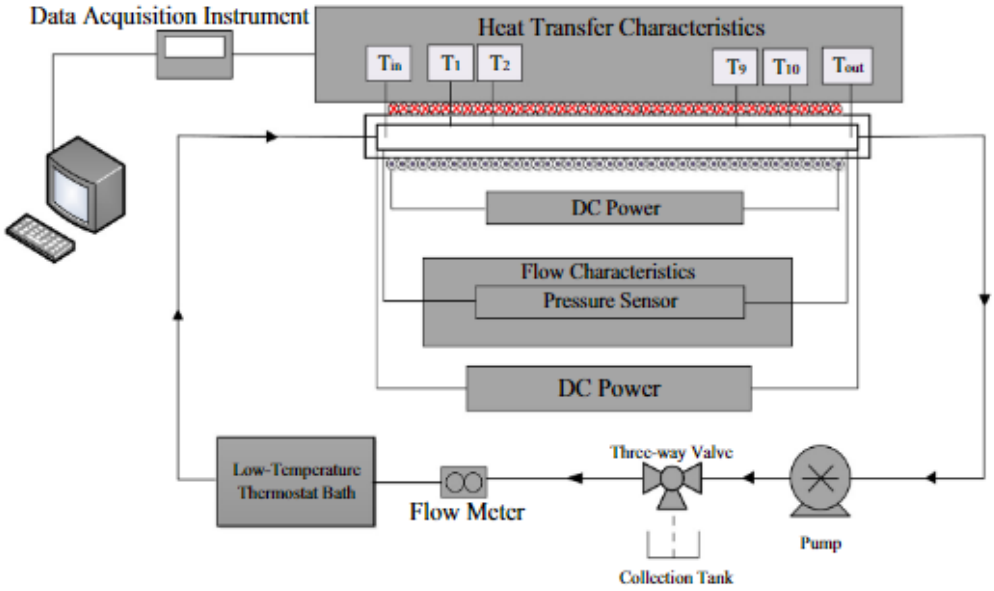

Figure 2.12: Schematic diagram of the experimental system [41].

from 1 W to 9 W, and the temperature of the latter section varied between 5 °C, 0 °C and -5 °C. By using the FF as a coolant with both a magnetic field and a temperature gradient present, a magnetic force was generated. The magnetic force caused the fluid to move and lead to a stable circulating flow. They stated that since no mechanical moving parts are needed in such devices, they are highly applicable in a lot of different applications such as energy conversion devices, electronic cooling devices etc. It was found that by adjusting the external magnetic field and/or the temperature gradient in the FF, it is possible to control the energy transport process of such systems. Additionally, the device showed a self-regulating feature where the flow velocity increased with an increasing temperature gradient (heat load). This indicates that the external heat load automatically controls the operation of the cooling device.

Xuan et al. [69] used thermomagnetic convection loop in electronic cooling. The device used the generated waste heat from the electronic elements to drive the FF flow and to transport heat to a far end for dissipation. A hydrocarbon-based Mn–Zn ferrite magnetic fluid was used as the FF. The averaged diameter of the suspended magnetic particles was about 6.8 nm, and the volume fraction was about 4.5%. The temperature gradient was generated by a heating and heat-rejection section. The heat load on the former section varied from 1 W to 5 W, and the latter section consisted of a blower which was varied between 0 V, 9 V and 12 V. They found that by utilizing an earth magnet located close to the heat source could produce a better cooling performance. No additional energy other than the dissipated waste heat is used for driving the FF flow, and the device can thus be considered self-

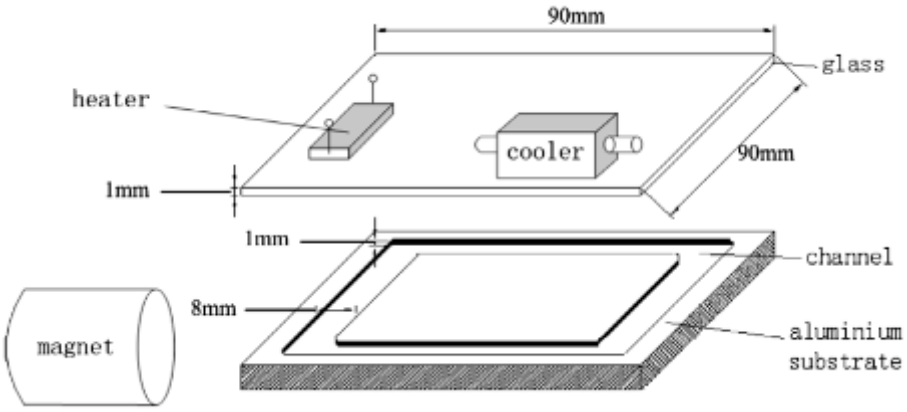

Figure 2.13: Scheme of the studied automatic energy transport device [38].

powered. They also discuss the advantages and disadvantages of thermomagnetic cooling for electronic cooling applications. With an increase in heat load, a higher heat dissipation rate can be realized, because of stronger thermomagnetic convection. This indicates a self-regulating feature. The prototype of the cooler investigated in this work is visualized in Figure 2.14.

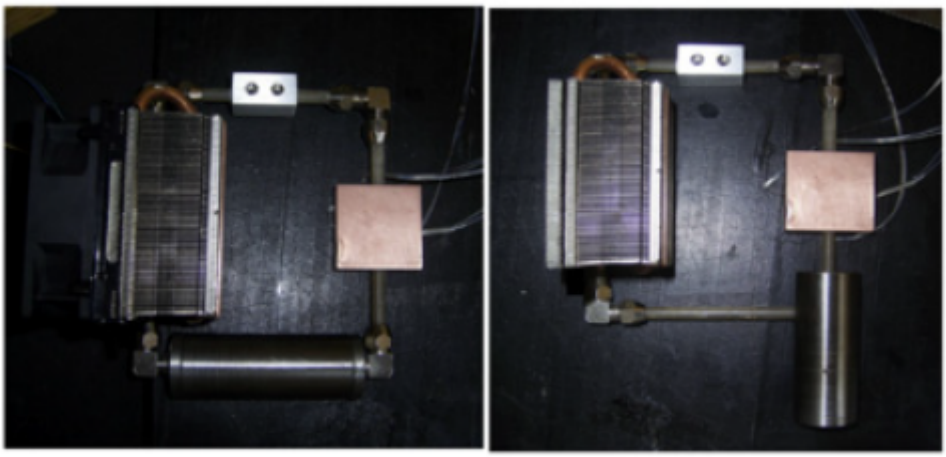

Figure 2.14: Prototype of a thermomagnetic cooler [69].

Aursand et al. [8] suggested a procedure for designing an optimal solenoid and FF for the application showed in Figure 2.15. They derived a simple approximation for the expected thermomagnetic convection action by the use of simulations. The FF was a mix between the base fluid kerosene and the nanoparticles MnZn-Ferrite, with an average particle diameter of 10.0 nm. The volume concentration was kept at 10%. The temperature gradient was generated by a heating and heat-rejection section. The former and latter sections obtained a temperature of 90 °C and 10 °C, respectively. The result showed that the cooling power always increased with in-

creasing field strength. However, they found that different maximum field strengths (H_{max}) are optimal depending on the temperature difference (ΔT). It was concluded that the thermomagnetic driving force is significant compared to natural convection. The cooling performance from thermomagnetic convection was found to be 2.4 times better than the cooling performance from the natural convection. It should be noted that the performance enhancement may vary with size scales and variations in rig design. Additionally, performance enhancement of 50% was within reach, simply by adding nanoparticles to the base fluid.

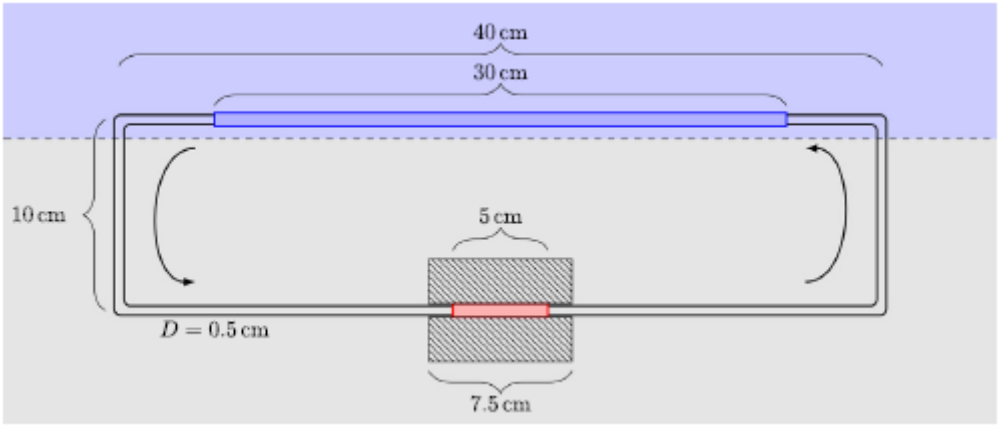

Figure 2.15: A schematic of the simulated flow loop, showing the heat source at the bottom section and the heat-rejection source at the top section. The solenoid cross-section is shown as hatched boxes. Gravity points downward in-plane. All dimensions are to scale. Arrows show the chosen flow direction [8].

Wrobel et al. [67] executed an experimental and numerical analysis of a thermomagnetic convection flow with FF in an annular enclosure with a round rod core and a cylindrical outer wall present. The FF was a concentration of 0.3 mol/(kg of solution) of gadolinium nitrate hexahydrate. The temperature gradient was generated by a heating and heat-rejection section. The two different investigated heat loads on the former section were 4.45 W to 13.11 W, and the latter section obtained a temperature of 18.0°C. The scheme is shown in Figures 2.16 and 2.17. How the position of the annular vessel affected the thermomagnetic convection of the FF was also tested. The result showed that the magnetic force affects the heat transfer rate. It was found that the magnetic field yielded heat transfer values four times higher than those the thermal Rayleigh number did. Thus the magnetic field enhances heat transfer far more efficiently than increasing the thermal Rayleigh number.

Moghaddam [33] investigated analytically, numerically and experimentally the thermomagnetic convection effect on a FF in a flow loop, under the influence of an applied magnetic field and a temperature gradient. Additionally, how the position of the heat source relative to the magnetic field source affected the cooling perfor-

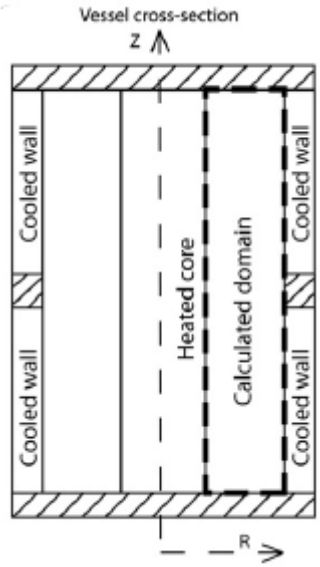

Figure 2.16: Modelled system of the cross-section of the vessel [67].

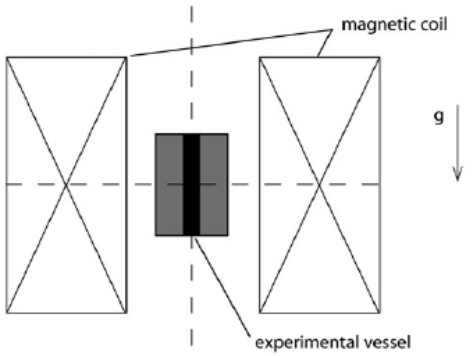

Figure 2.17: A scheme of the setup, with the vessel enclosed by the magnetic coil. Vessel located in the middle of the coil [67].

mance was studied. Results showed that the heat source should be located from the middle out of the solenoid. This produced the highest flow velocity and cooling performance. It was also found that by increasing the magnetic field intensity, increases the cooling capacity of the thermomagnetic circulation flow loop. The scheme for the numerical and experimental studies is visualized in Figures 2.18 and 2.19 respectively.

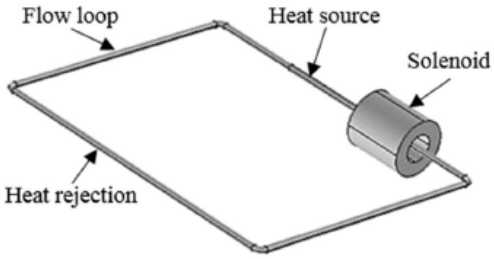

Figure 2.18: Schematic layout of the thermomagnetic circulation flow loop for the numerically study [33].

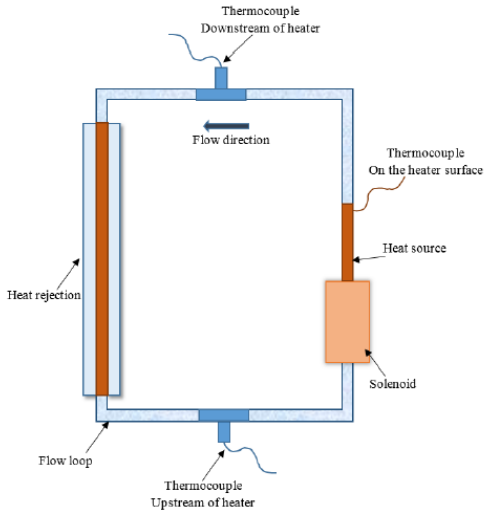

Figure 2.19: Schematic layout of the thermomagnetic circulation flow loop for the experimentally study [33].

Chapter 3

Methods

3.1 Research design

An experimental set-up was designed to investigate the performance of thermomagnetic circulation in a flow loop. The performance capability was analyzed by collecting temperature data. The nanoparticles used in this study were iron(III) oxide (Fe_2O_3). The thermomagnetic convection was obtained by a magnetic field created from a solenoid, in combination with a temperature gradient on the fluid.

The experiments were conducted at two different rig orientations, horizontal and vertical. Different particle concentrations and magnetic field strengths were investigated to achieve optimum cooling performance. In the horizontal case, different values of power input were additionally investigated. A full description of the methods used in this thesis is addressed in this chapter.

3.2 Experimental setup

The custom build apparatus was self-made and developed at the Department of Physics and Technology at the University of Bergen. As mentioned in the previous section, experiments were performed with the rig oriented both in a horizontal and vertical direction. An illustration of the rig for vertical and horizontal orientation is shown in Figure (3.1) and Figure (3.2), respectively. The primary fluid channel consists of polytetrafluoreten (PTFE) tubes with an inner diameter (ID) equal to 4 mm and an outer diameter (OD) equal to 6 mm, that were connected with PTFE connectors such as elbows and T-shapes. The PTFE tubes were combined with a glass tube (ID = 4 mm, OD = 6 mm), a heat exchanger, an expansion tank and a fluid pump (DC 12V 60W Micro diaphragm Pump). This forms a 400 x 220 mm closed flow loop. Temperature sensors (thermocouple T-type) were mounted between the

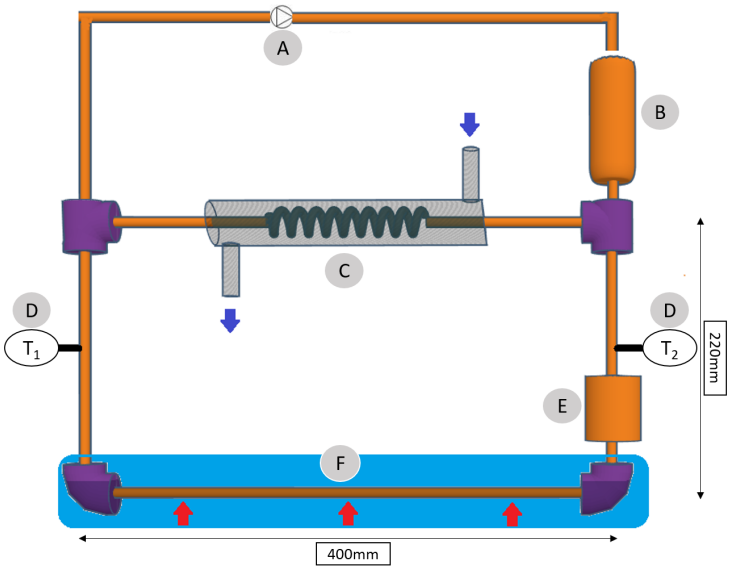

Figure 3.1: Scheme of the experimental apparatus in a vertical position, with thermal bath as a heating source. A is the fluid pump, B is the expansion tank, C is the heat exchanger, D on the left and right sides of the apparatus there are the two thermocouples with the notation T_1 and T_2 respectively, E is the solenoid and F is the thermal bath.

heating section and the heat-rejection section on each side of the flow loop, shown in Figures 3.4 and 3.5. The expansion tank was used to fill the system with fluid. The fluid pump transported the fluid through the apparatus and recirculated it back into the expansion tank until all air bubbles were eliminated in the system. The expansion tank was also used for safety reasons, in case of pressure buildup from fluid expansion. A solenoid was used as the source for obtaining the magnetic field. It was placed close to the heating section so that the magnetic field would spread over the temperature gradient. The location of the tank and the solenoid were altered when the apparatus got tilted to a horizontal orientation. This change can be seen in Figure 3.1 and Figure 3.2.

The heat section of the apparatus was made of a 400 mm glass tube (ID = 4 mm, OD = 6 mm). For the vertical case, the section with the glass tube was lowered into a hot thermal bath which was used as the heating source. The thermal bath consisted of a metallic container filled with tap water, heated by a hot plate (VWR Hotplate [25]), and set to hold a constant temperature of 62°C. For the horizontal case, the heating source was changed to a halogen lamp of type Cotech floodlight 400 W / 230 V, to investigate the possibility of utilizing the phenomenon of magnetic convection to obtain fluid flow in a DASC. The lamp was placed over the glass tube and radiated downwards. The distance between the light source and the glass tube

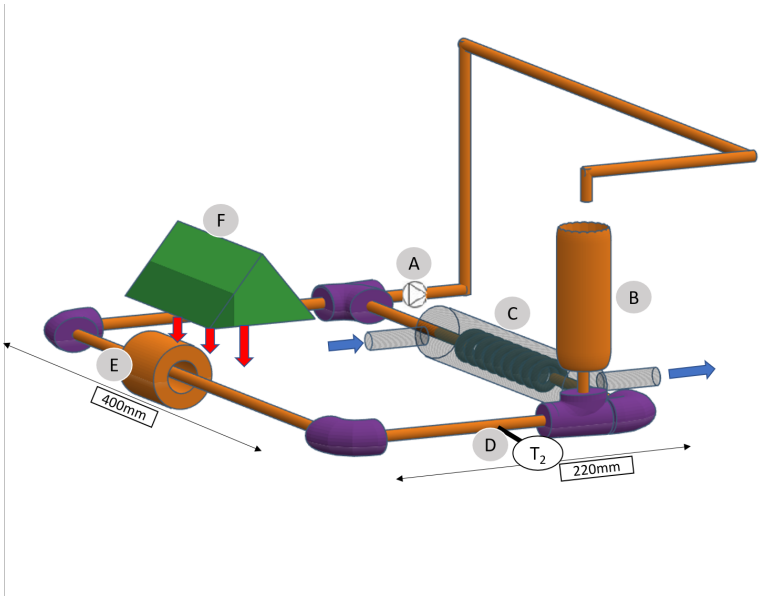

Figure 3.2: Scheme of the experimental apparatus in a horizontal position, with halogen lamp as a heating source. A is the fluid pump, B is the expansion tank, C is the heat exchanger, D are the two thermocouples, E is the solenoid and F is the halogen lamp.

was varied to investigate the influence of the power input.

The heat exchanger in Figure 3.3 was used as the heat-rejection source. It was mounted onto the PTFE tubes, with different assembly configurations on each side. The heat exchanger included a central helix glass tube surrounded by an outer concentric glass tube (ID = 31 mm, OD = 33 mm). The helix had an inner diameter equal to 8 mm, and outer diameter equal to 20 mm. The tube of the helix had an inner diameter equal to 4mm and outer diameter equal to 6 mm. In the void between the helix and the outer concentric glass, a counter-current flow of cold water was injected. This was provided from the spring, which obtained a water temperature approximately constant to 12°C.

The solenoid (FC-5818) was a electromagnet coil purchased from APW Company [18], and its characteristics is presented in table 3.1. The solenoid generated heat from the applied current and absorbed heat from the heating section, which caused the temperature of the solenoid to increase. Because of this temperature increase, the electrical resistivity of the wire of the solenoid increased. Hence, from Ohms law, a decreased current through the wire of the solenoid was obtained, due to the solenoid restriction of 6 volt. This generated a weaker magnetic field intensity. A fan cooler was used to hinder the temperature of the solenoid to rise, to maintain a constant magnetic field strength. The other parts of the apparatus were protected from the fan cooler with aluminium foil.

Figure 3.3: Heat exchanger used in the experimental apparatus. The left and right assembly configuration between the tube and the heat exchanger are visualized.

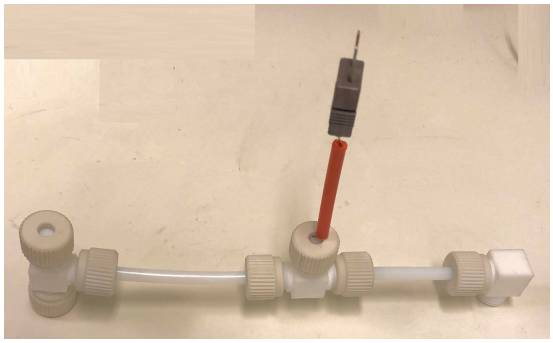

Figure 3.4: The assembly of temperature sensor T_1.

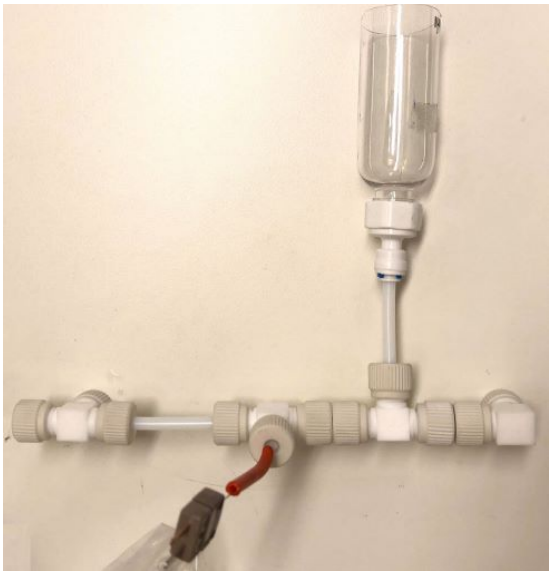

Figure 3.5: The assembly of temperature sensor T_2 and the expansion tank, with the apparatus in horizontal orientation.

Voltage (V)	6
Current (A)	1.26
Resistance (Ω)	4.75
Wire gauge	23
Turns	800
Bobbin OD (mm)	38.1
Bobbin ID (mm)	19.05
Bobbin length (mm)	44.704

Table 3.1: Solenoid specifications.

3.3 Development of the experimental setup

3.3.1 Nanoparticles

The material of the nanoparticles used in this study was iron(III) oxide [56], with the formula Fe_2O_3. It can also be called ferric oxide, hematite or the general term iron oxide. Ferric oxide possesses strong magnetic properties and is an alternative to the more expensive industrial limited nanoparticles. In addition, few researchers have investigated the use of the nanoparticles Fe_2O_3 in thermomagnetic convection systems [60]. The particle size was smaller than 50 nm, the molecular weight was 159.69 g/mol and the surface area was 50-245 m^2/g, specified from the supplier [56].

3.3.2 Nanofluid preparation

There are two widespread methods for nanofluid synthesis, termed the one-step process and a two-step process. The one-step process was selected due to the decrease in particle agglomeration, increase in fluid stability and a more straightforward procedure [37][71][61]. Various techniques for breaking agglomerates with sonication have been investigated [27][6]. A direct ultrasonic probe was found to be most efficient, but an indirect ultrasonic bath also reported a positive impact on particle agglomeration. An indirect ultrasonic bath (Branson 3510 Ultrasonic cleaner) was already available at the University of Bergen. Therefore, this was used in this thesis due to the high cost of purchasing a direct ultrasonic probe. The specified ultrasonic bath has a frequency of 40 kHz, and a power of 130 W.

The particle concentration was represented by mass fraction. The iron(III) oxide powder and the base fluid were measured by the scale of the type Sartorius CPA 324S, with an uncertainty of $\pm$ 0.0001 gram. The base fluid was distilled water from Fybikon. The iron(III) oxide powder and distilled water were measured in two separate beakers, to allow the removal of chemicals in case too much substance was weighed. The particles were added into the base fluid beaker and gently stirred with a glass rod, before sonicating for 30 minutes.

3.3.3 Stability

The nanofluid stability was studied by visual observation in order to investigate potential sedimentation. The ferric oxide FF (Fe_2O_3-water) was prepared by the one-step process, with the different concentrations of 0.5 wt.%, 1.0 wt.%, 1.5 wt.% and 2.0 wt.%. The samples were tested with the dispersant polyvinylpyrrolidone (PVP) and sodium dodecyl sulfate (SDS), to attempt to improve fluid stability. The concentration of the dispersants was equal to 1.0 wt.%. The entire stability study can be found in the Appendix (B). Stability investigation of 1.0 wt.% of Fe_2O_3 is shown in Figures (3.6 - 3.11). For all the different concentrations, the samples

with the surfactant SDS showed the worst fluid stability, with significant deposition. The samples with the polymer PVP showed good stability, but had slightly more precipitate after 24 hours compared with the samples without dispersant. Hence, it was challenging to choose the most stable sample, due to the small difference between the samples with PVP and without dispersant. However, it is redundant and unnecessary to add an extra component in the fluid such as a dispersant, without obtaining any improvement in the fluid stability. Thus, the samples without any dispersant were decided to be used in this thesis.

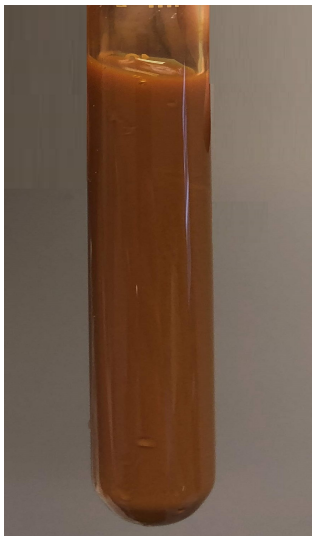

Figure 3.6: 1.0 wt.% of Fe_2O_3 without dispersant, after sonification.

Figure 3.7: 1.0 wt.% of Fe_2O_3 with 1.0 wt.% PVP, after sonification.

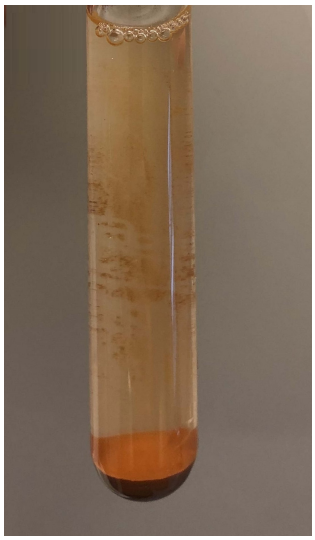

Figure 3.8: 1.0 wt.% of Fe_2O_3 with 1.0 wt.% SDS, after sonification.

The influence of pH on the stability of the samples was investigated by visual observation. From the previous paragraph, the samples without a dispersant obtained the best fluid stability. Therefore, the pH investigation was only performed on ferric oxide samples without dispersant. The concentration of 1.0 wt.% of ferric oxide, produced with the pH values equal to 2.2, 7.3 and 10.1 are shown in Figures (3.12 - 3.17). The hydrogen-ion activity in the solutions was measured with a pH meter (Lutron PH-221), with an accuracy of $\pm$ 0.02 pH. The pH values equal to 2.22 $\pm$ 0.02 and 10.11 $\pm$ 0.02 were obtained by adding sulfuric acid and ammonia solution, respectively. The fluid with a pH value equal to 7.32 $\pm$ 0.02 corresponds to the neutral solution, where no substance was added to alter the pH value.

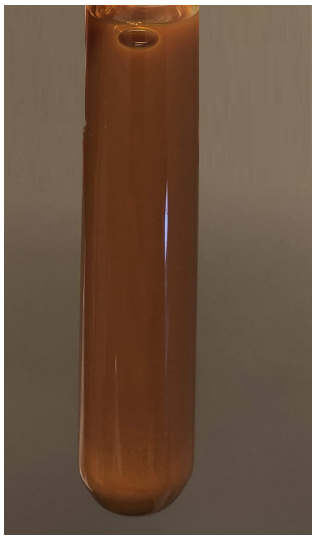

Figure 3.9: 1.0 wt.% of Fe_2O_3 without dispersant, 24 hours after sonification.

Figure 3.10: 1.0 wt.% of Fe_2O_3 with 1.0 wt.% PVP, 24 hours after sonification.

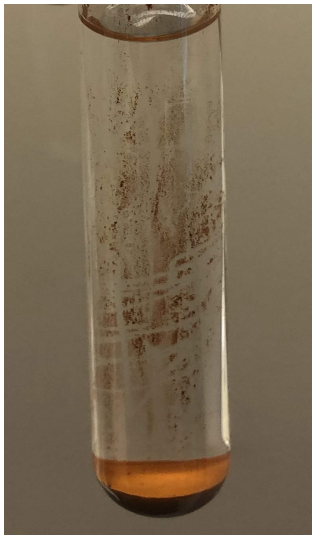

Figure 3.11: 1.0 wt.% of Fe_2O_3 with 1.0 wt.% SDS, 24 hours after sonification.

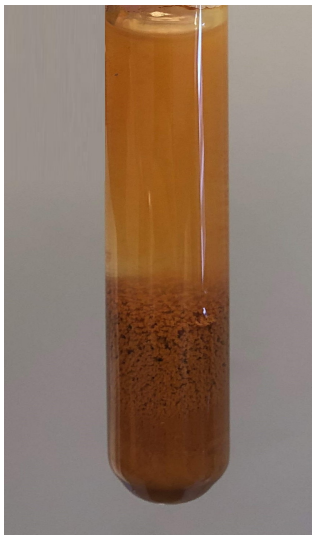

Figure 3.12: 1.0 wt.% of Fe_2O_3 without dispersant and pH=2.2, after sonification.

Figure 3.13: 1.0 wt.% of Fe_2O_3 with pH = 7.3, after sonification.

Figure 3.14: 1.0 wt.% of Fe_2O_3 with pH = 10.1, after sonification.

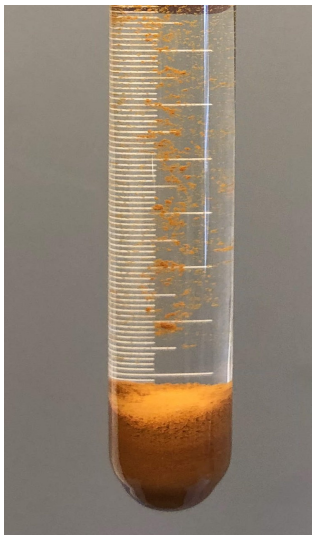

Figure 3.15: 1.0 wt.% of Fe_2O_3 with pH = 2.2, 24 hours after sonification.

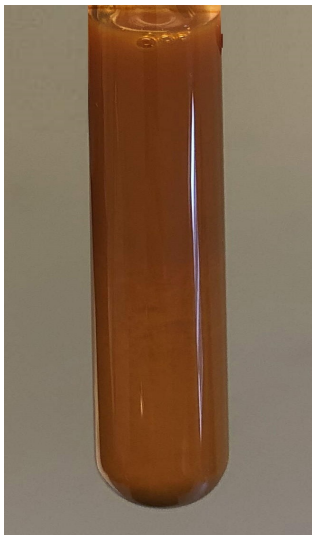

Figure 3.16: 1.0 wt.% of Fe_2O_3 with pH = 7.3, 24 hours after sonification.

Figure 3.17: 1.0 wt.% of Fe_2O_3 with pH = 10.1, 24 hours after sonification.

From Figures (3.12 - 3.17), changing the FF to a basic or acidic fluid resulted in lower stability. Thus, the pH value of the fluid was not altered in this thesis.

3.3.4 Particle size distribution

Studies of the particle size distribution (PSD) of the FF was done with static light scattering (SLS). The working mechanism of SLS is irradiation of the fluid with a laser. The incident light gets scattered due to its interaction with the particles and the carrier fluid. The scattered light creates a light pattern which is detected by sensors. The PSD is found by applying models of scattering prediction such as Mie-theory or Fraunhofer-approximation. This was done by the Malvern Mastersizer software, where the PSD was achieved in volume frequency. However, the scattering models are not discussed here, due to their insignificance for the objective of this thesis.

Malvern Mastersizer 2000 laser was the SLS devices used in this work. As mentioned, the PSD was obtained from the Malvern Mastersizer software and presented as volume frequency. The volume frequency is based on the total volume that is occupied by particles at a defined diameter. Thus, a large number of small particles has a negligible effect on the frequency due to their low volumes. Conversely, a few large particles with large volumes will significantly influence the frequency. This can give a false impression of which particle diameter that is most prevalent. Therefore, the volume frequency was converted to number frequency by [63]:

$$f_{n,d_i} = \frac{\left(\frac{6f_{V,d_i}}{\pi {d_i}^3}\right)}{\left(\sum_{d_i}^{d_n} \frac{6f_{V,d_i}}{\pi {d_i}^3}\right)}, \tag{3.1}$$

where f_{n,d_i} is the number frequency of particles with diameter $d \in [d_i, d_n]$ and f_{V,d_i} is the volume frequency of particles with diameter $d \in [d_i, d_n]$. For simplicity, the particles were assumed to be spherical in the conversion from the volume to number frequency.

Even though the vendor stated particles smaller than 50 nm, larger particles in the FF will be expected due to agglomeration within the fluid. Thus, static light scattering was performed to determine the particle size in the fluid. SLS was done on two prepared samples with 1.0 wt.% and 2.0 wt.% of Fe_2O_3, respectively. Calculated average particle diameter of the former and latter samples were 0.097 μm and 0.091 μm, respectively. The SLS results are shown in Figure 3.18.

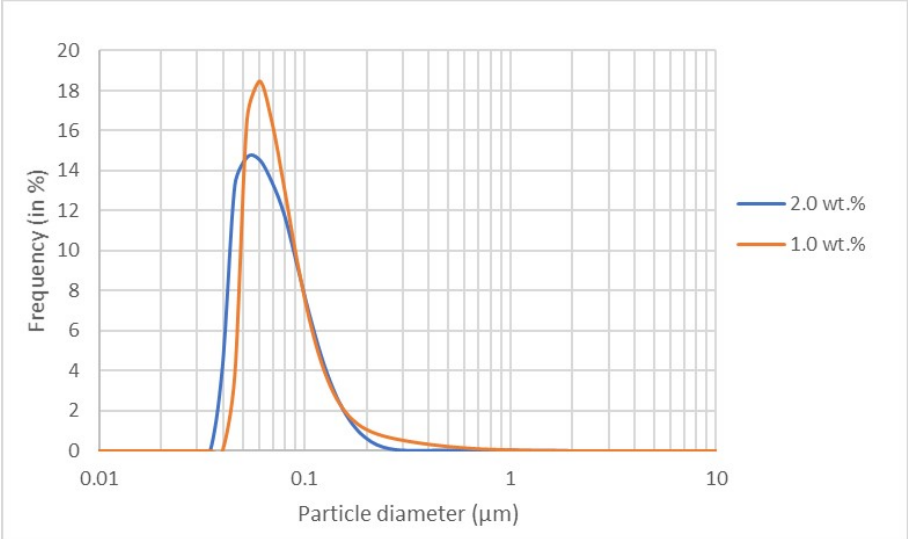

Figure 3.18: Number frequency of the particle size distribution of 2.0 wt.% and 1.0 wt.% of Fe_2O_3, obtained from SLS.

3.3.5 Temperature sensors

There are different sensing elements available for temperature control, such as thermocouples, thermistors, resistance temperature detectors (RTD) etc. Thermocouples are the most widely used method for temperature measurement, due to their temperature range, low cost, simplicity, small size and robustness [16]. The basis of these devices is the Seebeck effect. It describes the production of an electromotive force (emf) generated in a circuit of two different conductors experiencing a thermal gradient. The amount of electromotive force generated corresponds to a defined temperature.

Thermocouples are categorized as a noble metal, base metal, refractory metals or non-metals. There is a wide range of standardized thermocouples. Type E, K and T are the most commonly used and are made of base metals. The main differences between the types are the temperature range and accuracy. Specifications of the thermocouples collected from the vendor are shown in table 3.2, which states that the T-type has the highest accuracy of ± 1.0°C. Hence, the T-type thermocouple is chosen for this thesis.

Spesification	**E-type**	**K-type**	**T-type**
Temp-range	−200° - 900°C	−200° - 1250°C	−250° - 350°C
Accuracy	± 1.7°C	± 2.2°C	± 1.0°C

Table 3.2: Thermocouple specification stated from the vendor [47].

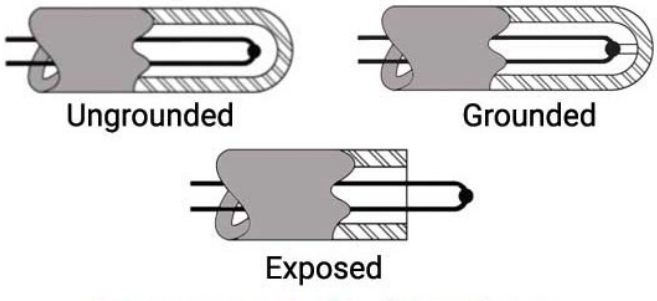

Figure 3.19: Three different thermocouple junction types: ungrounded, grounded and exposed [19].

The different junction types available for thermocouples are exposed, grounded and ungrounded. The exposed type is limited to use in noncorrosive and nonpressurized applications, and can not be used in FFs. The grounded type provides intimate contact between the conductors and sheath, which results in faster response time compared to the ungrounded type [48]. Consequently, small grounded T-type thermocouples (HTMQSSIM100G150) from Omega are mounted on the apparatus. The material of the sheath is steel, due to its chemical compatibility, which means that the sheath will remain very stable during exposure with other substances.

3.3.6 Radiation source

For experiments with the apparatus in a horizontal position, one halogen lamp was used as the heating source. The maximum power was 4000W, stated by the vendor. A LS122 Infrared Power Meter [28] measured the radiative intensity I of the lamp. It gauges the intensity of the incoming radiation in the unit $\mathrm{W/m^2}$. The spectral range of the LS122 gauge is limited to $\lambda \in [1000, 1700]$nm [28], which is within the infrared spectrum. It should be noted that the lamp most likely emits radiation also outside this range, which causes the measured intensity values to be lower than the actual radiation intensity.

With decreasing distance from the lamp, the radiation intensity increased. In addition, it was found that the radiation intensity at the illuminated area was unevenly distributed, with the strongest intensity at the centre line of the beam. The measurements were done at different distances, where the sensor was moved along the centre line of the beam. The sensor was always pointing towards the centre of the lamp. Measured values of the radiation intensity at a distance of 2.0 cm to 10.0 cm from the lamp is shown in Figure 3.20.

The polynomial line in Figure 3.20 is calculated from the average of the three measurements. The intensity from the lamp as a function of distance was obtained from

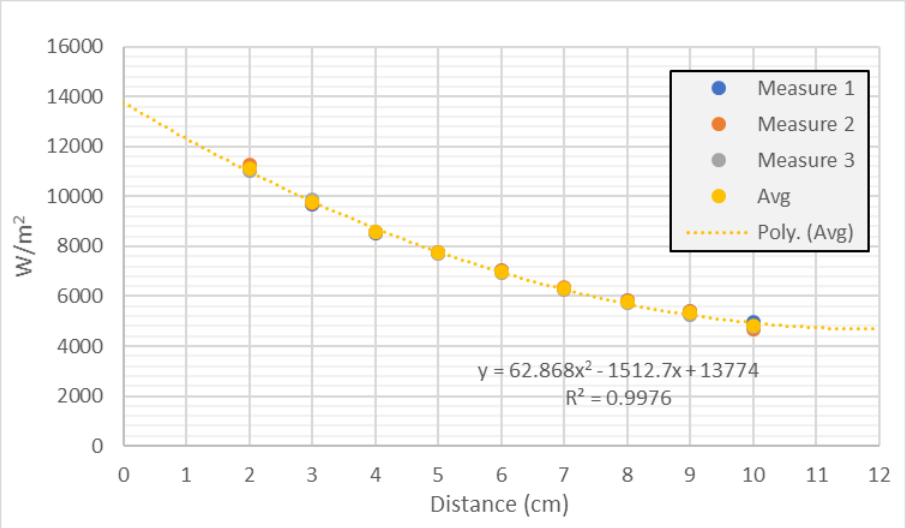

Figure 3.20: Light intensity as a function of distance.

the polynomial equation. It is given as follows:

$$I(x) = 62.868x^2 - 1512.7x + 13774, \tag{3.2}$$

where I is the intensity from the lamp in W/m^2 and x is the distance in cm. The R^2 value was equal to 0.9976, which indicated a good fit for the regression line. Error from the unevenly distributed radiation intensity at the illuminated area, and the limited spectral range of the sensor must be noted. Still, for simplicity, values obtained from Eq. (3.2) were used in this thesis.

3.4 Cooling performance

The cooling performance of the apparatus refers to its ability to reduce or regulate the temperature of a system. A good indicator of the cooling performance is the fluid velocity, where higher fluid velocities induce enhanced cooling performance [33]. A method to measure the velocities directly was not found and was therefore estimated from the temperature differences.

The velocity calculations for the vertical and horizontal direction setup required different approaches. In the vertical case, for calculating the velocity analytically, the Bernoulli equation was combined with the continuity equation. The velocities for vertical direction were also found through computational fluid dynamics (CFD). In the horizontal case conservation of energy was used. In both the vertical and horizontal cases, properties of the FF were assumed to be approximately equal to

water. Thus, properties values of water were used for the density, viscosity and specific heat capacity.

3.4.1 Velocity calculation for vertical direction setup

Average velocities and Reynolds numbers were calculated both analytical and by CFD. In the analytical calculation, the positive pressure difference over the solenoid was not taken into account. Therefore, the results from the analytical calculations will only reflect the natural convection at the corresponding temperature differences. Additionally, CFD was used to compute the actual fluid velocity, where both natural and forced convection were included. The CFD part is described in Chapter 4. The analytically calculated velocity can be used as a reference value. By comparing the analytically calculated velocity with the velocity estimated from the CFD program, an indication of how much the fluid velocity increases due to the applied magnetic field was achieved.

At first, the Reynolds number is defined:

$$Re = \frac{\overline{\rho}\ \overline{V}\ D}{\eta}, \tag{3.3}$$

where $\overline{\rho}$ is the average density (kg/m^3) found at the average temperature ($(T_1 + T_2)/2$), $\overline{V}$ is the average velocity (m/s), D is the pipe diameter (m) and η is the fluid viscosity (Pa·s). The Reynolds number is used to describe the pattern of the flow. The flow can be laminar (low Reynolds number), turbulent (high Reynolds number) or a transition between them where it will vary between laminar and turbulent in irregular intervals.

The analytical calculation of the fluid velocity is based on the Bernoulli equation:

$$P_1 + \frac{\rho_1 V_1^2}{2} + g\rho_1 Z_1 = P_2 + \frac{\rho_2 V_2^2}{2} + g\rho_2 Z_2 + \Delta P_{loss}, \tag{3.4}$$

where P is the pressure (Pa), ρ is the density, V is the velocity, g is the gravity (m/s^2) and Z is the height (m). ΔP_{loss} describes the total pressure loss (Pa) due to friction from the tube, friction from the four 90 degrees bends in the streamline and friction from the spiral in the heat exchanger. The notation 1 and 2 specifies two points on the streamline. Points 1 and 2 are set to the same position as the location of the two thermocouples on the apparatus visualized in Figure 3.1. Thus, the two points have equal heights ($Z_1 = Z_2 = h$). It is known from the continuity equation that $\rho_1 V_1 = \rho_2 V_2 = \overline{\rho}\ \overline{V}$. By the use of the relation from the continuity equation

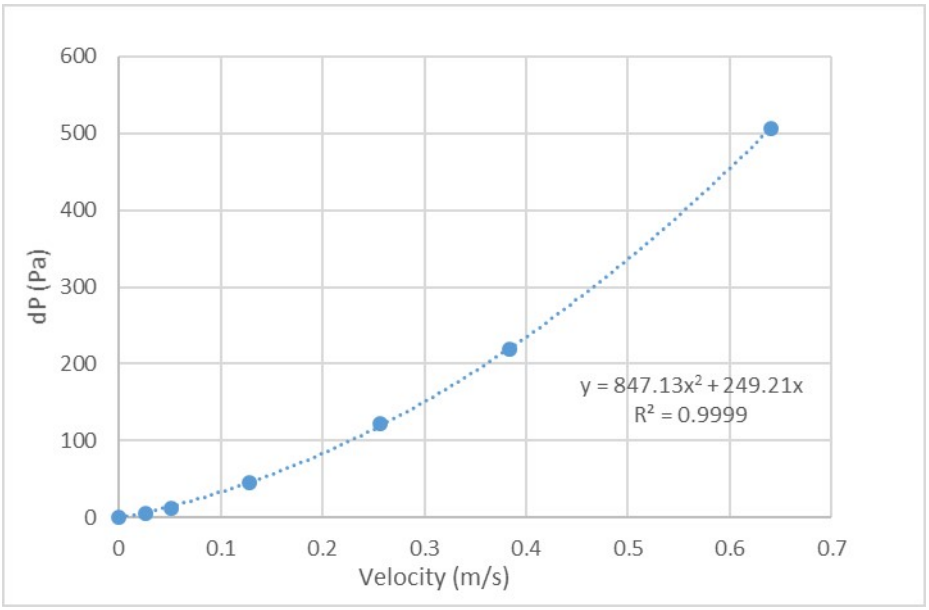

Figure 3.21: Pressure drop across the heat exchanger as a function of fluid velocity.

and that $Z_1 = Z_2$, an equation for the total pressure difference was obtained:

$$\Delta P_{tot} = P_1 - P_2 = \frac{\overline{\rho}^2\ \overline{V}^2}{2}\left(\frac{1}{\rho_2} - \frac{1}{\rho_1}\right) + (\rho_2 - \rho_1)gh + \Delta P_{loss}, \tag{3.5}$$

where the first two terms on the right-hand-side of Eq. (3.5) describes the positive dynamic pressure difference ($\Delta P_{dynamic}$) and negative hydrostatic pressure difference ($-\Delta P_{hydrostatic}$) respectively. As already mentioned, the last term (ΔP_{loss}) is the total pressure loss difference and is equal $\Delta P_{loss} = \Delta P_{friction} + \Delta P_{bends} + \Delta P_{spiral}$. These terms are calculated from the following equations:

$$\Delta P_{friction} = f\ \overline{\rho}\ \frac{\overline{V}^2}{2} = \frac{64}{Re}\ \overline{\rho}\ \frac{\overline{V}^2}{2}, \tag{3.6}$$

$$\Delta P_{bend} = 4K_{bend}\ \overline{\rho}\ \frac{\overline{V}^2}{2}, \tag{3.7}$$

$$\Delta P_{Spiral} = 847.13\overline{V}^2 + 249.21\overline{V}. \tag{3.8}$$

In Eq. (3.6), the friction factor f was equal to $\left(\frac{64}{Re}\right)$, because a laminar flow (low Reynolds number) was assumed. Since low velocities were expected, the assumption is acceptable. In Eq. (3.7) the characteristic bend coefficient was K_{bend} equal 1.5 and is multiplied with 4 because of the four corners of the streamline. Eq. (3.8) was

obtained from the investigation with the CFD program. The pressure drop across the heat exchanger was studied at different fluid velocities. The results were plotted in Figure 3.21, and a polynomial line between the points were created. The equation of the polynomial line (Eq. (3.21)) expresses the pressure drop (dP) across the heat exchanger as a function of the fluid velocity.

In the Bernoulli equation defined in Eq. (3.4), steady state is assumed, and the velocity does not change with time by default. The static pressure difference is zero, as both of them are at atmospheric pressures. As a result, the following equation is obtained:

$$\Delta P_{hydrostatic} = \Delta P_{dynamic} + \Delta P_{loss}. \tag{3.9}$$

The value of $\Delta P_{hydrostatic}$ is derived from the temperature difference. Since both $\Delta P_{dynamic}$ and ΔP_{loss} are functions of the velocity, the velocity can be found through iteration at a particular temperature difference. From Eq. (3.9), a discrepancy value in percent can be found from Eq. (3.10).

$$\binom{\text{Discrepancy}}{\text{Value}} = \frac{\Delta P_{dynamic} + \Delta P_{loss} - \Delta P_{hydrostatic}}{\Delta P_{hydrostatic}} \cdot 100\% < 1\% \tag{3.10}$$

The discrepancy values were obtained by iterating over velocity in the interval $V \in [0.1, 100]$ mm/s, with a step of 0.1 mm/s. When the discrepancy value is lower than 1.0 %, the correct velocity value is assumed. This velocity calculation is only valid for natural convection. It does not take the positive pressure difference over the solenoid into account. This velocity is used as a reference value to determine how much the velocity has increased when affected by a magnetic field estimated by CFD calculations.

3.4.2 Velocity calculation for horizontal direction setup

The average velocity and the Reynolds number were calculated by the use of conservation of energy, described as followed:

$$Q = \dot{m} C_p \Delta T, \tag{3.11}$$

where Q is the applied rate of heat flow to the system in (W), $\dot{m}$ is the mass flow rate of the fluid in (kg/s), C_p is the specific heat capacity in (J/(kg·K)) and ΔT is the temperature difference between the two measuring points in (K).

Several assumptions were made by using this method. The system was assumed to be an adiabatic process, where no heat from the fluid is lost to the surroundings, and no chemical reaction occurs within the fluid or between the fluid and the wall.

In order to find the applied rate of heat flow ($Q = IA$) from Eq. (3.2), the absorption area (A) must be defined. Heat absorption occurs both on the surface of the tube and inside the nanofluid. The total absorption area in the latter case is obtained by adding together the absorption areas from each particle within the fluid. The total absorbance area from each particle depends on several variables such as how deep the light travels within the fluid, particle concentration, particle agglomeration and the location of each particle as a function of time.

As a conservative estimate, heat absorption is assumed to occur only on the surface of the tube, shown in Figure 3.22. The heat flux from the light is strongest in the centre of the tube (centre of curvature). The incoming radiation beams on the edges of the tube will have to travel further and will not hit perpendicular to the tube, which reduces the heat flux from the light beam. Outside the centre of curvature will also bending of the light beams occur due to the density difference between air and glass, which will affect the absorption area. Furthermore, reflection, refraction and scattering of light in different directions are present due to the curvature of the glass tube.

In this thesis, the radiation area is simplified to the cross-section area of the curvature of the tube. The light beams will then hit perpendicular to the entire absorption area, shown in Figure 3.23. With a value for the absorption area (A), a value for the applied heat rate (Q) from Eq. (3.2) is obtained. It should be noted that discrepancies will occur in the calculation of the heat rate (Q), due to the aforementioned assumptions.

The mass flow rate can be expressed as:

$$\dot{m} = \frac{dm}{dt} = \frac{\rho dV}{dt} = \frac{\rho A dm}{dt} = \rho A u, \tag{3.12}$$

where m is the weight (kg), t is the time (s), ρ is the density (kg/m^3), V is the volume (m^3), A is the area (m^2) and u is the velocity (m/s). By combining Eq. (3.11) and Eq. (3.12), an expression for the velocity is obtained.

$$u = \frac{Q}{\rho A C_p \Delta T} \tag{3.13}$$

From the calculated velocity in Eq. (3.11) the corresponding Reynolds number is estimated from Eq. (3.3). Discrepancy will occur due to the aforementioned assumptions for Eq. (3.11) and heat rate (Q).

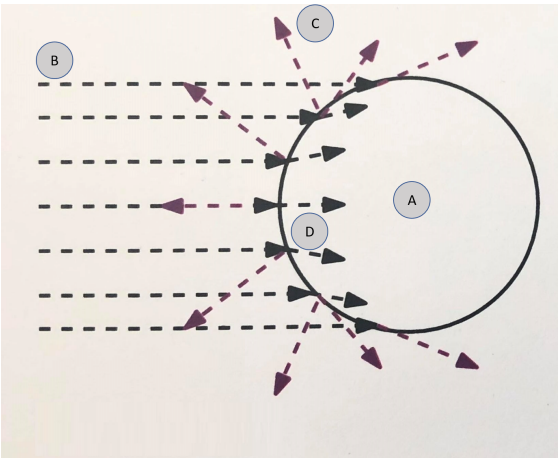

Figure 3.22: Cross-section of tube with radiation absorbance at the surface of the tube. A is the tube, B is the irradiated light with black lines, C is the reflected light with purple lines and D is the the refracted light with black lines.

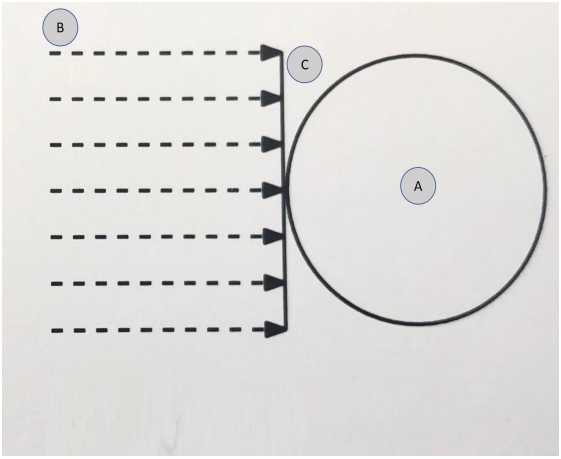

Figure 3.23: Cross-section of tube with radiation absorbance at the cross-section area of the tube. A is the tube, B is the irradiated light with black lines and C is the the cross-section area of the tube.

Chapter 4

Computational fluid dynamics

Computational fluid dynamics (CFD) is a method to quantify and visualize fluid flows by solving a set of algebraic equations numerically. Any physical aspects of fluid flow are described by the governing equations of fluid dynamics, namely the continuity equation, momentum equation and energy equation. These are obtained from the fundamental laws, conservation of mass, conservation of momentum and conservation of energy. The governing equations can be produced as either integral equations or partial differential equations. In CFD the integrals and the partial derivatives in these equations are replaced with discretized algebraic forms, and a set of algebraic equations is obtained. The algebraic equations are solved by the computer to produce numbers for the flow field values at discrete points in time and space. In contrast to a closed-form analytical solution, the end product of CFD will create a collection of numbers [4]. The CFD software used in this thesis is STAR-CCM+.

4.0.1 Discretization

Approximated algebraic difference quotients replace the partial derivatives or the integrals in the governing equations. The algebraic difference quotients are expressed in terms of the flow field variables at two or more of the grid points. Grid points are discrete points distributed across the domain. The algebraic difference quotients are solved for the value of the flow field variables at discrete grid points. The original governing equations have now been discretized. This method of discretization is called finite differences. There are three different methods of discretization, finite differences, finite volume and finite element [59].

STAR-CCM+ discretizes the system of equations by the use of either the finite volume method or the finite element method, dependent on the mathematical model. In this thesis, the segregated flow model is used, and the finite volume method is

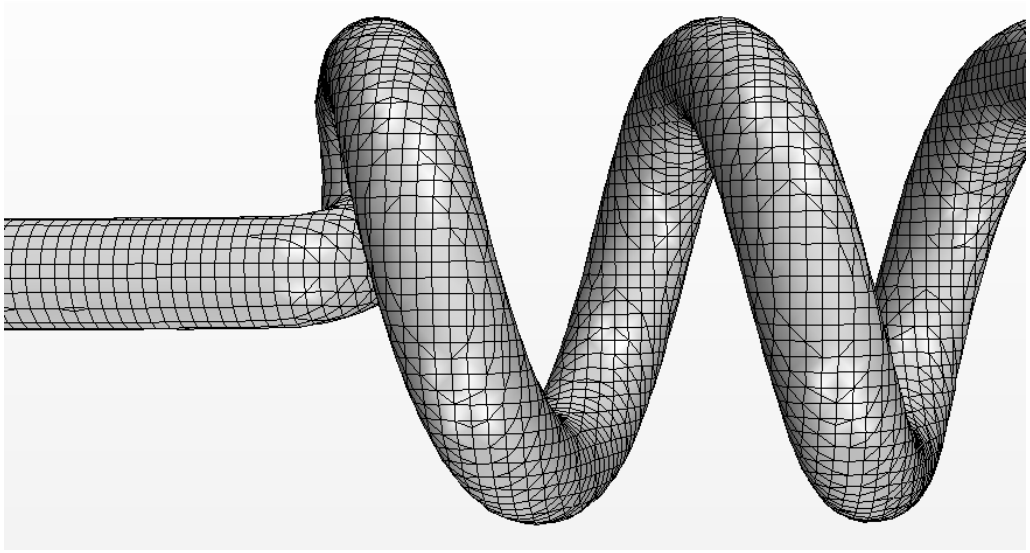

Figure 4.1: A snipping part of the mesh on the left side of the helix.

applied by STAR-CCM+ [59]. The governing equations are discretized in space and time. The produced linear equations are solved with an algebraic multigrid solver, due to its ability to accelerate the convergence [59].

4.0.2 Mesh/Grid

A mesh/grid is a network of discrete irregular subdomains, or cells, where the subdomains constitute the larger domain. A domain can include real-world geometry, its content and the surrounding environment. The discretized governing equations are solved at each subdomain, which generates an individual solution to all subdomains. By combining the solutions from all of the subdomains, a solution for the whole mesh (domain) is obtained. For finite volume discretization, STAR-CCM+ calculates values at the center of the subdomains [59].

Two different mesh types were used in this thesis, surface remesher and trimmed cell mesher. The geometry was first made in AutoCAD, and imported as a stereolithography (STL) file to STAR-CCM+. A STL imported surface is always represented as surface mesh part. From the STAR-CCM+ user manual [59], it is recommended to use the surface remesher on imported SLT files. The surface remesher retriangulates the existing surface, which improves the overall quality and optimizes the surface for the volume mesh models. This will ensure a closed surface without holes [59].

The trimmed cell mesher is a robust and efficient method of producing a volume mesh. The trimmed cell mesh will generate a high-quality grid [59]. A snipping part of the mesh on the helix is shown in Figure 4.1.

The generated mesh had a base size of 0.0005 m. The volume mesh had the following properties: total number of cells was equal to 210 728, total interior faces was equal to 578 008, total vertices was equal to 245 622 and total edges was equal to zero.

4.0.3 Fundamental laws

The fundamental laws used in STAR-CCM+ are presented below and are in differential form and for an infinitesimal control volume, stated from the STAR-CCM+ user manual [59]. These laws are developed into numerical solution techniques that STAR-CCM+ employs [59].

4.0.3.1 Conservation of mass

Through a control volume, the balance of mass is described by the continuity equation [59]:

$$\frac{\partial \rho}{\partial t} + \nabla \cdot (\rho \vec{v}) = 0, \tag{4.1}$$

where ρ is the density (kg/m^3) and v is the continuum velocity (m/s).

4.0.3.2 Conservation of momentum

The total force acting on the continuum will be of equal magnitude as the time rate of change of linear momentum. This is written as [59]:

$$\frac{\partial (\rho \vec{v})}{\partial t} + \nabla \cdot (\rho \vec{v} \otimes \vec{v}) = \nabla \cdot \sigma + \vec{f_b}, \tag{4.2}$$

where $\otimes$ is the outer product, f_b is the resultant of the body forces per unite volume acting on the continuum (N/m^3) and σ is the stress tensor (N/m^2). σ is the sum of the normal stresses and shear stresses. For a fluid, the stress tensor is written as the sum of normal stresses and shear stresses, $\sigma = -pI + T$, where p is the pressure, I is an unit tensor and T is the viscous stress tensor. Thus, for a fluid, Eq. (4.2) can be given as followed [59]:

$$\frac{\partial (\rho \vec{v})}{\partial t} + \nabla \cdot (\rho \vec{v} \otimes \vec{v}) = \nabla \cdot (pI) + \nabla \cdot T + \vec{f_b}. \tag{4.3}$$

4.0.3.3 Conservation of energy

Conservation of energy is obtained by applying the first law of thermodynamics to the control volume and is written as [59]:

$$\frac{\partial (\rho E)}{\partial t} + \nabla \cdot (\rho E \vec{v}) = \vec{f_b} \cdot \vec{v} + \nabla \cdot (\vec{v} \cdot \sigma) - \nabla \cdot \vec{q} + S_E, \tag{4.4}$$

where E, q and S_E are the total energy per unit mass, the heat flux and an energy source per unit volume respectively.

4.0.4 Geometry

The geometry is shown in Figure 4.2, and have the same dimensions as the vertical apparatus described in section 3.2. The tube in the flow loop has a diameter of 4 mm. The width of the loop is 400 mm and the height of the loop is 220 mm.

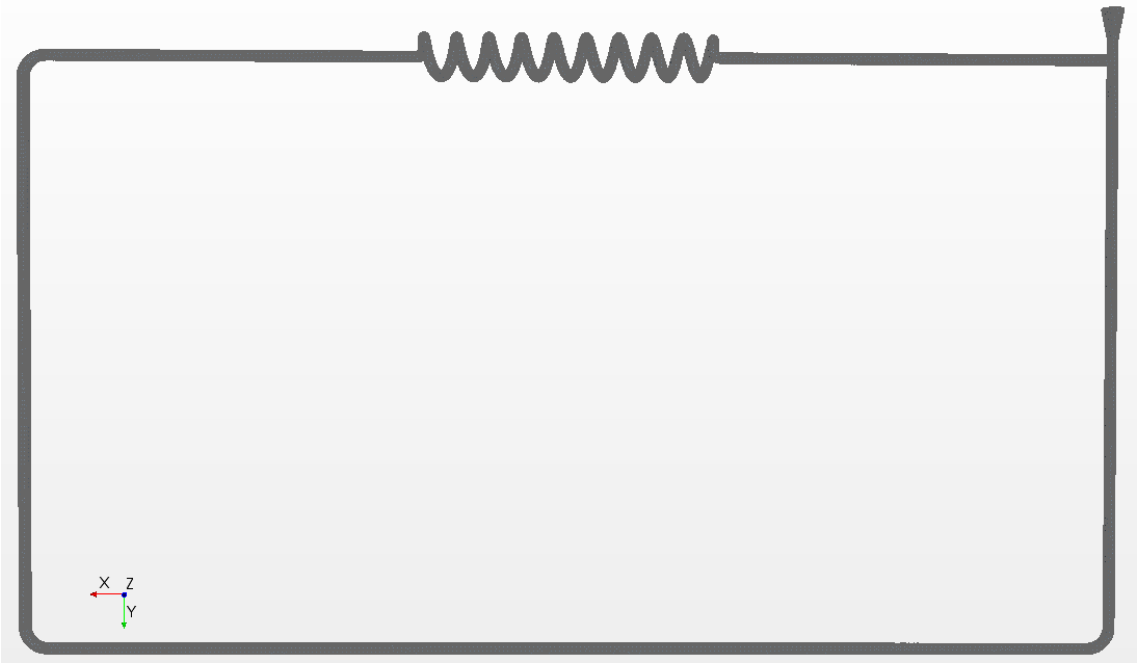

Figure 4.2: Geometry used in the CFD program.

4.0.5 Models

STAR-CCM+ has physics models that define the mathematical formulations used to produce the solution. In addition, the models also determine the primary variables of the simulation. The models are complex and have various functions, but the major purpose of the models is to work with the solvers to produce a solution and to help present the information to the user [59]. The models used are presented in table 4.1, and are described according to the STAR-CCM+ user guide [59].

The convective CFL (Courant–Friedrichs–Lewy) and energy-based time step control models adjust the length of time step automatically according to CFL and von Neumann number specified by the user. When the models are used together, the simulation always uses the shortest time step from the two models [59].

The gradients model allows the user to specify the gradient method and the limiter method. The former and latter methods were specified to be Hybrid Gauss-Least Squares and Venkatakrishnan method, which are the default methods. They improve the accuracy and robustness in unstructured meshes [59].

Models	**- Convective CFL Time-Step Control** **- Energy-Based Time-Step Control** **- Gradients** **- Gravity** **- IAPWS-IF97 (Water)** **- Implicit Unsteady** **- Laminar** **- Liquid (H_2O)** **- Segregated Flow** **- Segregated Fluid Temperature** **- Three Dimensional**

Table 4.1: The physics models used in the CFD program.

The gravity model includes the gravitational acceleration in the simulation [59].

IAPWS-IF97 (Water) model lets the user simulate with liquid water or gaseous steam. IAPWS-IF97 stands for "International Association for the Properties of Water and Steam, Industrial Formulation 1997". In this CFD-program, water is used instead of the nanofluid due to approximately equal properties, which is the reason for selecting this model [59].

Implicit unsteady model is one of the time models, which implements the implicit unsteady solver that control the iteration and unsteady time step. This is the only available unsteady time model for segregated flow models. With this model, the unknown quantities to be calculated at each time increment are expressed through parameters that are also unknown at the beginning of this increment. Therefore, iteration algorithms are necessary to achieve a numerical solution. Implicit methods are more complicated to use but usually much more stable, and larger time steps can be implemented [59].

Since low fluid velocities were expected, the laminar module was selected as the viscous regime [59].

The material model was selected to be liquid and specified as water, which is a single-component material. The liquid model manages the liquid that is simulated in the continuum. It is responsible for the thermodynamic and transport properties relevant to the selected substance and to the physical processes modelled in the continuum [59].

The segregated flow model was chosen as the flow model and applies the segregated flow solver to solve the momentum equations for each dimension in turn. It accomplishes a relationship between the momentum and continuity equation with a predictor-corrector approach. The model originates from constant density flows, but

it can handle moderately compressible flows. In addition, it can also handle flows of low Rayleigh number corresponding to laminar flow and heat transfer dominated by convection. In the segregated flow properties were the convection selected to be 2nd-order discretization scheme. This leads to good accuracy but can lead to poorer convergence properties [59].

The segregated fluid temperature model is one of the three segregated fluid energy models that come with the segregated flow model. The segregated fluid temperature model is selected because it calculates the temperature from solving the total energy equation [59].

4.0.6 Solvers

STAR-CCM+ adds the relevant solvers based on the selected physics models. Each solver has a specific task. Some solvers assemble the system of equations that describe the phenomenon of interest, some solvers solve the assembled system of equations and some solvers produce source terms to other solvers. The solvers used is presented in table 4.2, and are described according to the STAR-CCM+ user guide [59].

The solvers can be divided into two categories, the parent and the child solver. The parent solvers manage the physics and assemble the system of equations that must be solved. The child solver solves the equations. In addition, the child solver controls the solution of the linear system. The child solver is determined from the discretization technique. Finite volume discretization is used in this program, and the algebraic multigrid (AMG) linear solver is applied as the child solver. Thus, the discrete linear system is solved iteratively by the AMG solver.

Solvers	**- Implicit Unsteady** **- Partitioning** **- Segregated Flow** **- Segragated Energy** **- Time-Step Control**

Table 4.2: The solvers used in the CFD program.

STAR-CCM+ makes use of parallel processing, where the computational domain is divided into separate sections (sub-domains). Each sub-domains are assigned to a separate process. This is called domain decomposition. The partitioning solver ensures that the domain decomposition is up to date. Thus, the partition solver is the first solver to be invoked, before any physics solvers are invoked on a given iteration or time step.

Section	**Temperature (°C)**
Heat section	63
Heat rejection section	12
Ambient temperature	23
Across the solenoid	35

Table 4.3: Static temperatures.

The implicit unsteady solver controls the time step size and the update at each physical time for the calculation.

The segregated flow solver executes the task of controlling the solution update for the segregated flow model. Furthermore, the segregated flow solver controls two additional solvers, velocity solver and pressure solver. The velocity solver obtains the intermediate velocity field by solving the discretized momentum equation. The pressure solver updates the pressure field by solving the discrete equation for pressure correction. Both of them also control the under-relaxation factor and the AMG parameters for the momentum equation.

The segregated energy solver controls the solution update for the segregated fluid energy model. The solver defines the under-relaxation factor and the AMG parameter for the energy equation.

The time-step control solver sets the time-step properties for the two-time models used. In addition, the solver defines the CFL number and von Neumann number properties for the convective CFL time-step control model and the energy-based time-step control model, respectively.

4.0.7 Initial conditions

4.0.7.1 Pressure, velocity and static temperature

The initial condition for pressure and velocity was set to have a value of 0 Pa and (0, 0, 0) m/s respectively, and the method for both of them was set to constant. The initial condition for the static temperature was set through the method of a field function. The field function defined the temperature across the heat section and heat rejection section, the ambient temperature and the temperature across the solenoid due to its self-heating. The temperature properties are given in table 4.3.

The gravity was defined to be 9.81 m/s^2 in the positive y-direction.

4.0.7.2 Time-step and inner iterations

The time step in the simulation was set to 0.05 s. A smaller time step would increase the computational time. The temporal discretization was set to 1st-order, because 2nd-order are harder to stabilize [59]. Thus, the discretized grid flux is of the first order.

4.0.7.3 Under-relaxation factor

The under-relaxation factor can reduce the number of iterations and accelerate convergence [4]. In this thesis, the under-relaxation factor in the segregated flow and energy solvers was set to default values obtained from the STAR-CCM+ user guide [59]. Even though the chosen default factors are conservative, they lead to convergence in most cases [59].

4.0.8 Boundary conditions

The boundary conditions and some times also the initial conditions dictate the particular solution to be obtained from the governing equations [59]. Thermal boundary conditions of Neumann type were used, which control the values of flux at the boundary [23].

For the physics conditions in the regions, the momentum source option was selected to be specified. The physics values in the region for the momentum source were specified with the method of a field function. This field function in the momentum source accounted for the magnetic source from the solenoid. The magnetic field in the program is, therefore, a momentum source with the unit force per volume (N/m^3).

In this thesis, the geometry had wall and pressure outlet boundaries. A sketch showing the boundary conditions are visualized in Figure 4.3.

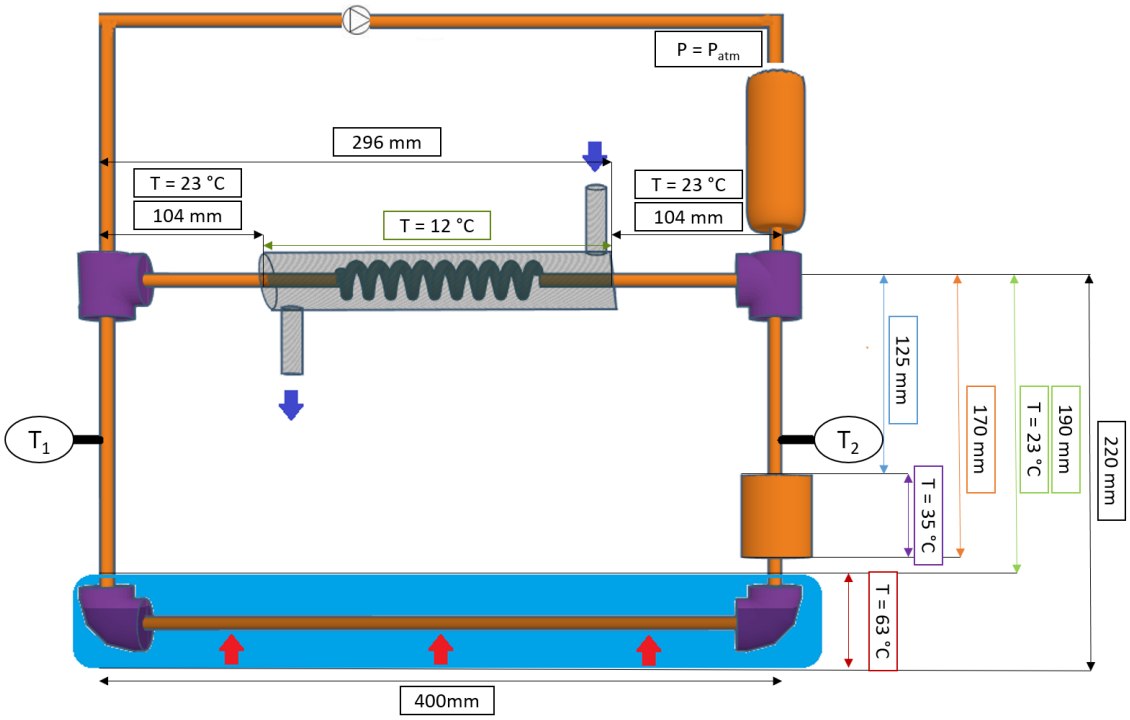

Figure 4.3: Scheme of the boundary conditions.

4.0.8.1 Wall boundaries

In the wall boundary, the following physics conditions were selected:

- Reference frame specification was set to region reference frame.
- Shear stress specification was set to no-slip.
- Tangential velocity specification was set to fixed.
- Thermal specification was set to convection.
- User wall heat flux coefficient specification was set to none.

Additionally, the following physics values were set for the wall boundary:

- Ambient temperature was set using the method of a field function. The field function used is the same as the function used for the static temperature in the initial conditions.
- Heat transfer coefficient was set using the method of a field function, where the heat transfer coefficient was set to 500, 250 and 25 for the heat rejecting section, heat section and ambient temperature respectively.

4.0.8.2 Pressure outlet boundary

In the pressure outlet boundary, the following physics condition was selected:

- Backflow specification was set to the boundary-normal direction and a environmental pressure.
- Pressure outlet option was set to none
- Reference frame specification was set to the lab frame.

In addition, the following physics values were selected for the pressure outlet boundary:

- Pressure was set to constant and 0 Pa.
- Static temperature was set using the method of a field function.

Chapter 5

Results

5.1 Uncertainty analysis

Mass, heat flux and temperature measurements, and velocity estimations included uncertainties concerning the procedure, set-up and instrumentation. The uncertainty of each of the instruments used to obtain the results is given in Table 5.1.

In the process of producing FF, the particles and distilled water were measured separately. Thus, calculated from the equations given in Appendix A, the uncertainty of the concentration of each sample was ± 0.0001 wt.%.

The distance between the glass tube and the lamp was measured with a tape measure with an uncertainty of ± 0.1 cm. The relative uncertainty of the measured distance of 6 cm and 8 cm are 1.7% and 1.3%, respectively. If the former and latter distance between the glass tube and the lamp decreased by 0.1 cm, the radiative heat flux, according to Eq. 3.2, would increase by 76.5 W/m^2 and 51.3 W/m^2, respectively. This would affect the resultant velocity by approximately 0.5%. For the analytical velocity calculations in the vertical and horizontal experimental cases, it should be noted that the merging of data variables led to an unavoidable experimental error. Therefore, the velocities stated in this thesis is given with the corresponding uncertainties, calculated by Eq. (A) from Appendix A.

Instrument	Manufacturer	Parameter	Uncertainty	Unit
Radiometer (LSS 122 IR)	Lingshang	Heat flux	± 1	W/m^2
T-type (HTMQSSIM100G150)	Omega	Temperature	± 0.1	°C
Weight scale (CPA 324S)	Sartorius	Mass	± 0.0001	g

Table 5.1: Instrumental uncertainties.

5.2 Experiments on vertical apparatus

A set of experiments were conducted to characterize the thermomagnetic convection of the flow loop. During the experiments, the ambient air, the thermal bath and the cold water through the heat exchanger maintained a temperature of 23°C, 63°C and 12°C, respectively. A set of experiments were done where both the concentration of the FF (Fe_2O_3-water) and the magnetic field strength were varied. The different concentrations investigated were 0.5 wt.%, 1.0 wt.%, 1.5 wt.% and 2.0 wt.%. The solenoid electrical currents of 1.26 A, 0.80 A and 0.40 A, were used to obtain different magnetic field strengths. By the use of Eq. (A.2), this corresponds to theoretical magnetic field strengths of 2.3×10^4 A/m, 1.4×10^4 A/m and 7.2×10^3 A/m, respectively.

When the fluid was changed to a different concentration, the whole loop system was dismantled and cleaned. It was first cleaned by soap and spring water before it was sonicated in ethanol.

5.2.1 Experimental procedure

Before each experiment, the apparatus was raised from the thermal bath, and the cold water supply to the heat exchanger together with the current supply for the solenoid were turned off. This was done to establish a uniform fluid temperature in the whole system. Next, the fluid was circulated through the system by the pump, to remove any air bubbles within the system. The apparatus was lowered into the thermal bath, and the cold water supply together with the current supply for the solenoid were turned on, to start an experiment. Each experiment was done for about 20 minutes, which was enough to achieve stable temperatures and stability in the system.

5.2.2 Temperature analysis

The relation between the magnetic field strength, concentration of the FF and measured temperatures were investigated in this subsection. The sensors T_1 and T_2 measured the temperatures after the heating and heat-rejection section, respectively. To better visualize the measured temperatures from the sensors T_1 and T_2, the temperature difference $(T_1 - T_2)$ was used.

To characterize the effect of thermomagnetic convection, the result from natural convection of water in the flow loop was used as a reference point. The result of water is shown as a red dotted line in Figures 5.1, 5.3, 5.4 and 5.5. Experiments with FF without an applied magnetic field were also conducted, to investigate how the FF at different concentrations was affected by natural convection.

5.2.2.1 Temperature distribution over time

Temperatures changes over time in the system due to mainly natural and thermomagnetic convection for the concentration of 1.0 wt.%, are shown in Figure 5.1. The measured temperatures for the other concentrations are found in Appendix C.1. Additionally, to get a better understanding of how the fluid temperature is distributed in the system, a thermographic camera was used. The IR picture in Figure 5.2 was of the experimental case with the concentration of 1.0 wt.% and a solenoid electrical current of 0.40 A, at 1090 seconds into the experiment. The recorded temperatures in Figure 5.1 at 1090 seconds show good agreement with the temperatures from the IR picture.

In Figure 5.1, the experimental cases with a concentration of 1.0 wt.% and various magnetic field strengths, exhibited temperature differences almost equal to the temperature differences of water. Thus, there is no clear indication of thermomagnetic convection taking place. However, a small difference in the recorded temperature differences occurred due to an increase in the magnetic field strength. This indicates that the FF with a concentration of 1.0 wt.% was influenced by the magnetic field, but to a very small extent.

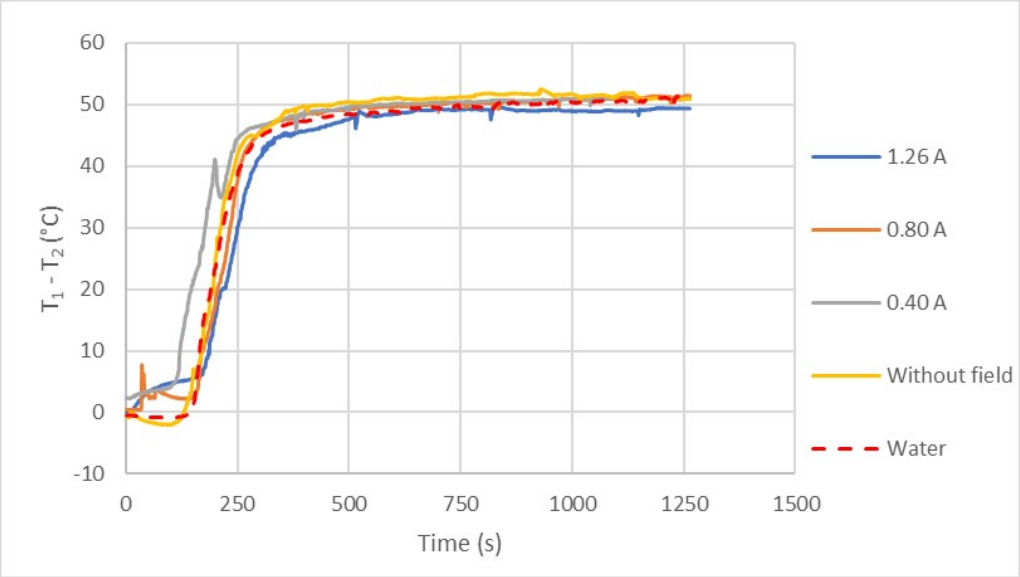

Figure 5.1: Temperature differences for 1.0 wt.% of Fe_2O_3, without and with different solenoid electrical currents.

Figure 5.2: Picture of the apparatus with a thermal camera, 1090 seconds into the experiment, for 1.0 wt.% of Fe_2O_3 and a solenoid electrical current of 0.40 A.

In Figure 5.3, the temperature differences of the different concentrations without an applied magnetic field are shown. Here, natural convection was the main heat transport mechanism. The concentration of 2.0 wt.% showed the lowest temperature differences. The average temperature difference of the specified concentration was equal to 33.8 ± 0.1°C. The base fluid (water) of the FF had an average temperature difference of 50.3 ± 0.1°C. This is similar to the results from Misale, Devia and Garibaldi [42]. For a similar system with only natural convection present and a heating rate of 10 W, they found that by increasing the concentration of Al_2O_3 from 0.5% to 3.0%, the average temperature difference decreased. The reason for this decrease in the temperature difference can be due to the viscosity increase. Li and Peterson [35] observed also that the effect of natural convection deteriorated when particles were added to the suspension. It is believed that the enhanced thermal conductivity will reduce the temperature gradient and the enhanced viscosity will increase the viscous drag and obstruction of fluid flow. This will play a role in slowing down the bulk movement of the nanofluids in natural convection by reducing the temperature gradient and advection momentum.

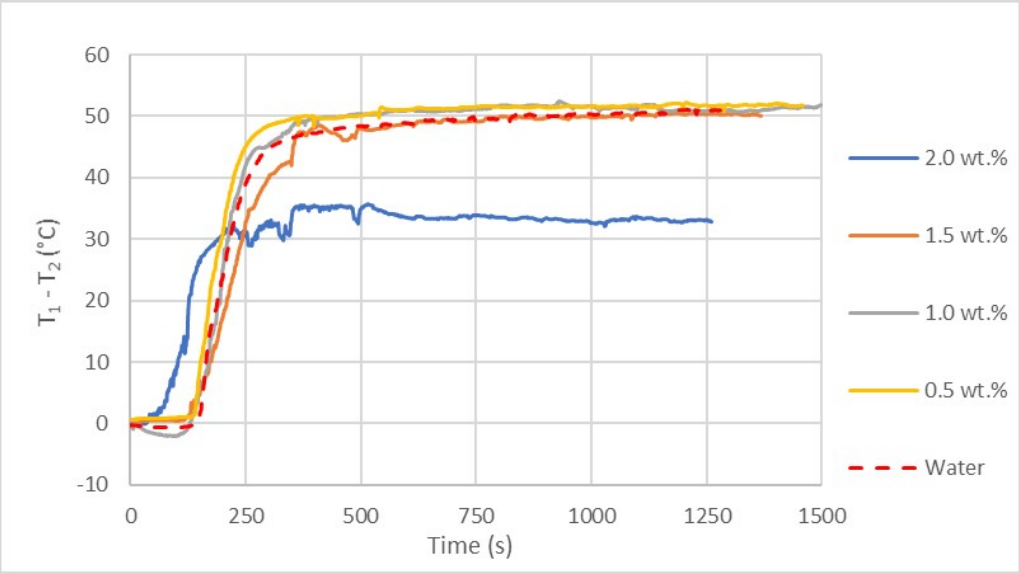

Figure 5.3: Temperature differences over time for different concentrations of Fe_2O_3 with no magnetic field present.

5.2.2.2 Concentration and magnetic field strength investigation

After the temperature differences had stabilized, an average temperature difference ΔT_{Avg} for the measured temperatures was estimated. Thus, by removing the time variable, better visualizations of how the concentration and the field strength affected the temperature difference in the FF were obtained.

Particle concentration.
Figure 5.4 shows that an increase in the concentration produces usually a lower average temperature difference, except for the change in the concentration from 1.5 wt.% to 2.0 wt.% with the strongest field strength of 1.26 A. The concentration change from 0.5 wt.% to 1.0 wt.% had little impact on the average temperature difference. In contrast, the concentration change from 1.0 wt.% to 1.5 wt.% and to 2.0 wt.% had a distinct impact on the average temperature difference. A lower average temperature difference due to an increased fluid concentration was also found by Chaudhary et al. [15]. This supports that an increased concentration has a tendency to decrease the average temperature difference.

The largest change in temperature difference by increasing the concentration was found for the solenoid electrical current of 1.26 A. For the experimental cases with the specified magnetic field strength, by altering the concentration from 0.5 wt.% to 1.5 wt.%, caused the average temperature difference to decrease from 50.1 $\pm$ 0.1°C to 7.5 $\pm$ 0.1°C respectively. This corresponds to a temperature difference decrease of 85.0%.

At higher concentrations, during the influence from an external magnetic field, more particles with a magnetic dipole moment will attempt to be aligned with the field. Thus, the magnetic dipole moment density is increased, which enhances both the fluid magnetization and susceptibility. This is seen from Eq. (2.6) and Eq. (2.9), by increasing the concentration. In this process, magnetic energy and thermal energy are competing between magnetizing or demagnetizing the FF. A larger gradient between the magnetic and thermal energy induces a stronger thermomagnetic force gradient. By increasing the concentration, the fluid is magnetized to a larger extent, which enhances the magnetic energy and the Kelvin body force from Eq. (2.15). This results in a higher thermomagnetic force gradient, and a stronger thermomagnetic pumping force [52]. The enhanced pumping force caused the fluid volume element to be exposed to the heating section for a shorter time. Thus, the fluid volume element absorbs less heat and the temperature difference drop. This corresponds to a higher fluid velocity which will be discussed in section 5.2.3.

Magnetic field strength.
Figure 5.5 shows that an increase in the magnetic field strength, regardless of the FF concentration, produce a lower average temperature difference. This is equivalent to the results found by Chaudhary et al. [15] and Moghaddam [33], where an increased magnetic field strength, in both of the studies, induced a lower average temperature difference. The change of solenoid electrical current from 0.4 A to 0.8 A, for all the experimental cases, had little impact on the average temperature difference. Furthermore, for the experimental cases with the concentrations of 0.5 wt.%, 1.0 wt.% and 2.0 wt.%, by changing the solenoid electrical current from 0.8 A to 1.26 A, the average temperature difference for each case decreased slightly

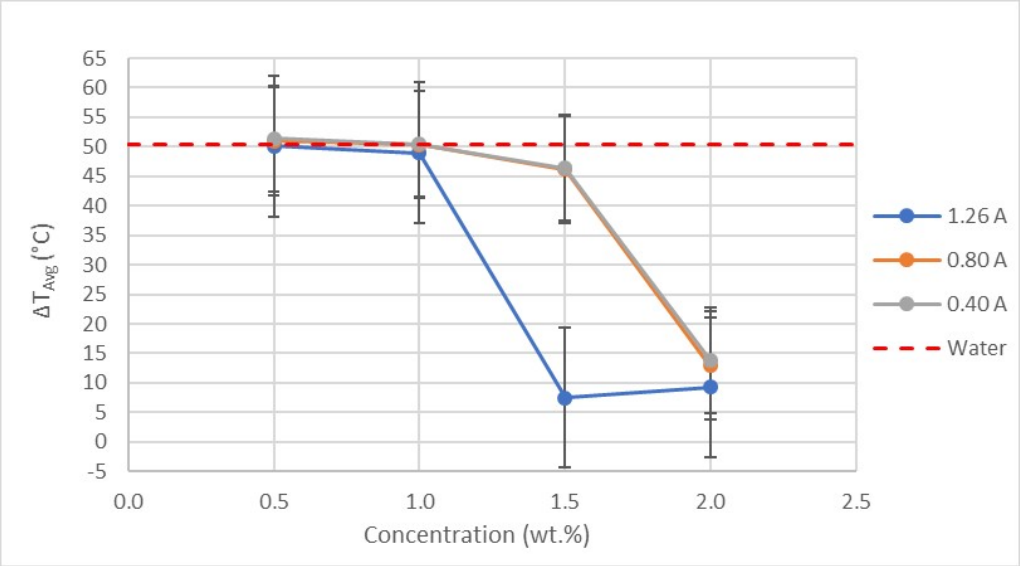

Figure 5.4: Average temperature differences as a function of the concentration for different solenoid electrical currents.

more. For the experimental case with concentration of 1.5 wt.%, by changing the solenoid electrical current from 0.8 A to 1.26 A, a distinct decrease in the average temperature difference was observed.

When a magnetic field is applied, the direction of the magnetic dipole moment of the particles will attempt to be aligned with the magnetic field direction. This is explained by the magnetic moments that rotate towards the minimum energy direction, which is parallel to the magnetic field. With increasing magnetic field strength, the number of particles with a magnetic dipole moment aligned with the magnetic field increases. Thus, at a stronger magnetic field strength, the density of aligned magnetic dipole moments increases, which enhances the fluid magnetization. This is seen from Eq. (2.6), by increasing the magnetic field strength. In this process, magnetic energy and thermal energy are competing between magnetizing or demagnetizing the FF. A larger gradient between the magnetic and thermal energy induces a stronger thermomagnetic force gradient. By increasing the magnetic field strength, the fluid is magnetized to a larger extent, which enhanced the magnetic energy and the Kelvin body force from Eq. (2.15). This results in a higher thermomagnetic force gradient, and a stronger thermomagnetic pumping force [52]. The enhanced pumping force caused the fluid volume element to be exposed to the heating section for a shorter time. Thus, the fluid volume element absorbs less heat and the temperature difference drop. This corresponds to a higher fluid velocity.

The largest change in temperature difference by increasing the magnetic field strength was found for experimental case with the concentration of 1.5 wt.%. At the specified

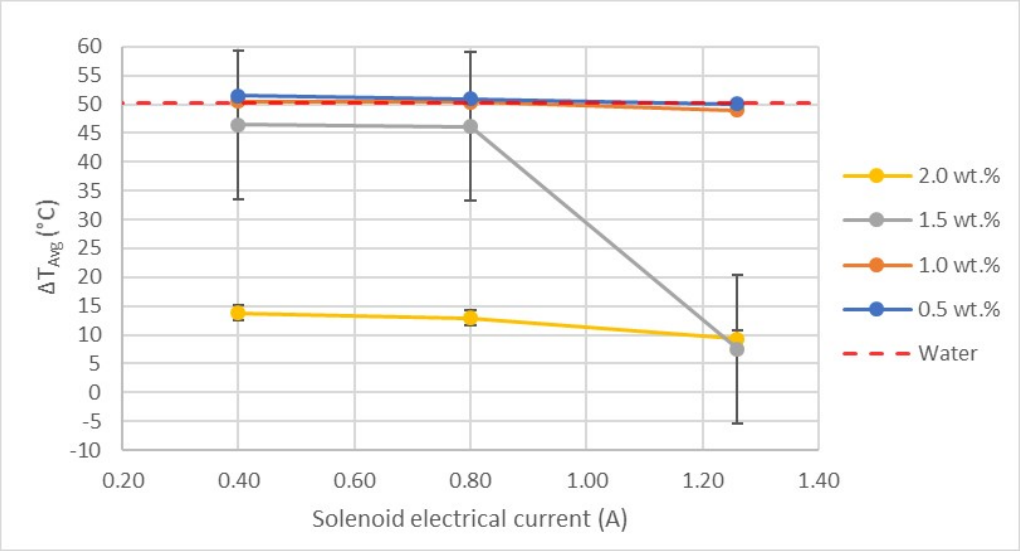

Figure 5.5: Average temperature differences as a function of the solenoid electrical current for different concentrations.

experimental case, by altering the solenoid electrical current from 0.40 A to 1.26 A, the average temperature difference decreased from 46.4 ± 0.1°C to 7.5 ± 0.1°C. This corresponds to a temperature difference decrease of 83.8%.

The experimental case with concentration of 1.5 wt.% and a solenoid electrical current of 1.26 A produced the lowest average temperature difference equal to 7.5 ± 0.1 °C. The average temperature difference for the specified experimental case was decreased by 85.1% compared to water.

5.2.3 Velocity analysis

The fluid velocity was calculated for each case using the measured temperatures, along with the constant temperatures of the heat and heat-rejection section. Higher fluid velocities in the flow loop arise from enhanced thermomagnetic convection which induces a better cooling performance [33][52].

5.2.3.1 Procedure for obtaining fluid velocity from CFD

The Kelvin body force (N/m^3) arising from the interaction between the fluid magnetization and magnetic field for each experimental case was unknown. In the CFD program, the Kelvin body force was represented by an applied momentum source (N/m^3). Therefore, to obtain a simulated temperature distribution in the CFD program, a momentum source needed to be assumed. Each momentum source corresponded to a particular average temperature difference. The correct momentum

source was assumed when the simulated average temperature difference was approximately equal to the experimental average temperature difference. When the former and latter average temperature differences corresponded, the fluid velocity could be read from the CFD program.

The CFD program was used for the experimental cases where thermomagnetic convection significantly influenced the system. The experimental cases which were simulate in the CFD program are shown in Table 5.2. Additionally, for each experimental case, Table 5.2, shows the correctly assumed momentum source, the corresponding simulated temperature difference, the corresponding simulated fluid velocity and the experimental temperature difference. The experimental cases not mentioned in Table 5.2 were difficult to obtain in the CFD program, because a very low applied momentum source corresponding to the low influence of thermomagnetic convection was required.

Mass fraction (wt.%) of Fe_2O_3	**solenoid electrical current (A)**	**Momentum source (N/m^3)**	**$\Delta T_{Experiment}$ (°C)**	**ΔT_{CFD} (°C)**	**Fluid velocity (m/s)**
2.0	1.26	6080	9.3 ± 0.1	9.3	0.07478
	0.80	4080	12.9 ± 0.1	12.9	0.05455
	0.40	3725	13.8 ± 0.1	13.8	0.05118
1.5	1.26	7800	7.5 ± 0.1	7.5	0.09091

Table 5.2: The specified concentrations, solenoid electrical current, experimental temperature differences, the correctly assumed momentum sources, the corresponding simulated temperature differences and fluid velocities are shown.

5.2.3.2 Investigation and comparison of the simulated and estimated fluid velocities

The analytical and simulated velocities were used to illustrate a qualitative difference between the natural and the thermomagnetic convection. Only the natural convection was accounted for in the analytical velocity calculation. Conversely, the fluid velocities obtained by the CFD program included the thermomagnetic convection. Thus, with an increased influence from thermomagnetic convection, the deviation between the analytical fluid velocity and the simulated fluid velocity increased. The analytical and simulated velocities are used to illustrate a qualitative difference between the natural and the thermomagnetic convection.

Figure 5.6 shows that all experimental cases were within the laminar flow range (Re < 2100) [40], which complies with the assumption in the velocity estimates.

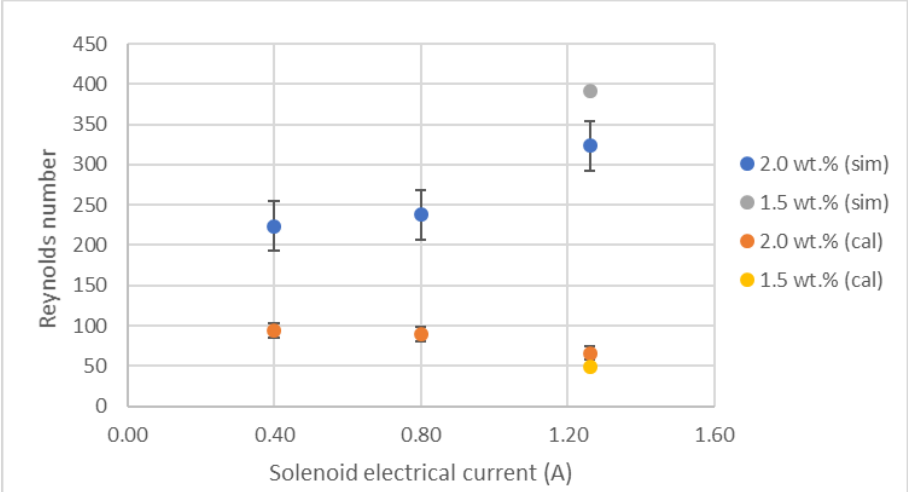

Figure 5.6: Reynolds numbers for both the analytically calculated velocities and simulated velocities are shown. The notations "sim" and "cal" stands for the Reynolds number obtained from the simulated and calculated velocities respectively.

Temperature difference.
In Figure 5.7, the fluid velocity vs the temperature difference of the fluid, for the experimental case with a concentration of 2.0 wt.%, follows an almost linear relation, and applies for both the simulated velocities and the analytically calculated velocities. The simulated fluid velocities decreased with increasing average temperature differences. The same results were found by Moghaddam [33], where a higher average temperature difference corresponded to a lower fluid velocity. However, for the analytically calculated fluid velocities, the velocity increased with increasing average temperature differences. This is because the buoyancy force becomes stronger at more significant temperature differences, and induces an enhanced natural convection and a higher fluid velocity.

In Figure 5.7, the average temperature difference at points 1 and 4 were equal to 9.3 $\pm$ 0.1°C. The fluid velocity from natural convection at point 4 was equal to 15.0 $\pm$ 2.6 mm/s. By applying a magnetic field with a solenoid electrical current of 1.26 A, the fluid velocity increased to 74.8 mm/s (point 1), which obtained the same temperature difference as in point 4. Hence, the fluid velocity increased by 398.7 $\pm$ 0.7 % from point 4 to point 1. At lower magnetic field strengths (points 2 and 3), the fluid velocity increased to a smaller extent compared to the fluid velocity from natural convection (points 5 and 6). Nevertheless, for the experimental cases with a concentration of 2.0 wt.%, a distinct fluid velocity increase was observed by applying a magnetic field.

Particle concentration.
Visualized in Figure 5.8, with a constant solenoid electrical current of 1.26 A, the

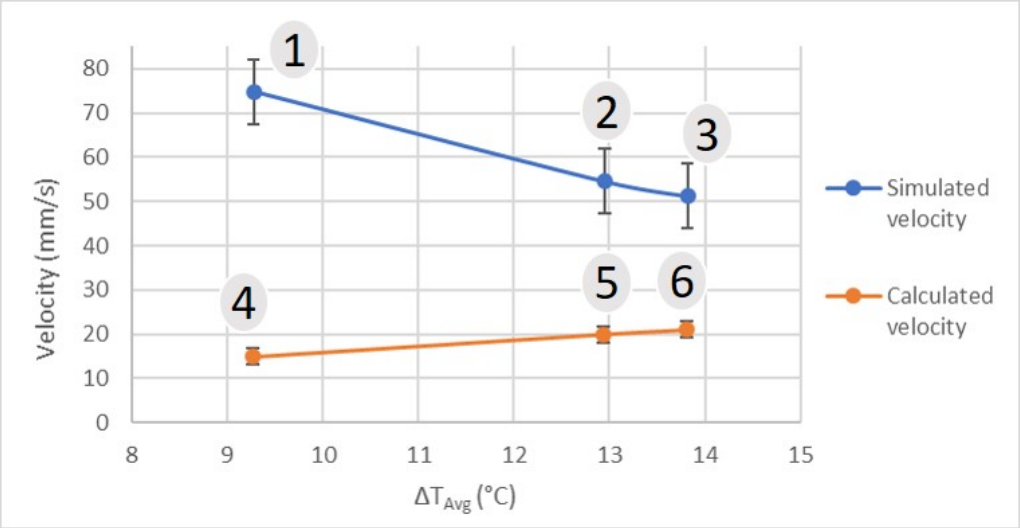

Figure 5.7: Fluid velocity as a function of the average temperature difference, for the concentration of 2.0 wt.%. Points 1 and 4 corresponds to the fluid velocity with solenoid electrical current of 1.26 A, points 2 and 5 corresponds to the fluid velocity with solenoid electrical current of 0.80 A and Points 3 and 6 corresponds to the fluid velocity with solenoid electrical current of 0.40 A.

simulated fluid velocity reduced when the concentration increased from 1.5 wt.% to 2.0 wt.%. The explanation originates most probably from the increase in the obstruction of flow from the fluid viscosity. The addition of more particles into the fluid increased the fluid viscosity. Furthermore, at higher concentrations, during the influence from an external magnetic field, the fluid magnetization and subsequently the susceptibility increases. This results in a higher thermomagnetic force gradient and a stronger thermomagnetic pumping force [52]. However, in Figure 5.8, the fluid velocity decreased at higher concentrations. At steady-state condition, the fluid velocity is determined from the balance between the driving and the resisting forces. Thus, for the concentration of 1.5 wt.% compared to 2.0 wt.% with a solenoid electrical current of 1.26 A, the increase in the thermomagnetic pumping force (driving force) was smaller than the fluid viscosity (resisting force) increase. Hence, the fluid velocity decreased due to the increased viscous drag throughout the whole circulation path.

From the simulated results, a decreased temperature difference originated from a higher fluid velocity. In Figure 5.4, by increasing the concentration while keeping the magnetic field strength constant, the average temperature difference decreased for all cases except for the experimental case mentioned in the previous paragraph. Thus, by increasing the concentration, the most common tendency was an increased fluid velocity.

The analytically calculated velocity of 2.0 wt.% of Fe_2O_3 increased compared to

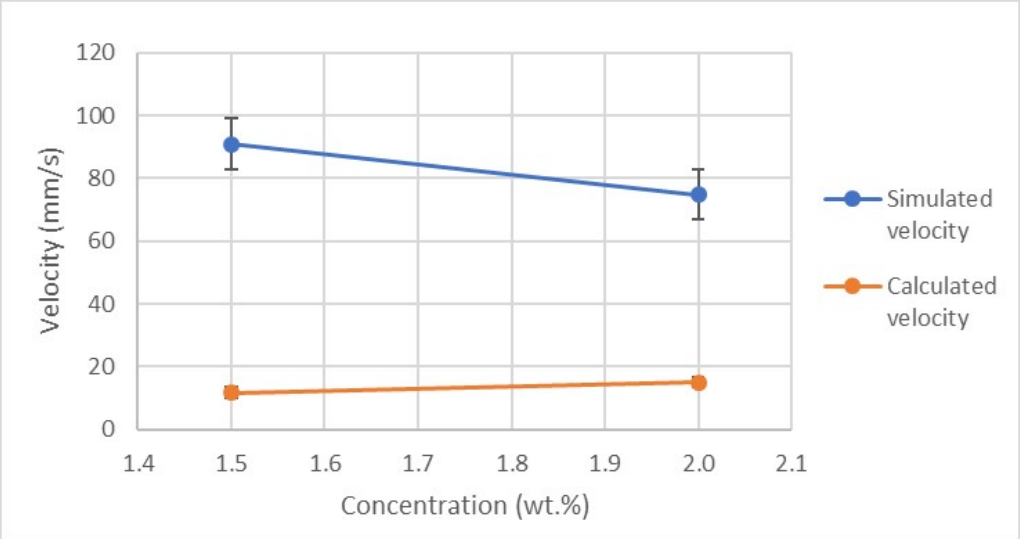

Figure 5.8: Fluid velocity as a function of the concentration, with a solenoid electrical current of 1.26 A.

the velocity of 1.5 wt.% of Fe_2O_3. As previously stated, this is due to a higher measured temperature difference in the former case compared to the latter case. Higher temperature differences enhance the natural convection effect, and the fluid velocity is increased.

At the concentration of 1.5 wt.%, the fluid velocity from natural convection was equal to 11.7 $\pm$ 2.2 mm/s. By applying a magnetic field with a solenoid electrical current of 1.26 A, the fluid velocity increased to 90.9 mm/s. This correspond to a fluid velocity increase of 676.9 $\pm$ 1.3 %, due to the influence of thermomagnetic convection.

Magnetic field strength.
In Figure 5.9, the simulated fluid velocity increased with increasing magnetic field strength. A similar result was also found by Moghaddam [33], where the fluid velocity increased due to an enhanced magnetic field strength. The fluid is magnetized to a larger extent, by increasing the magnetic field strength, which enhances the magnetic energy and the Kelvin body force from Eq. (2.15). This results in a higher thermomagnetic force gradient, and a stronger thermomagnetic pumping force [52]. Thus, a stronger magnetic field strength produced a stronger thermomagnetic pumping force and a higher fluid velocity was observed. The enhanced fluid velocity induces a better cooling performance [33]. A rise in the solenoid electrical current from 0.40 A to 1.26 A with the concentration of 2.0 wt.%, caused an enhanced fluid velocity of 46.1% from 51.2 mm/s to 74.8 mm/s.

In Figures 5.7 - 5.9, it can be noted that the calculated and simulated fluid velocities

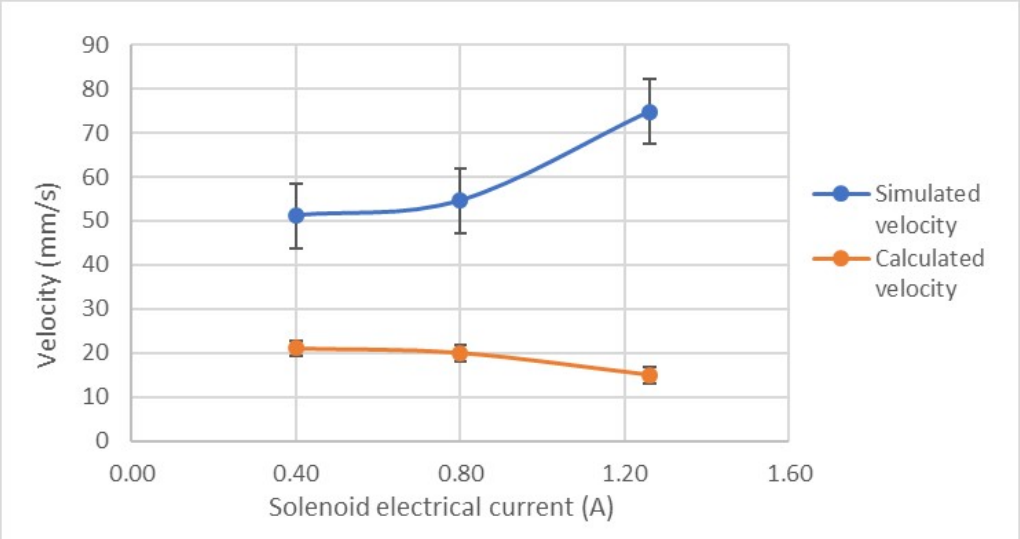

Figure 5.9: Fluid velocity as a function of the solenoid electrical current, for the concentration of 2.0 wt.%.

are in the same order, millimeter per seconds. Hence, the analytically calculated fluid velocities is a reasonably good approximation of the fluid velocities.

The line for the analytically calculated velocities has a negative gradient, observed in Figure 5.9. This is in line with what has been discussed previously. With an increased magnetic field strength, the thermomagnetic convection has a more significant influence on the fluid velocity. Thus, the deviation between the calculated and simulated velocity will increase accordingly.

5.3 Evaluation of the CFD results

5.3.1 Temperature profile and velocity profile

Figure 5.10, compares the simulated temperature differences with the experimental temperature differences over time, for 1.5 wt.% of Fe_2O_3. The same comparison for the experimental cases of 2.0 wt.% of Fe_2O_3 can be seen in Appendix D.1. It shows that the simulated temperatures fluctuated in the beginning, but become more stable over time.

The flow loop was not a completely closed system due to the expansion tank. Disturbance from the expansion tank on both the temperature profile and the fluid velocity profile was expected. However, how the expansion tank would affect the temperature and velocity profile were unclear. Therefore, this was investigated by the CFD program. The temperature and velocity profile of 1.5 wt.% of Fe_2O_3 with

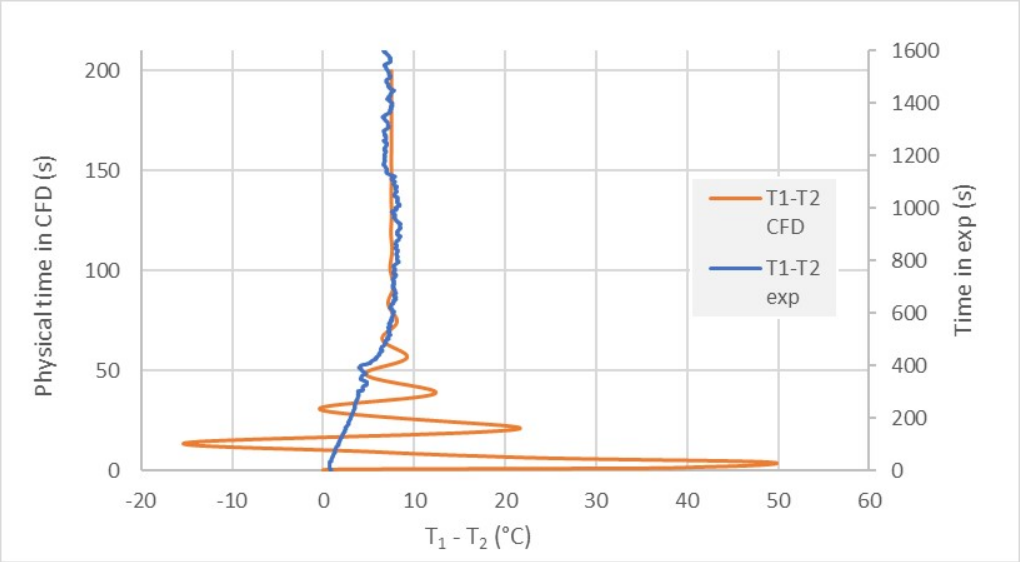

Figure 5.10: The simulated and experimental temperature differences over time for 1.5 wt.% of Fe_2O_3 with a solenoid electrical current of 1.26 A.

1.26 A as the solenoid electrical current, are visualized in Figure 5.11 and 5.12 respectively. For the other experimental cases, see the Appendices D.2 and D.3. It can be noted that the temperature profile (Figure 5.11) qualitatively corresponds to the temperature profile from the IR-picture (Figure 5.2).

In Figure 5.11, the temperature profile shows that the expansion tank influenced the fluid temperature insignificantly. A colder fluid has a weaker buoyancy force compared to a warmer fluid. Thus, the cold fluid at the expansion tank tends to flow downwards. Additionally, heat transfer by thermal conductivity takes place. Hence, a distinct local fluid temperature in the expansion tank was not established.

Figure 5.13 and 5.14 show the fluid velocity profile of the lower-left and the upper-right bend of Figure 5.12, respectively. The direction of the fluid flow in the apparatus was clockwise. The lowest and highest velocities were found at the inner and outer bend, respectively. The change in the direction of the fluid flow produces both friction and momentum exchange, which caused the fluid velocity to change in the bend [58].

The different fluid velocities at the outer and inner bend arise from the centrifugal force. When a fluid flows through a bend, a radial pressure gradient is developed due to the centrifugal force acting on the fluid. Because of the developed radial pressure gradient, the pressure near the outer and inner wall of the bend increases and decreases respectively. The pressure gradient near the outer wall in the bend and near the inner wall just after the bend can generate flow separation at these points, which leads to a pair of counter-rotating vortices [20].

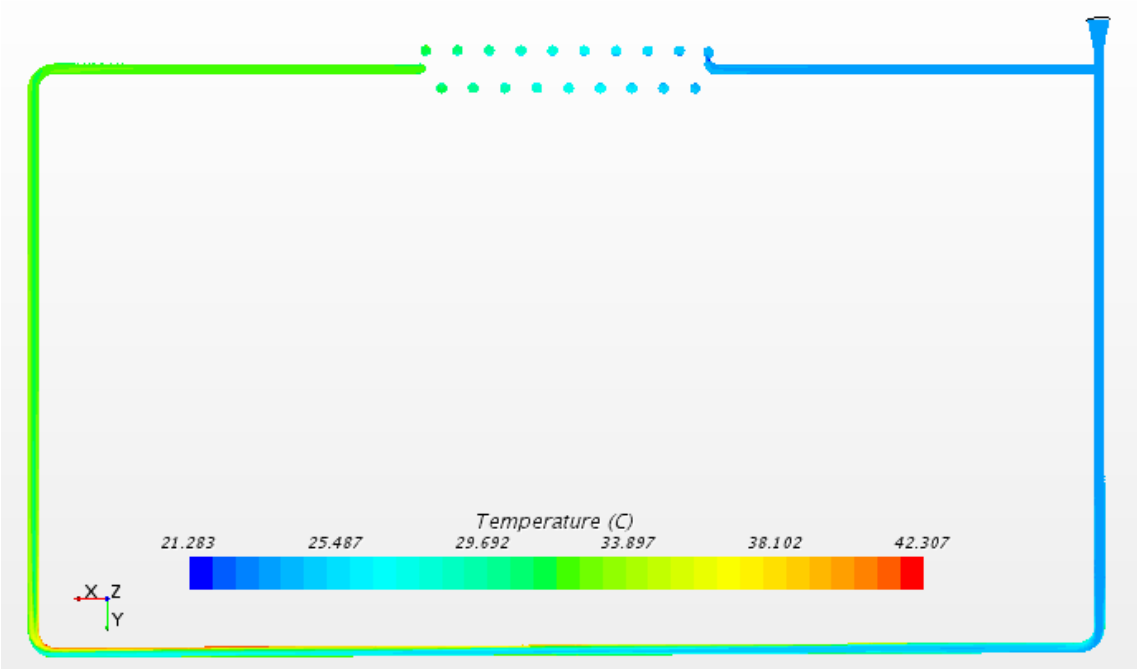

Figure 5.11: Temperature profile on the geometry for 1.5 wt.% of Fe_2O_3 with a solenoid electrical current of 1.26 A, after 200 s in physical time in CFD.

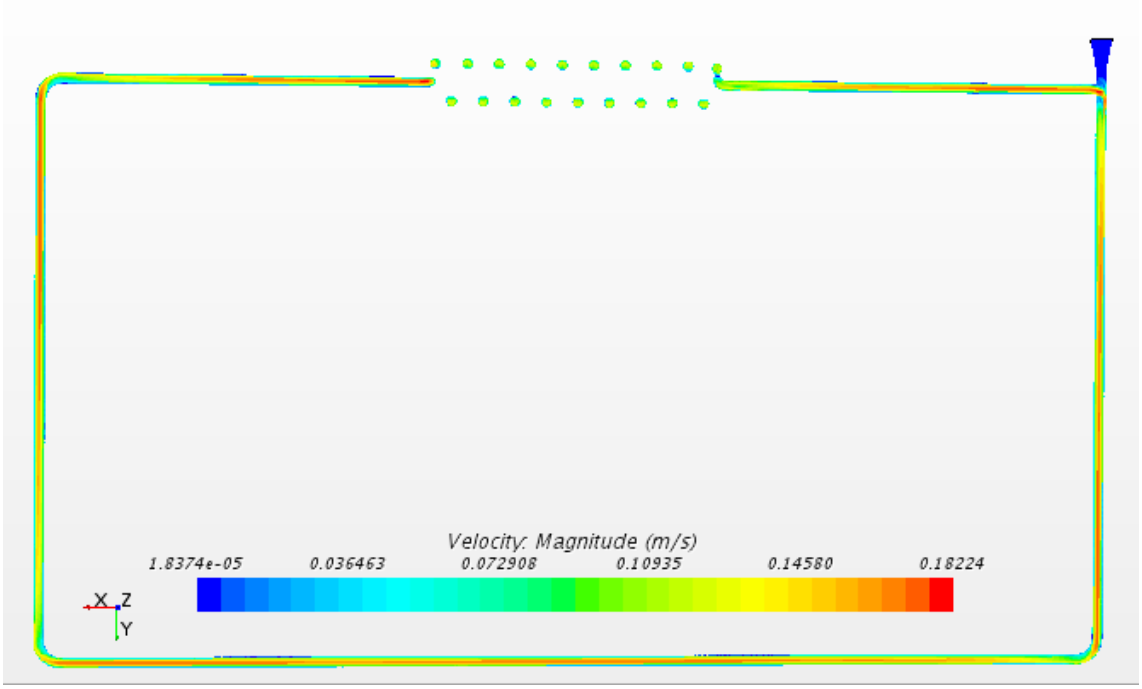

Figure 5.12: Velocity profile on the geometry for 1.5 wt.% of Fe_2O_3 with a solenoid electrical current of 1.26 A, after 200 s in physical time in CFD.

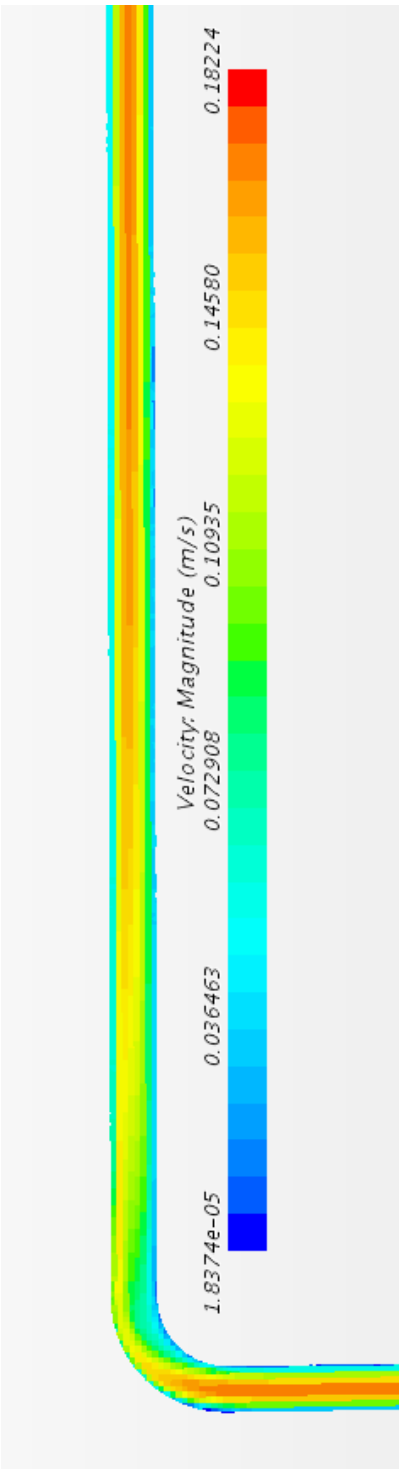

Figure 5.13: Velocity profile of the lower-left bend of the apparatus, for 1.5 wt.% of Fe_2O_3 with a solenoid electrical current of 1.26 A, after 200 s in physical time in CFD.

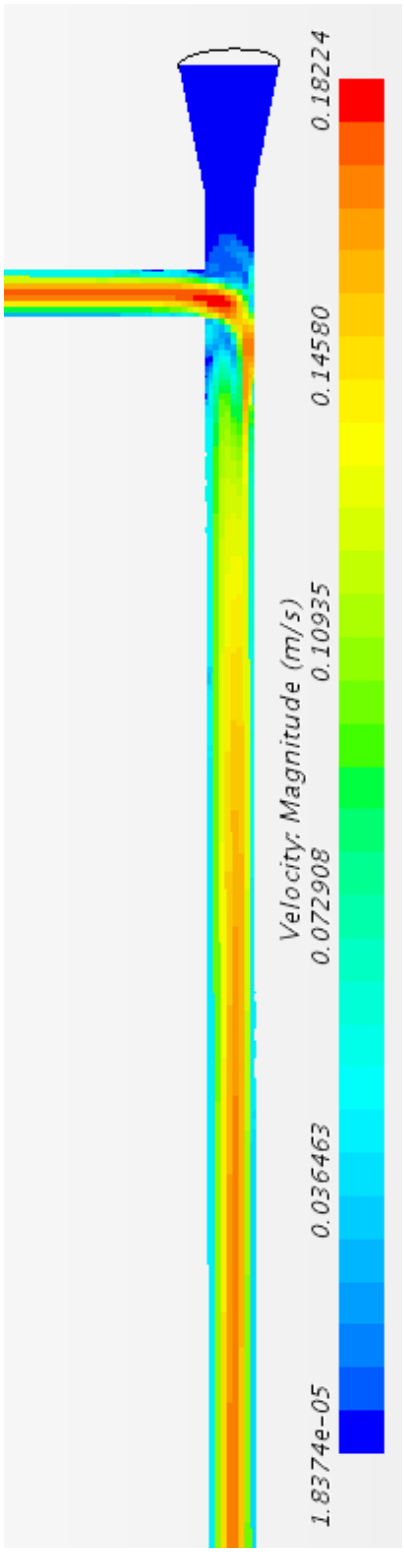

Figure 5.14: Velocity profile of the upper-right bend of the apparatus, for 1.5 wt.% of Fe_2O_3 with a solenoid electrical current of 1.26 A, after 200 s in physical time in CFD.

Figure 5.14 shows the bend where the expansion tank was present. As mentioned, the direction of the fluid flow in the apparatus was clockwise. Here, the outer wall in the bend was replaced by an expansion tank. The atmospheric pressure and the fluid in the expansion tank hinders the fluid flow to exit through the tank and forced the fluid flow to circulate in the loop. The lowest and highest velocities were found at the inner and outer bend respectively, but to a greater extent compared with the other three bends. This was seen from the red and blue fields observed just after the bend, which also indicated a more significant presence of vortices. Additionally, some velocity changes were found at the lower end of the expansion tank. This demonstrates the presence of small vortices, which affected just the lower part of the expansion tank. Nevertheless, the expansion tank affected the velocity profile in the bend to a small extent compared to the velocity profile at the other three bends.

5.3.2 Kelvin body force

The influence of Kelvin body force on the fluid at varying magnetic field strengths for 2.0 wt.% of Fe_2O_3, is shown in Table 5.2. It must be mentioned that the Kelvin body force (momentum source) is defined from the CFD program and not measured. With a stronger magnetic field strength followed an increased magnetization, and the Kelvin body force on the fluid enhanced [52]. This is in line with the Kelvin body force equation (Eq. (2.15)), which states that a stronger fluid magnetization induces a stronger Kelvin body force.

However, in Table 5.2, the Kelvin body force decreased at a higher particle concentration. This contradicts the fact that an increase in the concentration results in an enhanced fluid magnetization which subsequently generate an enhanced Kelvin body force when exposed to a magnetic field [69][52]. The answer to this contradiction lies in the setup of the CFD program. The properties of the fluid simulated were assumed to be equal to water. Thus, the change in fluid properties such as fluid viscosity was not accounted for, when particles were added to the solution. This assumption is a source of error, which affected the results.

5.4 Experiments on horizontal apparatus

A set of experiments were conducted with the apparatus in a horizontal orientation to characterize the thermomagnetic convection of the flow loop. With the apparatus in a horizontal orientation, the natural convection was sufficiently reduced. The temperature distribution in the system changed over time because of the influence of thermomagnetic convection, which circulated the fluid in the flow loop. During the experiments, the ambient air and the cold water through the heat exchanger maintained a temperature of approximately 23°C and 12°C, respectively. The source of heat was changed to a halogen lamp, which turned the apparatus into a DASC.

The distances between the lamp and the apparatus investigated were 6 cm and 8 cm. The radiating heat flux of the former and latter distances were 6961 W/m^2 and 5695 W/m^2 respectively, estimated by Eq. (3.2).

When the fluid concentration was changed, the whole loop system was dismantled and cleaned. It was first cleaned by soap and spring water before it was sonicated in ethanol.

5.4.1 Experimental procedure

The apparatus was placed on poles of equal heights to obtain the horizontal direction. Before each experiment, the solenoid electrical current, halogen lamp and the cold water for the heat exchanger were turned off, to establish a uniform temperature in the system. The fluid was circulated with a fluid pump to prevent bubbles in the system before each experiment. To start of an experiment, the cold water, solenoid electrical current and halogen lamp were turned on at the same time. Each experiment was conducted for about 1 hour (3600 s), to achieve stable temperatures and stability in the system.

5.4.2 Temperature analysis

The relation between the magnetic field strength, the fluid concentration and the measured temperatures were investigated in this section. As stated in section 5.2.2, to better visualize the measured temperatures of sensor T_1 and T_2, the temperature difference $(T_2 - T_1)$ was used. The sensors T_1 and T_2 measured the temperatures after the heat-rejecting and heating section, respectively.

5.4.2.1 Temperature distribution over time

How the temperature difference changed over time in the system for the experimental cases with a concentration of 2.0 wt.% and different magnetic field strengths and applied heating rates, are shown in Figure 5.15. The measured temperatures for the other experimental cases are found in Appendix E.1. The temperature differences exhibit that fluid flow was present, which revealed the influence of thermomagnetic convection.

Ideally, the apparatus should be completely horizontal with no effect from natural convection present. The light source should irradiate uniformly on the middle of the glass tube. If a magnetic field is not present, only conductive heat transfer should occur. Thus, an equal amount of heat would be conducted through the fluid to the two temperature sensors, and the measured temperature differences should be zero degree Celsius. However, this is not the case. The fluid always has some small local resistances, which influence the fluids ability to conduct heat. The lamp was

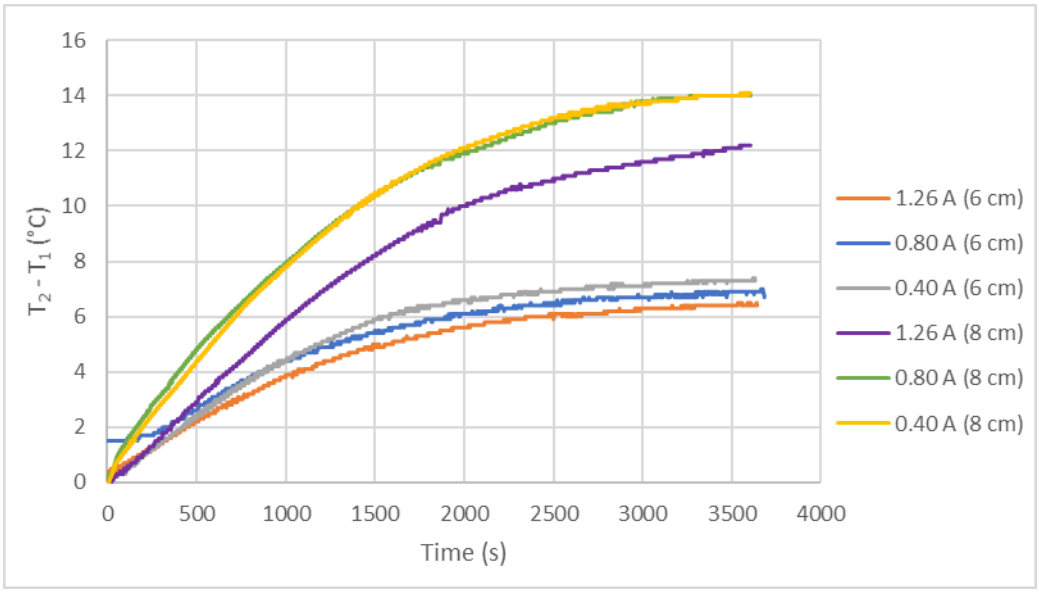

Figure 5.15: Temperature differences for the concentration of 2.0 wt.% with different solenoid electrical currents and irradiation distances.

measured to radiate on the middle of the glass tube, and the apparatus was measured to be in level, but some discrepancy exists. A weak effect of natural convection could arise due to the discrepancy mentioned above. However, the apparatus was placed prefixed poles, which was measured to be in level, to eliminate this to the best possible extent.

Experiments without an applied magnetic field were conducted to investigate the influence of thermal conduction. These experiments with the two predefined heat fluxes are visualized in Figure 5.16 and 5.17. As expected, for both the heat fluxes, the temperature differences for all of the experimental cases were not zero degree Celsius. All of the experimental cases without an applied magnetic field had temperature differences between 2°C and -2°C. This was acceptable and will influence the results to a small extent.

In Figure 5.18, the experimental cases with a concentration of 0.5 wt.%, an irradiation distance of 6 cm and the solenoid electrical currents of 1.26 A and 0.80 A showed fluctuations. The presence of these fluctuations is undesirable and are most probably caused by evaporation, due to visual observations of tiny bubbles. Fluctuations of this magnitude were only registered for the aforementioned experimental cases. The reason why fluctuations only happened for these cases can possibly be due to the fluid velocity. The fluid volume element over the radiated zone had such a low velocity that it was irradiated long enough to begin evaporating. Additionally, the thermal conductivity is lower for smaller concentrations. Hence, the ability of the fluid to conduct heat was also reduced, and local heat build-up could occur. During

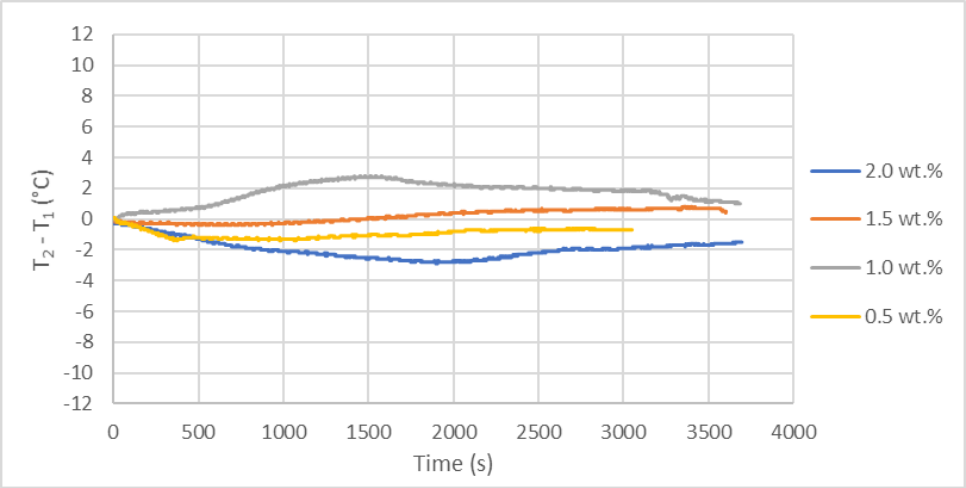

Figure 5.16: Temperature differences of different concentrations, without a magnetic field, 6 cm from lamp.

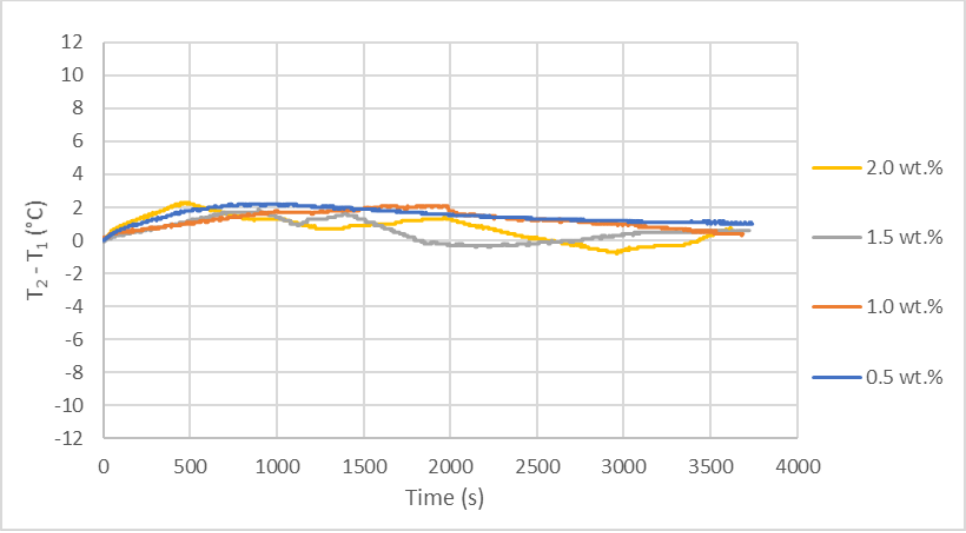

Figure 5.17: Temperature differences of different concentrations, without a magnetic field, 8 cm from lamp.

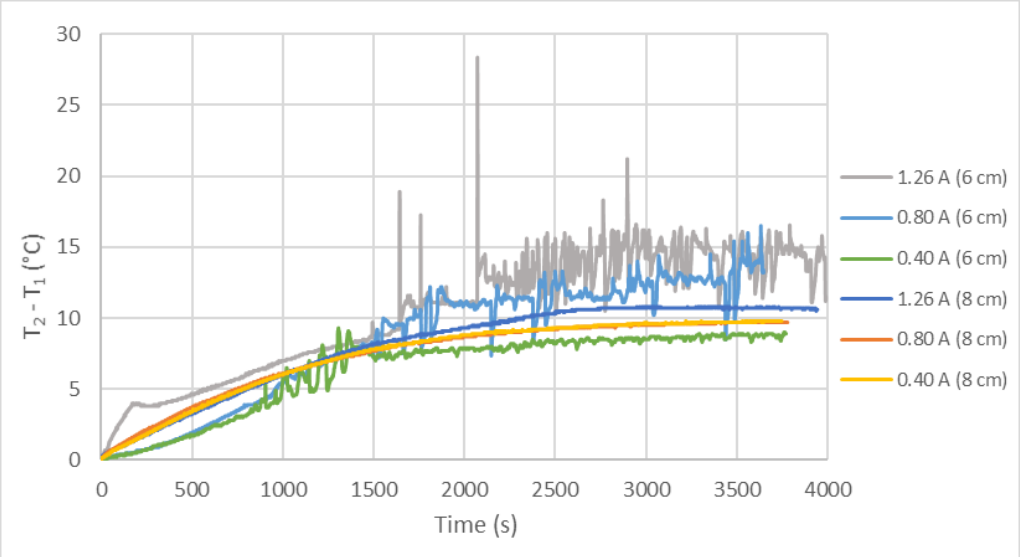

Figure 5.18: Temperature differences for the concentration of 0.5 wt.% with different solenoid electrical currents and irradiation distances.

evaporation, the amount of base fluid will decrease due to the generated steam, but the same amount of particles will remain in the suspension. Thus, the concentration of the fluid is influenced by evaporation. Additionally, the hot steam does not possess the magnetic properties of the FF. Hence, the magnetic field cannot induce a thermomagnetic force on the steam. These experimental cases were overlooked in further discussions.

5.4.2.2 Magnetic field strength, concentration and heat flux investigation

Particle Concentration.
Figure 5.19 shows that by increasing the concentration from 0.5 wt.% to 1.0 wt.% for both the irradiation distances, the temperature difference increased for all of the experimental cases, regardless of the magnetic field strength. For the cases with an irradiation distance of 8 cm, the average temperature difference also increased by altering the concentration from 1.5 wt.% to 2.0 wt.%, regardless of the field strength. These temperature difference increases can possibly be explained by the viscosity increase that follows from adding more particles into the suspension [43]. How the velocity is influenced is addressed later in section 5.4.3. Nevertheless, if the velocity decreases, the fluid volume element over the radiation zone irradiates over a longer time, which causes the fluid volume element to absorb more heat. This can cause the temperature difference to increase.

In Figure 5.19, by increasing the concentration from 1.0 wt.% to 1.5 wt.%, regardless

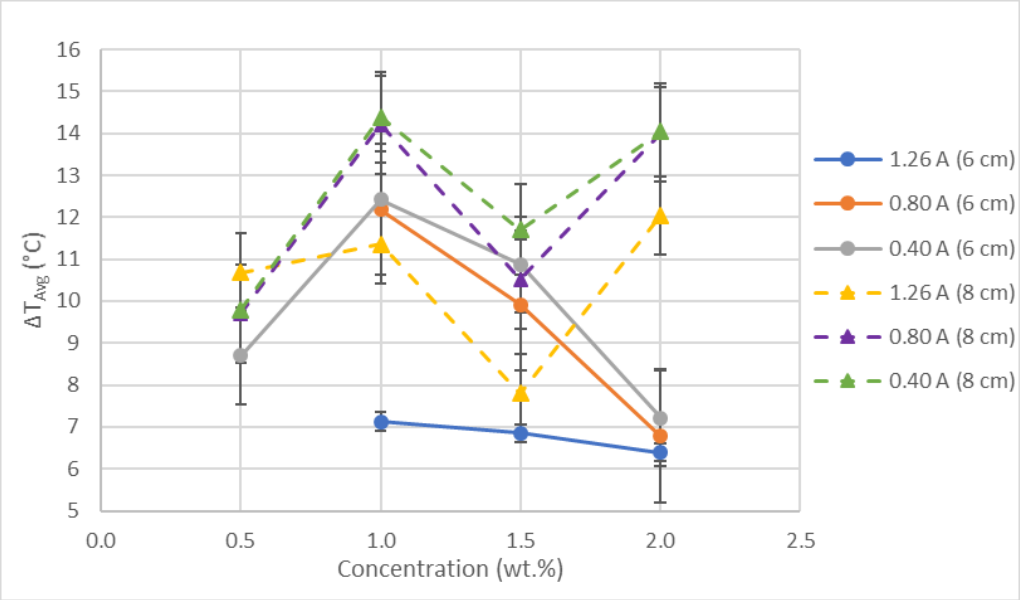

Figure 5.19: Average temperature differences as a function of the concentration for different solenoid electrical currents and irradiation distances.

of the irradiation distance and magnetic field strength, generated lower average temperature differences for all of the experimental cases. In addition, by increasing the concentration from 1.5 wt.% to 2.0 wt.%, the experimental cases with an irradiation distance of 6 cm, generated lower average temperature differences, regardless of the magnetic field strength. An increase in the concentration results in a higher thermomagnetic force gradient and a stronger thermomagnetic pumping force [52]. Hence, the fluid velocity increased, and the fluid volume element over the radiation zone was irradiated for a shorter time period. Thus, the fluid volume element absorbed less heat which caused the temperature difference to drop. Similar results were found by Chaudhary et al. [15], where the temperature difference of the experimental cases decreased with increasing FF concentration.

The experimental case with a solenoid electrical current of 0.80 A and an irradiation distance of 6 cm, produced the largest change in the temperature difference by changing the concentration. For the specified experimental case, by altering the concentration from 1.0 wt.% to 2.0 wt.%, the temperature difference dropped from 12.2 $\pm$ 0.1°C to 6.8 $\pm$ 0.1°C, respectively. This corresponds to a temperature difference decrease of 44.3%.

Magnetic field strength.
In Figure 5.20, the majority of the concentrations have decreasing temperature differences, during the exposure of an increased applied magnetic field strength. The increase in the solenoid electrical current from 0.40 A to 0.80 A, produced a minimal

temperature difference decrease for the different experimental cases. However, by changing the solenoid electrical current from 0.80 A to 1.26 A, an evident reduction in the average temperature differences were observed for the different experimental cases, except for the concentration of 0.5 wt.% with an irradiation distance of 8 cm. This was also observed in the vertical case, where an evident decrease in the average temperature difference occurred by increasing the solenoid electrical current from 0.80 A to 1.26 A. Similar results were found by Lajvardi et al. [34] and by Moghaddam [33], where increased magnetic field strengths produced lower average temperature differences.

When the applied magnetic field strength increased, the enhanced thermomagnetic pumping force increased the fluid velocity, which caused the fluid volume element to be exposed to the heating section for a shorter time. Thus, the fluid volume element absorbed less heat which caused the temperature difference to drop.

The largest change in the temperature difference by increasing the magnetic field strength was observed for the concentration of 1.0 wt.% with an irradiation distance of 6 cm. By enhancing the solenoid electrical current from 0.40 A to 1.26 A, the average temperature difference decreased from 12.4 ± 0.1°C to 7.1 ± 0.1°C respectively. This corresponds to a temperature difference drop of 42.7%.

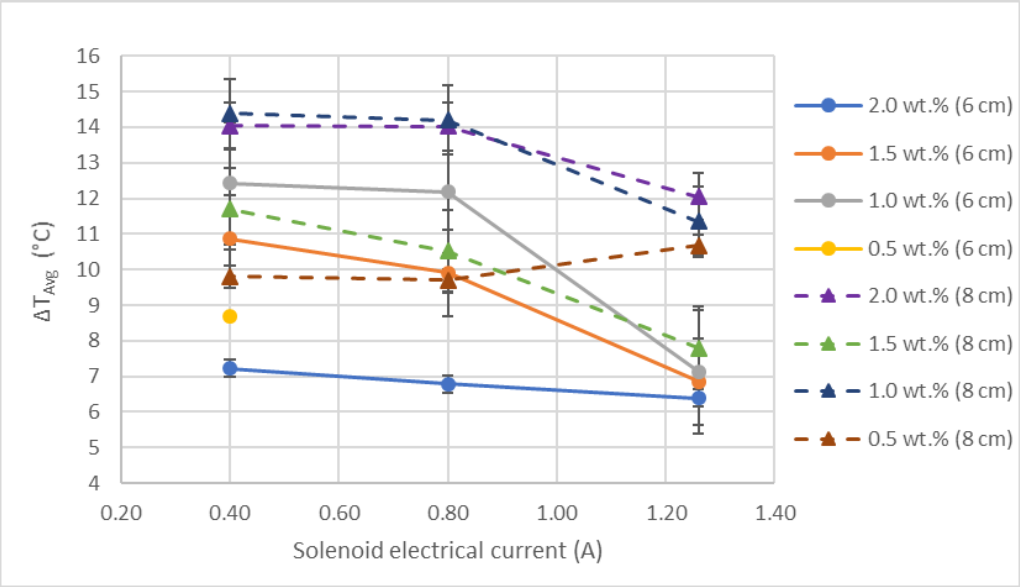

Figure 5.20: Average temperature differences as a function of the solenoid electrical current for different concentrations and irradiation distances.

The experimental case with a concentration of 0.5 wt.% and an irradiation distance of 8 cm has a positive slope, conversely to the other experimental cases. This could originate from evaporation. Furthermore, the concentration of 0.5 wt.% has the lowest magnetic susceptibility, and the fluid will be magnetized by an external magnetic field to a lesser extent compared with higher concentrations [52]. The exposure of an increased magnetic field strength increases both the fluid viscosity and the thermomagnetic force gradient [52][43]. Hence, the magnetic field has possibly increased the viscosity to such an extent, that the obstruction of flow caused the fluid volume element over the radiation zone to be irradiated for a longer time. The fluid volume element absorbs more heat which subsequently causes the temperature difference to increase.

The average temperature differences varied with the concentration, applied solenoid electrical current and applied heat flux. Of all the experimental cases with an irradiation distance of 8 cm, the concentration of 1.5 wt.% with a solenoid electrical current of 1.26 A produced the lowest temperature difference of 7.8 $\pm$ 0.1°C. Of all the experiments with an irradiation distance of 6 cm, the concentration of 2.0 wt.% with a solenoid electrical current of 1.26 A produced the lowest temperature difference of 6.4 $\pm$ 0.1°C.

Furthermore, lower average temperature differences were obtained for each of the experimental cases by increasing the irradiation distance from 8 cm to 6 cm.

It is interesting to note that the temperature differences for the horizontal case are almost the same for the vertical case.

5.4.3 Velocity analysis

The fluid velocity gives a good indication of the influence of thermomagnetic convection. Higher fluid velocities in the flow loop originate from enhanced thermomagnetic pumping force [33][52].

5.4.3.1 Procedure for obtaining the fluid velocity

The fluid velocities were calculated from Eq. (3.13), which was derived from the law of conservation of energy. For each case, the corresponding average temperature difference and the applied heat flux were used. For the specific heat capacity, the properties of water were used. Thus, the change in fluid properties was not accounted for, when particles were added to the solution. Additionally, several assumptions were made using this method. It was assumed constant pressure conditions ($\Delta H_{\Delta P=0} = q$), heat from the fluid is not lost to the surroundings, and chemical reactions within the fluid or between the fluid and the wall did not take place.

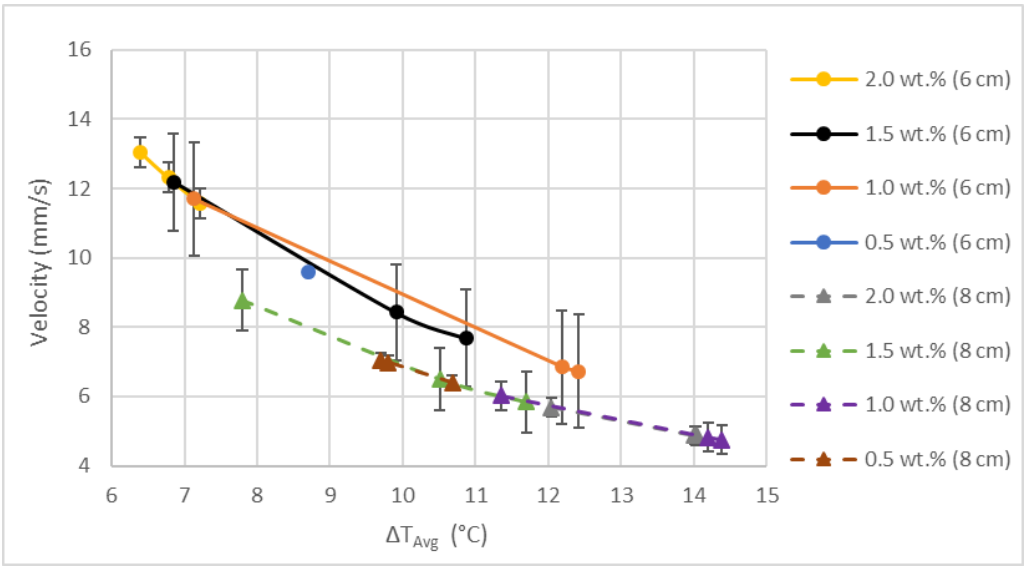

Figure 5.21: Fluid velocity as a function of the temperature difference for different solenoid electrical currents, concentrations and irradiation distances.

5.4.3.2 Investigation of the fluid velocities

Temperature difference.
In Figure 5.21, a linear relationship between the fluid velocity and the temperature difference was observed. This was also found in the vertical case, but for higher fluid velocities. The three value points on each line correspond to the results from the three solenoid electrical currents. Figure 5.21 exhibits that lower temperature differences correspond to higher fluid velocities. The experimental cases with an irradiation distance of 8 cm resulted in lower fluid velocities, compared to the same experimental cases with an irradiation distance of 6 cm. From studying the two experimental cases with a concentration of 1.5 wt.%, if the fluid velocity was to be kept constant, and the applied heat flux increased, the temperature difference has to increase. This is similar to the results found by Lajvardi et al. [34], where an increased applied heat flux corresponds to a higher fluid temperature if the fluid velocity was to be kept constant. This makes sense because the fluid volume element is exposed to an enhanced heat flux during the same period of time. Furthermore, by looking at the same two experimental cases. If the average temperature difference was to be kept constant, and the applied heat flux increased, the fluid velocity has to increase.

Particle concentration.
In Figure 5.22, by changing the fluid concentration from 0.5 wt.% to 1.0 wt.%, the fluid velocity decreased for all the experimental cases. As mentioned, the viscosity and the susceptibility increases with increasing concentration. The explanation for

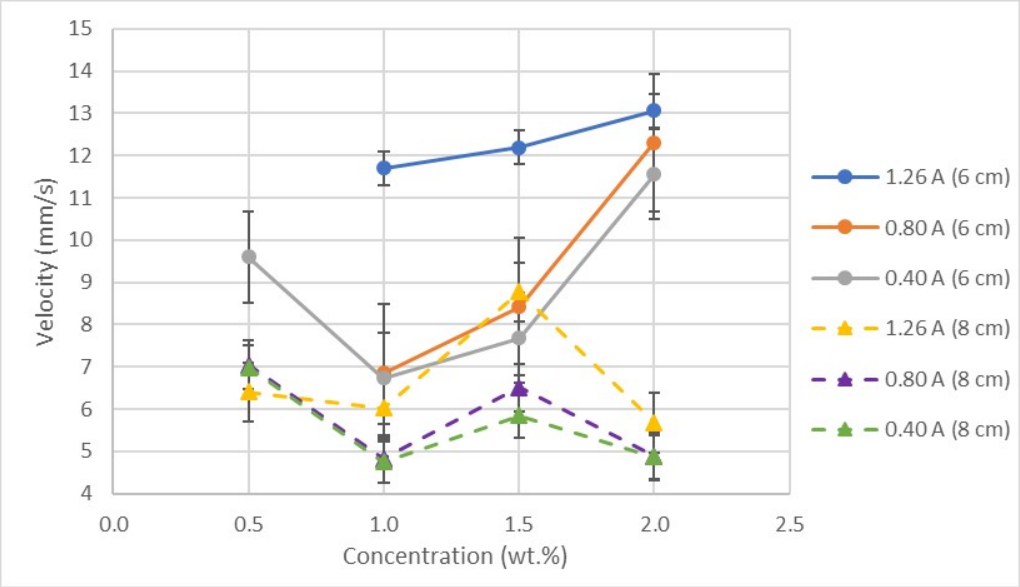

Figure 5.22: Velocity as a function of concentration for different solenoid electrical currents and irradiation distances.

these results originates most probably from the increase in the obstruction of flow from the fluid viscosity. At steady-state condition, the fluid velocity is determined from the balance between the driving and the resisting forces. Thus, for the specified experimental cases where the fluid velocity decreased by increasing the concentration, the increase in the thermomagnetic pumping force (driving force) was smaller than the fluid viscosity (resisting force) increase. Hence, the fluid velocity decreased due to the increased viscous drag throughout the whole circulation path.

The concentration change from 1.0 wt.% to 1.5 wt.% and subsequently to 2.0 wt.% for the experimental cases with an irradiation distance of 6 cm, caused the fluid velocity to increase regardless of the magnetic field strength. For low concentrations (wt.%<15.0), the addition of particles generates enhanced volumetric absorption efficiency [65]. More particles absorb the radiated light and transfer the absorbed heat to the fluid. Thus, the thermal energy increases, and the fluid is demagnetized to a greater extent. This results in a larger gradient between the magnetic and thermal energy, which induces a stronger thermomagnetic force gradient and a stronger thermomagnetic pumping force [52]. Thus, because a higher fluid velocity was observed, the thermomagnetic pumping force (driving force) increase was more significant than the fluid viscosity (resisting force) increase. This relationship was also found for the experimental cases with an irradiation distance of 8 cm, but only at the concentration change from 1.0 wt.% to 1.5 wt.%. Similar results were found by Chaudhary et al. [15], where the temperature differences decreased at higher fluid concentrations, which correspond to enhanced fluid velocities.

By increasing the concentration from 1.5 wt.% to 2.0 wt.% for the experimental cases with an irradiation distance of 8 cm, the fluid velocity decreased regardless of the magnetic field strength. Why the fluid velocity decreased can originate from the fluid magnetization. A lower applied heat flux reduces the thermal energy and demagnetizes the FF to a lesser extent. Hence, a lower applied heat flux results in a weaker thermomagnetic force gradient and subsequently, a lower thermomagnetic pumping force compared to a higher applied heat flux. Thus, by changing the concentration from 1.5 wt.% to 2.0 wt.%, the irradiation distance of 8 cm did not generate a high enough heat flux to obtain a sufficient fluid demagnetization. Furthermore, a large enough increase in the thermomagnetic pumping force was not produced. The increase in the thermomagnetic pumping force due to enhanced susceptibility was smaller than the fluid viscosity increase. Thus, the fluid velocities decreased due to the increased viscous drag throughout the whole circulation path. Nevertheless, if the applied heat flux is high enough, such as for the experimental cases with an irradiation distance of 6 cm, the tendency of an increasing fluid velocity due to an increasing concentration will occur.

In Figure 5.22, the experimental case with a solenoid electrical current of 0.80 A and an irradiation distance of 6 cm showed the largest increase in the fluid velocity by changing the concentration. From altering the concentration from 1.0 wt.% to 2.0 wt.% for the specified experimental case, the fluid velocity increased from 6.9 ± 1.2 mm/s to 12.3 ± 2.3 mm/s. This corresponds to a fluid velocity increase of 78.3%.

Magnetic field strength.
A fluid velocity increase due to a stronger applied magnetic field is a consistent relationship for all the experimental cases in Figure 5.23, except for the concentration of 0.5 wt.%. This relation was also found by Moghaddam [33], where the fluid velocity increased by increasing the magnetic field strength. Thus, the ability to control the fluid velocity by the magnetic field strength is indisputable. By increasing the magnetic field strength, a higher thermomagnetic force gradient and a stronger thermomagnetic pumping force are produced [52]. Thus, by keeping the concentration and the applied heat flux constant, an increase in the magnetic field strength induces generally a higher fluid velocity.

The most significant increase in fluid velocity by changing the magnetic field strength was observed for the experimental case with a concentration of 1.0 wt.% and an irradiation distance of 6 cm. By enhancing the solenoid electrical current from 0.40 A to 1.26 A, the fluid velocity increased from 6.7 ± 1.2 mm/s to 11.7 ± 2.1 mm/s, respectively. This corresponds to a fluid velocity increase of 74.6%. For the experimental cases with an irradiation distance of 8 cm, the largest increase in fluid velocity by changing the magnetic field strength was observed for the concentration of 1.5 wt.%. By enhancing the solenoid electrical current from 0.40 A to 1.26 A, the fluid velocity increased from 5.8 ± 0.9 mm/s to 8.8 ± 1.4 mm/s, respectively. This

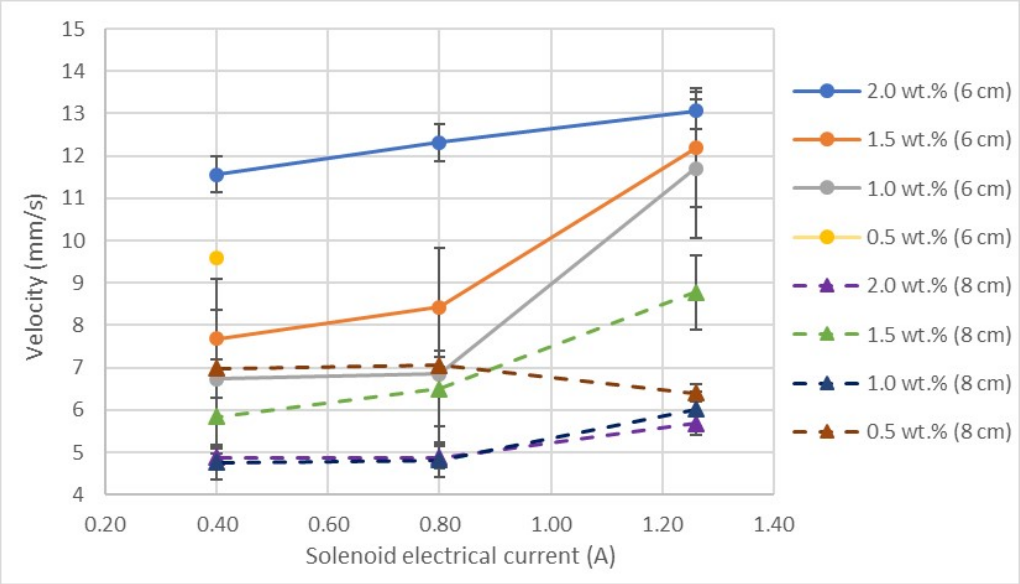

Figure 5.23: Velocity as a function of the solenoid electrical current for different concentrations and irradiation distances.

corresponds to a fluid velocity increase of 51.7%.

In Figure 5.23, a fluid velocity decrease for an increasingly magnetic field strength was only found for the experimental case with a concentration of 0.5 wt.% and an irradiation distance of 8 cm. The fluid velocity decrease was of a small extent and could originate from sources of error. Furthermore, the magnetic field has possibly increased the viscosity to such an extent, that the obstruction of flow throughout the whole circulation path caused the fluid velocity to decrease. Regardless, the tendency of a fluid velocity increase due to a stronger applied magnetic field for the other concentrations is indisputable.

The highest fluid velocity of 13.06 ± 2.39 mm/s was observed for the experimental case with an irradiation distance of 6 cm, concentration of 2.0 wt.% and a solenoid electrical current of 1.26 A. For the experimental cases with an irradiation distance of 8 cm, the highest fluid velocity of 8.77 ± 1.40 mm/s was found at the concentration of 1.5 wt.% and a solenoid electrical current of 1.26 A.

Heat flux.
Figures 5.24 - 5.27 demonstrates that the fluid velocity increases at increasing applied heat flux, regardless of the magnetic field strength. As mentioned in section 5.4, the irradiation distances of 8 cm and 6 cm corresponds to the heat fluxes of 5696 W/m^2 and 6961 W/m^2, respectively. The FF is demagnetized at the heating section, due to temperature increase. A larger gradient between the magnetic and thermal energy induces a stronger thermomagnetic force gradient. By increasing

the applied heat flux, increases the thermal energy, which causes the fluid to be demagnetized to a larger extent. The increased demagnetization of the FF results in a higher thermomagnetic force gradient and an increased thermomagnetic pumping force [52]. Hence, a stronger applied heat flux produces an increased fluid velocity, which subsequently induces a better cooling performance. This illustrates the self-regulating feature of a thermomagnetic driven flow system, which was also found by Lian et al. [39] and Moghaddam [33]. If the object that is cooled increases in temperature, the radiating heat flux from the object increases, and a higher fluid velocity in the flow loop will be induced, which cause enhanced cooling performance. This indicates that the external heat load automatically controls the operation of the cooling device. This self-regulating feature can replace the need for sensors in applications where the fluid velocity must be controlled to obtain sufficient cooling.

Another observation in Figures 5.24, 5.25 and 5.26 was that the slope of the velocity line became steeper at higher applied magnetic field strengths. The influence of the magnetic field on the fluid velocity increased when the applied heating flux increased. It appears that at a lower applied heat flux (5695 W/m^2), by increasing the magnetic field strength, the thermal energy is not sufficient to demagnetize the FF to the same extent as at a higher applied heat flux (6961 W/m^2) [52]. Thus, at an increased heat flux, by enhancing the magnetic field strength, the fluid velocity will increase to a greater extent. Similar results were found by Moghaddam [33], where the slope of the velocity line became steeper at higher magnetic field strengths.

The Reynolds number for all the experimental cases in Figures 5.24 - 5.27 were within the laminar flow region ($Re < 2100$) [40]. This was expected and assumed in the analytically fluid velocity calculations.

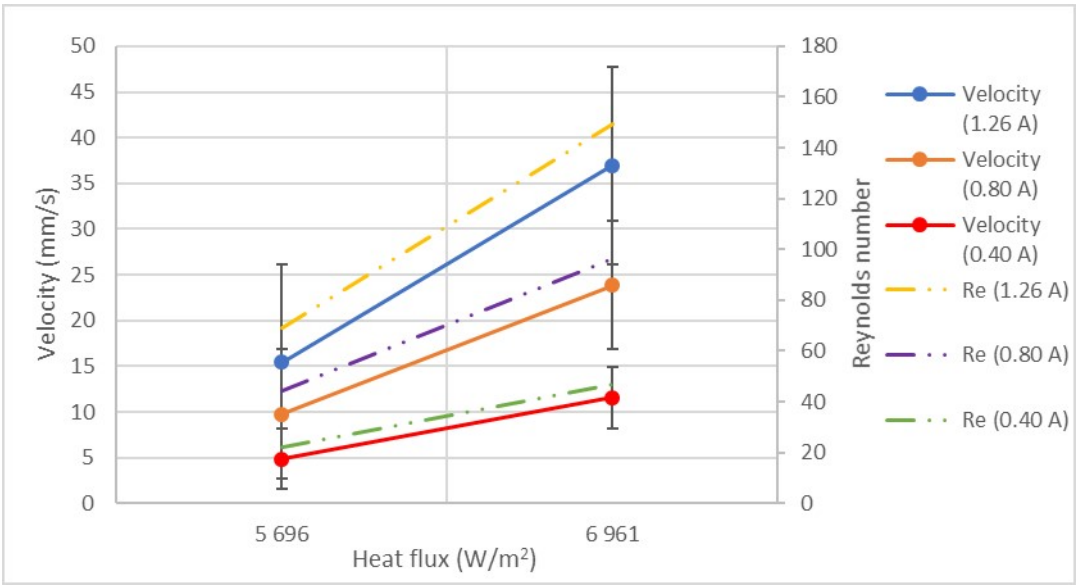

Figure 5.24: Velocities of 2.0 wt.% of Fe_2O_3 as a function of heat flux, at different solenoid electrical currents.

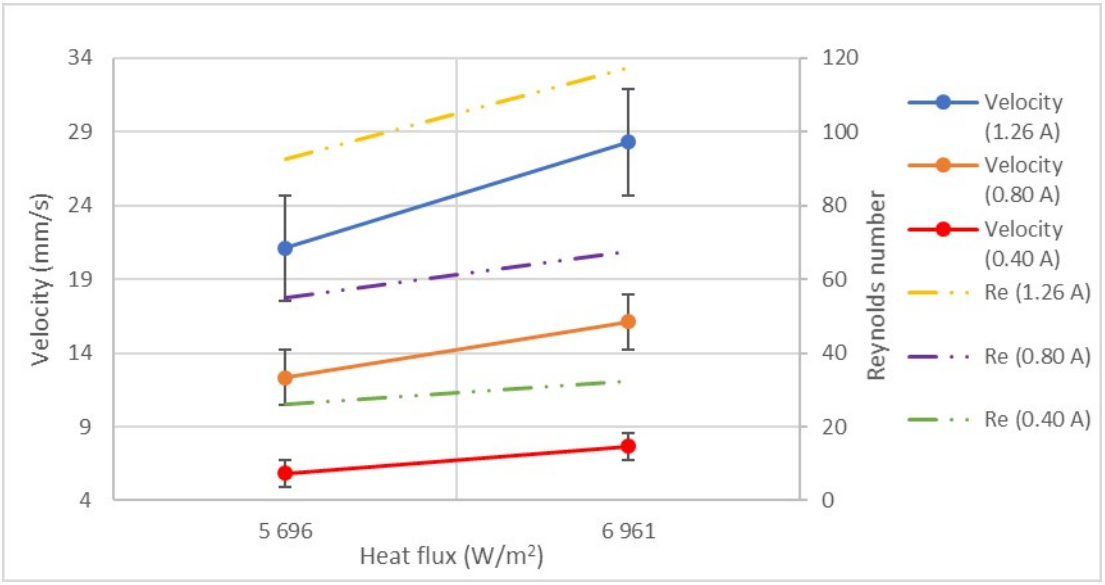

Figure 5.25: Velocities of 1.5 wt.% of Fe_2O_3 as a function of heat flux, at different solenoid electrical currents.

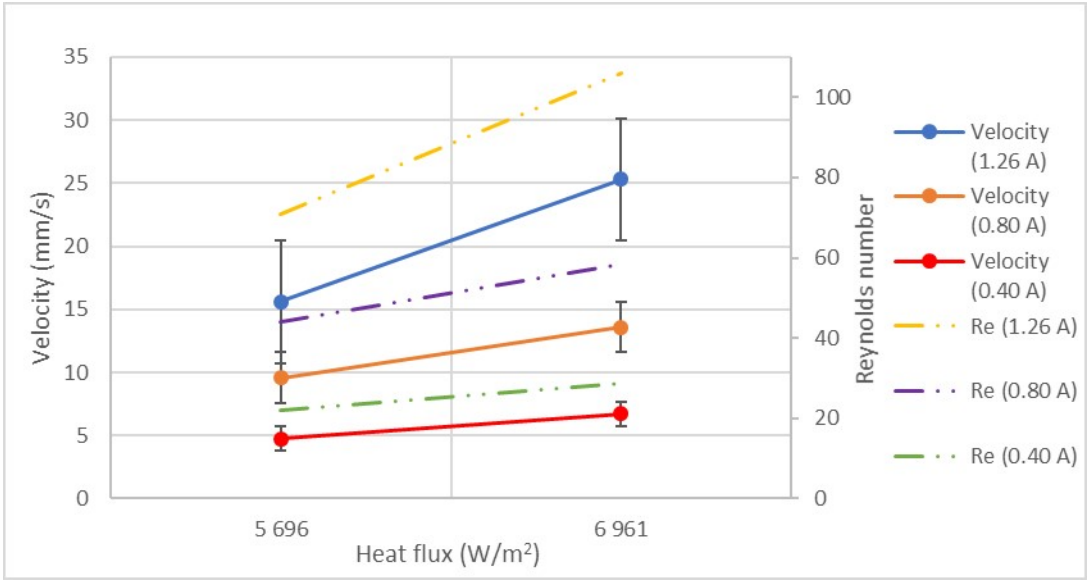

Figure 5.26: Velocities of 1.0 wt.% of Fe_2O_3 as a function of heat flux, at different solenoid electrical currents.

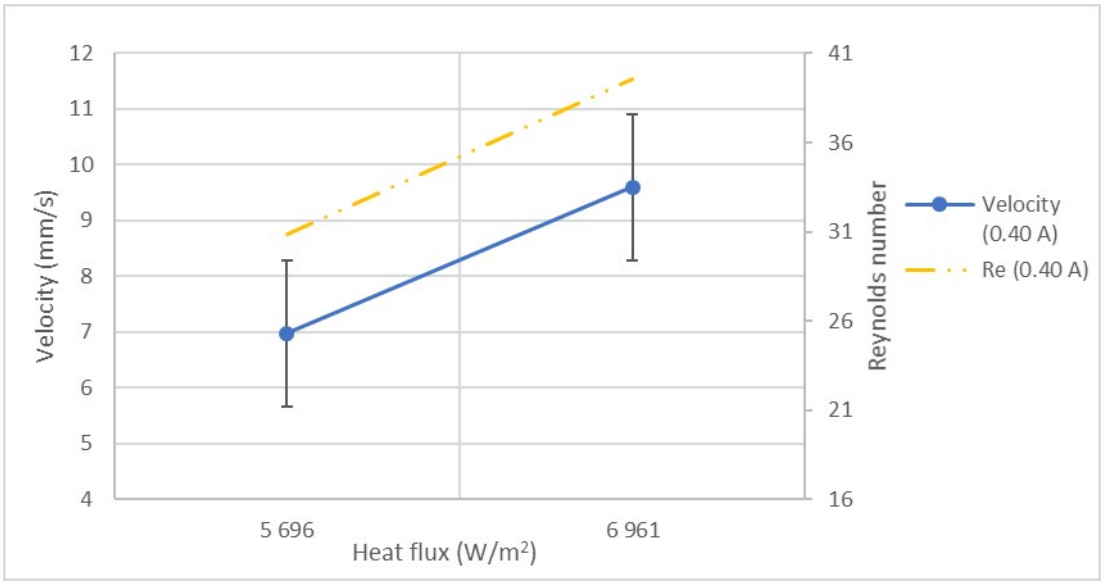

Figure 5.27: Velocities of 0.5 wt.% of Fe_2O_3 as a function of heat flux, at different solenoid electrical currents.

5.5 Comparison of the fluid velocities

The fluid velocity vs magnetic field strength, for the vertical and horizontal experimental cases with a concentration of 2.0 wt.%, is visualized in Figure 5.28. The fluid velocities from the vertical case were higher compared with the fluid velocities from the horizontal case, regardless of the magnetic field strength. It must be noted that the applied heat flux from the thermal bath used in the vertical case is unknown. However, the contact area between the thermal bath and glass tube was significantly larger than the contact area between the irradiating light and the glass tube. Perhaps, the thermal bath applied a higher heat flux to the system, which increased the fluid velocity. Nevertheless, an increased magnetic field induced a higher fluid velocity for all the experimental cases.

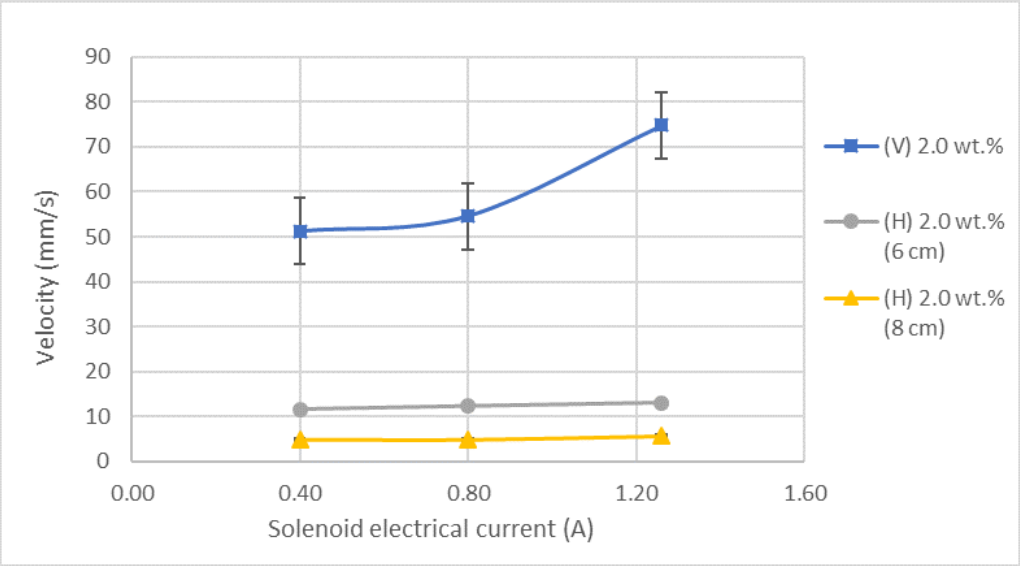

Figure 5.28: Fluid velocity vs magnetic field strength, for the vertical and horizontal experimental cases with a concentration of 2.0 wt.%. "(V)" is the experimental case with the apparatus in the vertical orientation, and "(H)" is the experimental cases with the apparatus in the horizontal orientation.

5.6 Particle size distribution

The extent to which the average particle size of the ferrofluid was affected by the experiments was investigated using SLS. SLS was done before and after an experiment. With the apparatus in a horizontal orientation, concentrations of 1.0 wt.% and 2.0 wt.%, a solenoid electrical current of 1.26 A and an irradiation distance of 8 cm, were used as the experimental cases.

In Figures 5.29 and 5.30, a shift towards a higher particle size distribution after the

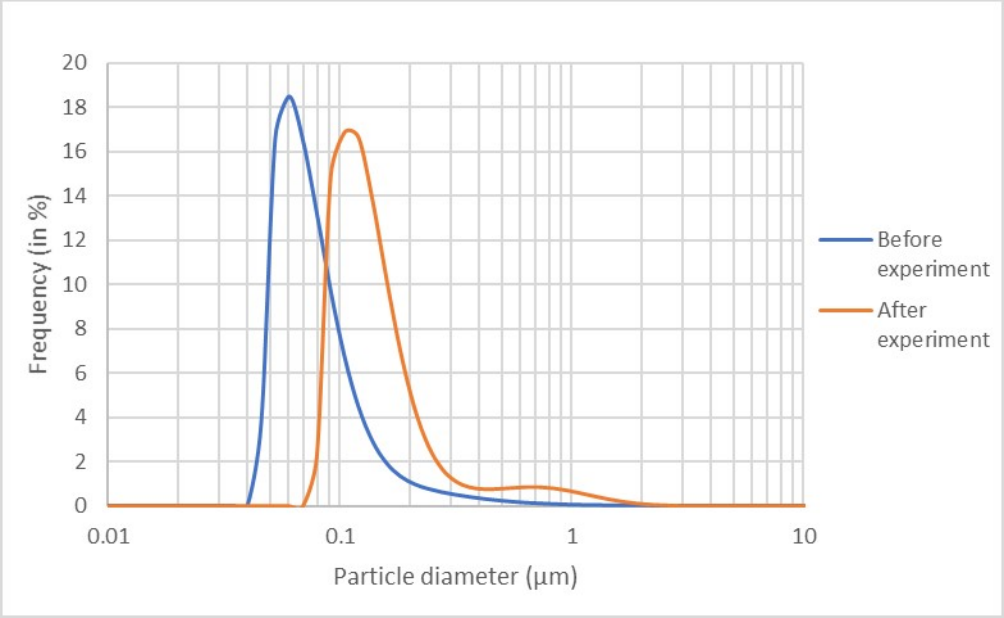

Figure 5.29: Number frequency of the particle size distribution of 1.0 wt.% of Fe_2O_3, obtained from SLS.

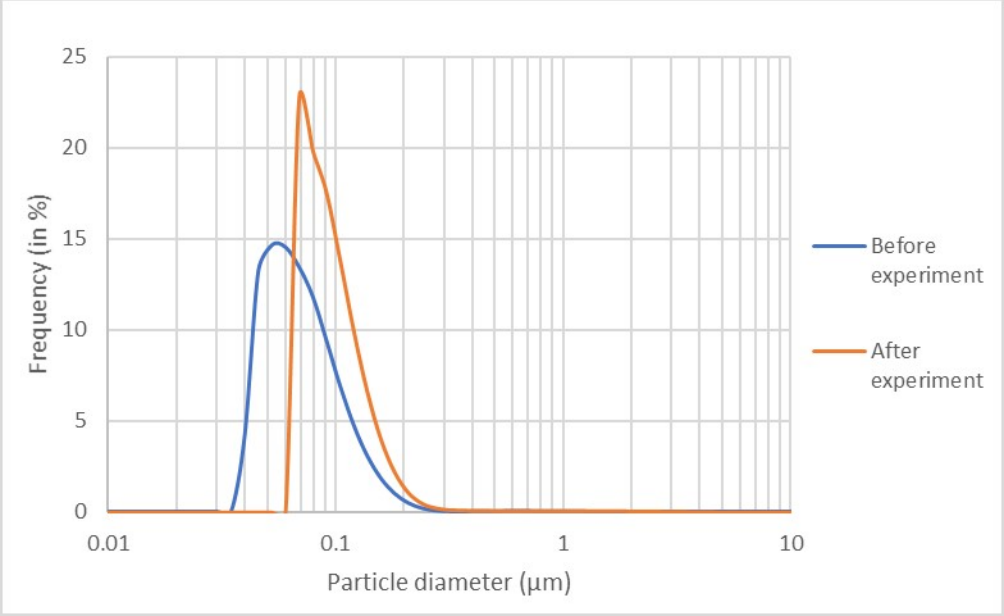

Figure 5.30: Number frequency of the particle size distribution of 2.0 wt.% of Fe_2O_3, obtained from SLS.

experiments were seen. The calculated average particle diameter of the experimental cases with a concentration of 1.0 wt.% and 2.0 wt.% before an experiment was 0.097 μm and 0.091 μm, respectively. The calculated average particle diameter of the former and latter experimental cases after an experiment was 0.18 μm and 0.12 μm, respectively.

The shift towards a higher particle size distribution after an experiment demonstrates that particle agglomeration took place. From the stability investigation in section 3.3.3, particle agglomeration would take place regardless of the conducted experiments. This could cause some particles to drop out of the suspension over time and deposit at the bottom. Although the particle size distribution increased, no particle sedimentation in the tubes was observed. The obtained fluid velocity during experiments supplied energy to the suspension and hindered the particles from depositing.

As the fluid concentration increases, the assumption that the particles do not aggregate becomes less valid. However, in Figures 5.29 and 5.30, by increasing the concentration from 1.0 wt.% to 2.0 wt.%, the shift towards a higher particle size distribution was almost the same. Thus, the extent of particle aggregation in the former and latter experimental cases was close to similar, and little affected by the concentration enhancement.

5.7 Power consumption

An accurate analysis of the heat loss in the flow loop is required to estimate the efficiency. This was beyond the scope of this thesis. However, the power consumed by the DASC and the power consumed in the solenoid are need in the heat loss analysis, and is therefore visualized in Table 5.3. This can be used in further research.

Solenoid		**Halogen lamp**	
Current (I)	**Power (W)**	**Heat flux (W/m^2)**	**Power (W)**
1.26	7.56	6961	2.78
0.80	3.04	5695	2.28
0.40	0.76		

Table 5.3: Power consumed in the solenoid and power consumed by the DASC.

Chapter 6

Conclusion

In this thesis, a differentially heated flow loop exposed to a magnetic field, with an operating FF (Fe_2O_3-water) under steady-state laminar flow conditions, driven by thermomagnetic convection, was investigated experimentally. Both vertical and horizontal orientation of the flow loop was studied. The flow loop is an energy transport device which does not need a mechanical pump, and has great potential in multiple thermal management applications, especially in remote and hazardous areas. The objective was to investigate how different particle concentrations, magnetic field strengths and applied heat fluxes affected the thermomagnetic convection effect, which can be utilized in future thermal management research.

In the study with the apparatus in a vertical orientation, both natural and thermomagnetic convection were present. For the experimental cases with concentrations of 0.5 wt.% and 1.0 wt.%, the magnetic field strengths affected the influence of thermomagnetic convection to a small extent. However, for the experimental cases with concentrations of 1.5 wt.% and 2.0 wt.%, a significant influence of thermomagnetic convection was observed. The results showed that a magnetic field could control the temperature distribution in the fluid and the fluid velocity. The fluid velocity increased in the flow loop by increasing the magnetic field strength. The effect of the magnetic field on the temperature distribution and fluid velocity was controlled by particle concentration.

At a constant applied heat flux, the lowest measured average temperature difference of 7.5 $\pm$ 0.1 °C was observed for the experimental case with a concentration of 1.5 wt.% and a solenoid electrical current of 1.26 A. This temperature difference corresponded to the highest estimated fluid velocity of 90.9 mm/s. If only natural convection had been present at this temperature difference, the fluid velocity had been equal to 11.7 $\pm$ 2.2 mm/s. Thus, for the specified experimental case, the fluid velocity from thermomagnetic convection increase by 676.9 $\pm$ 1.3 % compared

to the fluid velocity from the natural convection. For the experimental case with a concentration of 2.0 wt.%, by applying a magnetic field with solenoid electrical currents of 1.26 A, 0.80 A and 0.40 A, the fluid velocity from thermomagnetic convection increased by 398.7 ± 0.7 %, 173.0 ± 0.4 % and 143.8 ± 0.3 % respectively, compared to the fluid velocity from the natural convection.

In the study with the apparatus in a horizontal orientation, only thermomagnetic convection was present. The heating source was switched to a halogen lamp, and the apparatus operated as a DASC. The results demonstrated that the magnetic field could control the temperature distribution in the fluid and the fluid velocity. The fluid velocity increased in the flow loop by increasing the magnetic field intensity. The effect of the magnetic field on the temperature distribution and fluid velocity was controlled by particle concentration and the applied heat flux. In addition, the flow loop exhibited a self-regulating feature. By increasing the applied heat flux, the fluid velocity increased for all the experimental cases. This indicates that the external heat load automatically controls the operation of the cooling device. This self-regulating feature can replace the need for sensors in applications where the fluid velocity must be controlled to obtain sufficient cooling [33].

For the experimental cases with a heat flux of 5695 W/m^2, the highest fluid velocity of 8.8 $\pm$ 1.4 mm/s was found for the concentration of 1.5 wt.% and a solenoid electrical current of 1.26 A. Furthermore, for the experimental cases with a heat flux of 6961 W/m^2, the highest fluid velocity of 13.1 $\pm$ 2.4 mm/s was found for the concentration of 2.0 wt.% and a solenoid electrical current of 1.26 A. Thus, the optimal concentration to obtain the highest fluid velocity changed when the applied heat flux was altered. Nevertheless, the results show that an external magnetic field can control the fluid velocity and the temperature distribution of the fluid in a DASC.

The ability to control the fluid temperature distribution and fluid velocity observed from the results demonstrate that thermomagnetic convection is very promising for thermal management systems.

Chapter 7

Future work

Suggestions for future work is listed below:

- Further investigation of the stability of the FF Fe_2O_3-water.
- Study the possibility of using permanent magnets in these systems instead of a solenoid, and how to utilize the inappropriate magnetic field configurations of permanent magnets, to achieve just as good performance as by using a solenoid. This will avoid the need of additional power consumption from the solenoid.
- Research on using thermomagnetic convection for cooling of electromagnetic devices such as the end windings of electric machines. In such machines, the temperature and magnetic field gradient are already present, and will generate a thermomagnetic pumping force which circulates the cooling fluid (FF).
- Explore the range of applicability for thermomagnetic convection.
- Investigate the influence of the magnetoviscous effect on the thermomagnetic convection.

Bibliography

[1] *"Averaging, Errors and Uncertainty"*. (Accessed: 2020-03-14). [Online]. URL: https://avntraining.hartrao.ac.za/images/Error_Analysis.pdf.

[2] Mustafa Alsaady, Rong Fu, Bo Li, Rabah Boukhanouf, and Yuying Yan. "Thermophysical properties and thermo-magnetic convection of ferrofluid". *Applied thermal engineering* 88 (Sept. 2015), pp. 14–21.

[3] Mustafa Alsaady, Rong Fu, Yuying Yan, Zeyu Liu, Shenyi Wu, and Rabah Boukhanouf. "An Experimental Investigation on the Effect of Ferrofluids on the Efficiency of Novel Parabolic Trough Solar Collector Under Laminar Flow Conditions". *Heat Transfer Engineering* 40.9-10 (2019), pp. 753–761.

[4] John D. Anderson JR. *Computational Fluid Dynamics*. McGraw-Hill, 1995.

[5] S. A. Angayarkanni and John Philip. "Review on thermal properties of nanofluids: Recent developments". *Advances in colloid and interface science* 225 (Nov. 2015), pp. 146–176.

[6] Amin Asadi, Farzad Pourfattah, Imre Miklós Szilágyi, Masoud Afrand, Gaweł Żyła, Ho Seon Ahn, Somchai Wongwises, Hoang Minh Nguyen, Ahmad Arabkoohsar, and Omid Mahian. "Effect of sonication characteristics on stability, thermophysical properties, and heat transfer of nanofluids: A comprehensive review". *Ultrasonics sonochemistry* 58 (Nov. 2019), p. 104701. ISSN: 1350-4177.

[7] Eskil Aursand, Magnus Aa. Gjennestad, Karl Yngve Lervag, and Halvor Lund. "A multi-phase ferrofluid flow model with equation of state for thermomagnetic pumping and heat transfer". *Journal of Magnetism and Magnetic Materials* 402 (Mar. 2016), pp. 8–19.

[8] Eskil Aursand, Magnus Aa. Gjennestad, Karl Yngve Lervag, and Halvor Lund. "Potential of enhancing a natural convection loop with a thermomagnetically pumped ferrofluid". *Journal of Magnetism and Magnetic Materials* 417 (Nov. 2016), pp. 148–159.

[9] Mehdi Bahiraei and Morteza Hangi. "Flow and heat transfer characteristics of magnetic nanofluids: A review". *Journal of Magnetism and Magnetic Materials* 374 (2015), pp. 125–138. ISSN: 0304-8853.

[10] Boris V. Balakin and Kirill V. Kutsenko. "Magnetic enhancement of photothermal heating in ferrofluids". *Journal of Physics: Conference Series* 1133 (Nov. 2018), p. 012011.

[11] Boris V. Balakin, Oleg V. Zhdaneev, Anna Kosinska, and Kiri V. Kutsenko. "Direct absorption solar collector with magnetic nanofluid: CFD model and parametric analysis". *Renewable Energy* 136 (June 2019), pp. 23–32.

[12] Sumanta Banerjee, Achintya Mukhopadhyay, Swarnendu Sen, and Ranjan Ganguly. "Thermomagnetic Convection in Square and Shallow Enclosures for Electronics Cooling". *Numerical Heat Transfer part A-applications* 55.10 (2009), pp. 931–951.

[13] Tomasz Bednarz, John C. Patterson, Chengwang Lei, and Hiroyuki Ozoe. "Enhancing natural convection in a cube using a strong magnetic field - Experimental heat transfer rate measurements and flow visualization". *International Communications in Heat and Mass Transfer* 36.8 (Oct. 2009), pp. 781–786.

[14] Lee Blaney. "Magnetite (Fe3O4) Properties, synthesis and applications". *The Lehigh Review* 15 (Jan. 2007), pp. 33–81.

[15] V Chaudhary, Z Wang, A Ray, I Sridhar, and R. V Ramanujan. "Self pumping magnetic cooling". *Journal of Physics D: Applied Physics* 50.3 (Dec. 2016), 03LT03.

[16] P. R. N. Childs, J. R. Greenwood, and C. A. Long. "Review of temperature measurement". *Review of Scientific Instruments* 71.8 (2000), pp. 2959–2978.

[17] S U.S. Choi and Jeffrey A. Eastman. "Enhancing thermal conductivity of fluids with nanoparticles" (Oct. 1995).

[18] APW Company. *"Finished Standard Stock Electromagnet Coil - 6VDC"*. (Accessed: 2020-04-20). [Online]. URL: `https://apwelectromagnets.com/fc-5818.html#product-details-tab-specification`.

[19] Thermal Corporation. (Accessed: 2020-03-12). [Online]. URL: `https://i0.wp.com/www.thermalcorporation.com/wp-content/uploads/2019/02/thermocouplejunctions.jpg?ssl=1`.

[20] Prasun Dutta, Sumit Kumar Saha, Nityananda Nandi, and Nairit Pal. "Numerical study on flow separation in 90 degrees pipe bend under high Reynolds number by k$-\varepsilon$ modelling". *Engineering Science and Technology, an International Journal* 19.2 (2016), pp. 904–910. ISSN: 2215-0986.

[21] Royal Academy of Engineering. *"Solenoid valve – electromagnetism"*. (Accessed: 2020-05-19). [Online]. URL: `https://www.raeng.org.uk/publications/other/10-solenoid-valve_final`.

[22] Thomas A. Franklin. *Ferrofluid Flow Phenomena*. PhD diss. 2003.

[23] Fabio Galbusera and Frank Niemeyer. "Chapter 14 - Mathematical and Finite Element Modeling". *Biomechanics of the Spine*. Ed. by Fabio Galbusera and Hans-Joachim Wilke. Academic Press, 2018, pp. 239–255. ISBN: 978-0-12-812851-0.

[24] W. F. Hall and S. N. Busenberg. "Viscosity of Magnetic Suspensions". *The Journal of Chemical Physics* 51.1 (1969), pp. 137–144.

[25] VWR Advanced hotplates. *"Hotplate, ceramic"*. (Accessed: 2020-03-12). [Online]. URL: `https://no.vwr.com/store/product/en/3216743/varmeplater-advanced-serien?languageChanged=en`.

[26] Christopher P. Hunt, Bruce M. Moskowitz, and Subir K. Banerjee. "Magnetic Properties of Rocks and Minerals" (1995).

[27] Yu-Jin Hwang, Jae-Keun Lee, Jong-Ku Lee, Young Jeong, Seong-ir Cheong, Young-Chull Ahn, and Soo Kim. "Production and Dispersion Stability of Nanoparticles in Nanofluids". *Powder Technology - Powder Technol* 186 (Aug. 2008), pp. 145–153.

[28] Shenzhen Linshang Technology Co. Ltd. IR. *Power meter user manual*. (Accessed: 2020-03-12). [Online]. URL: `http://www.lsmeter.com/product/LS122new.html`.

[29] David Jiles. *Introduction to magnetism and magnetic materials*. Chapman and Hall, 1991.

[30] Raj K. and Moskowitz R. "Ferrofluid-cooled electromagnetic device and improved cooling method". *U.S. Patent No. 5,462,685* (1995).

[31] Sadik Kakac and Anchasa Pramuanjaroenkij. "Review of convective heat transfer enhancement with nanofluids". *International Journal of Heat and Mass Transfer* 52.13-14 (June 2009), pp. 3187–3196.

[32] P. N. Kaloni and A. Mahajan. "Stability and uniqueness of ferrofluids". *International Journal of Engineering Science* 48.11, SI (Nov. 2010), pp. 1350–1356.

[33] Giti Karimi-Moghaddam. "Application of Thermomagnetic Convection in Thermal Management of Electronic Systems". PhD diss. PhD thesis. North Carolina State University, 2014.

[34] Maryamalsadat Lajvardi, Jafar Moghimi-Rad, Iraj Hadi, Anwar Gavili, Taghi D. Isfahani, Fatemeh Zabihi, and Jamshid Sabbaghzadeh. "Experimental investigation for enhanced ferrofluid heat transfer under magnetic field effect". *Journal of Magnetism and Magnetic Materials* 322.21 (2010), pp. 3508–3513. ISSN: 0304-8853.

[35] Calvin H. Li and G. P. Peterson. "Experimental Studies of Natural Convection Heat Transfer of Al2O3/DI Water Nanoparticle Suspensions (Nanofluids)". *Advances in Mechanical Engineering* 2.0 (2015), pp. 742739–742739. ISSN: 1687-8132.

[36] Qiang Li, Yimin Xuan, and Jian Wang. "Experimental investigations on transport properties of magnetic fluids". *Experimental Thermal and Fluid Science* 30.2 (2005), pp. 109–116. ISSN: 0894-1777.

[37] Yanjiao Li, Jing'en Zhou, Simon Tung, Eric Schneider, and Shengqi Xi. "A review on development of nanofluid preparation and characterization". *Power Technology* 196.2 (Dec. 2009), pp. 89–101.

[38] W. Lian, Y. Xuan, and Q. Li. "Characterization of miniature automatic energy transport devices based on the thermomagnetic effect". *Energy Conversion and Management* 50.1 (Jan. 2009), pp. 35–42.

[39] Wenlei Lian, Yimin Xuan, and Qiang Li. "Design method of automatic energy transport devices based on the thermomagnetic effect of magnetic fluids". *International Journal of Heat and Mass Transfer* 52.23 (2009), pp. 5451–5458. ISSN: 0017-9310.

[40] Warren L. McCabe, Julian C. Smith, and Peter Harriot. *Unit operations of chemical engineering*. McGraw-Hill Education, 2005.

[41] Siyuan Mei, Cong Qi, Maoni Liu, Fan Fan, and Lin Liang. "Effects of paralleled magnetic field on thermo-hydraulic performances of Fe3O4-water nanofluids in a circular tube". *International Journal of Heat and Mass Transfer* 134 (May 2019), pp. 707–721.

[42] M. Misale, F. Devia, and P. Garibaldi. "Experiments with Al2O3 nanofluid in a single-phase natural circulation mini-loop: Preliminary results". *Applied Thermal Engineering* 40 (2012), pp. 64–70. ISSN: 1359-4311.

[43] Michael Murray. "Emergent Viscous Phenomena in Ferrofluids" (Dec. 2008). (Accessed: 2020-01-07). [Online]. URL: `http://guava.physics.uiuc.edu/~nigel/courses/569/Essays_Fall2008/files/murray.pdf`.

[44] Innocent Nkurikiyimfura and Antoine de Padoue Shyikira. "Photothermal characteristics of magnetic nanofluids for solar thermal applications". *International Journal of Engineering Research & Technology* 4 (Jan. 2015), pp. 765–770.

[45] Innocent Nkurikiyimfura, Yanmin Wanga, and Zhidong Pan. "Heat transfer enhancement by magnetic nanofluids—A review" (Feb. 2013).

[46] Stefan Odenbach. *Ferrofluids: Magnetically Controllable Fluids and Their Applications*. Eng. Vol. 594. Lecture Notes in Physics, Berlin, Heidelberg: Springer Berlin Heidelberg, 2002.

[47] OMEGA. *"Thermocouple types"*. (Accessed: 2020-03-12). [Online]. URL: `https://www.omega.com/en-us/resources/thermocouple-types`.

[48] Omega. *"How to choose a Thermocouple"*. (Accessed: 2020-04-20). [Online]. URL: `https://www.omega.com/en-us/resources/selecting-a-thermocouple`.

[49] Souvik Pal, Amitava Datta, Swarnendu Sen, Achintya Mukhopdhyay, Kallol Bandopadhyay, and Ranjan Ganguly. "Characterization of a ferrofluid-based thermomagnetic pump for microfluidic applications". *Journal of Magnetism and Magnetic Materials* 323.21 (Nov. 2011), pp. 2701–2709.

[50] John Philip, P. D. Shima, and Baldev Raj. "Evidence for enhanced thermal conduction through percolating structures in nanofluids". *Nanotechnology* 19.30 (July 2008).

[51] M. Raja, R. Vijayan, P. Dineshkumar, and M. Venkatesan. "Review on nanofluids characterization, heat transfer characteristics and applications". *Renewable & Sustainable Energy Reviews* 64 (Oct. 2016), pp. 163–173.

[52] R.E. Rosenzweig. *Ferrohydrodynamics*. Cambridge University Press, 1997.
[53] Ebtisam Saeed, Manuel M. Piñeiro, Carolina Hermida-Merino, and María José Pastoriza-Gallego. "Determination of Transport Properties of Glycol-Based NanoFluids Derived from Surface Functionalized Graphene". *Nanomaterials* 9.2 (2019), p. 252. ISSN: 2079-4991.
[54] Jahar Sarkar, Pradyumna Ghosh, and Arjumand Adil. "A review on hybrid nanofluids: Recent research, development and applications". *Renewable & Sustainable Energy Reviews* 43 (Mar. 2015), pp. 164–177.
[55] Ehsan Shojaeizadeh, Farzad Veysi, Koorosh Goudarzi, and Mostafa Feyzi. "Magnetoviscous effect investigation of water based Mn-Zn Fe2O4 magnetic nanofluid under the influence of magnetic field: An experimental study". *Journal of Magnetism and Magnetic Materials* 477 (May 2019), pp. 292–306.
[56] Sigma-Aldrich. *"Iron(III) oxide nanopowder, < 50nm particle size (BET)"*. (Accessed: 2020-03-12). [Online]. URL: https://www.sigmaaldrich.com/catalog/product/aldrich/544884?lang=en&region=NO.
[57] R. Skomski. "Nanomagnetics". *Journal of Physics-Condensed Matter* 15.20 (May 2003), R841–R896.
[58] Jayanti Sreenivas. "Bends, Flow and Pressure Drop" (Mar. 2011). DOI: 10.1615/AtoZ.b.bends_flow_and_pressure_drop_in.
[59] STAR-CCM+. *STAR-CCM+ User guide*.
[60] Bin Sun, Wei Lei, and Di Yang. "Flow and convective heat transfer characteristics of Fe2O3–water nanofluids inside copper tubes". *International Communications in Heat and Mass Transfer* 64 (2015), pp. 21–28. ISSN: 0735-1933.
[61] Robert A. Taylor, Patrick E. Phelan, Todd P. Otanicar, Ronald Adrian, and Ravi Prasher. "Nanofluid optical property characterization: towards efficient direct absorption solar collectors". *Nanoscale Research Letters* (2011).
[62] Robert Taylor, Sylvain Coulombe, Todd Otanicar, Patrick Phelan, Andrey Gunawan, Wei Lv, Gary Rosengarten, Ravi Prasher, and Himanshu Tyagi. "Small particles, big impacts: A review of the diverse applications of nanofluids". *Journal of Applied Physics* 113.1 (Jan. 2013).
[63] Halvard Thon. *Photothermal Boiling and Characterization of Nanofluids*. Master of Science in Process Technology. 2019.
[64] I. Torres-Diaz and C. Rinaldi. "Recent progress in ferrofluids research: novel applications of magnetically controllable and tunable fluids". *Soft Matter* 10.43 (2014), pp. 8584–8602.
[65] Edda Torsdottir Ulset. *Utilizing Solar Vapour Energy by Use of Nanofluids in a Direct Absorption Solar Collector*. Master's program in Energy with Specialization in Energy Technology. 2018.
[66] Werner Weitschies, Katharina Philipp, R. Kötitz, E. Romanus, and Peter Weber. "Mobility of Magnetic Peg-Nanoparticles in Blood, Liver and Spleen of Rats" (Dec. 2019).

[67] W. Wrobel, E. Fornalik-Wajs, and J. S. Szmyd. "Experimental and numerical analysis of thermo-magnetic convection in a vertical annular enclosure". *International Journal of Heat and Fluid Flow* 31.6, SI (Dec. 2010), pp. 1019–1031.

[68] Yimin Xuan and Wenlei Lian. "Electronic cooling using an automatic energy transport device based on thermomagnetic effect". *Applied Thermal Engineering* 31.8-9 (June 2011), pp. 1487–1494. ISSN: 1359-4311.

[69] Yimin Xuan and Wenlei Lian. "Electronic cooling using an automatic energy transport device based on thermomagnetic effect". *Applied Thermal Engineering* 31.8-9 (June 2011), pp. 1487–1494.

[70] Dae-Hwang Yoo, kwangjoon Hong, Tae Eun Hong, Jeffrey Eastman, and Imjeong Ho-Soon Yang. "Thermal conductivity of Al2O3/water nanofluids". *Journal of The Korean Physical Society - J Korean PHYS SOC* 51 (Oct. 2007).

[71] Wei Yu and Huaqing Xie. "A Review on Nanofluids: Preparation, Stability Mechanisms, and Applications". *Journal of Nanomaterials* (2012).

Appendices

Appendix A

Additional equations

A.1 Propagation of uncertainty of independent variables

The standard deviation of a function $f(x, y, z, ..., i)$ of independent variables $x, y, z, ..., i$ is given by [1]:

$$S_f = \sqrt{\left(\frac{\delta f}{\delta x} S_x\right)^2 + \left(\frac{\delta f}{\delta y} S_y\right)^2 + \left(\frac{\delta f}{\delta z} S_z\right)^2 + ... + \left(\frac{\delta f}{\delta i} S_i\right)^2}, \tag{A.1}$$

where S_f is the standard deviation of the function f and $S_x, S_y, S_z, ..., S_i$ are the standard deviation of the independent variables.

A.2 Theoretical magnetic field strength from solenoid

The magnetic field strength H of a solenoid is given as [21]:

$$H = \frac{NI}{L}, \tag{A.2}$$

where N, I and L are the number of turns of wire, the applied electrical current (A) and the length of the solenoid (m), respectively.

Appendix B

Stability study

B.1 After sonification

Pictures of the samples straight after sonification.

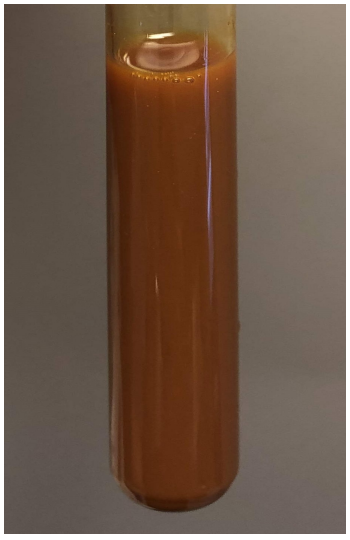

Figure B.1: 0.5 wt.% of Fe_2O_3 without dispersant.

Figure B.2: 0.5 wt.% of Fe_2O_3 with 1.0 wt.% PVP.

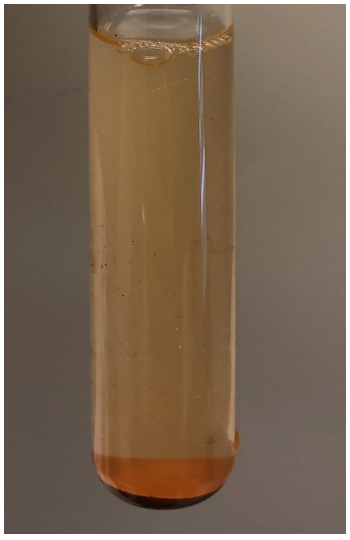

Figure B.3: 0.5 wt.% of Fe_2O_3 with 1.0 wt.% SDS.

Figure B.4: 1.0 wt.% of Fe_2O_3 without dispersant.

Figure B.5: 1.0 wt.% of Fe_2O_3 with 1.0 wt.% PVP.

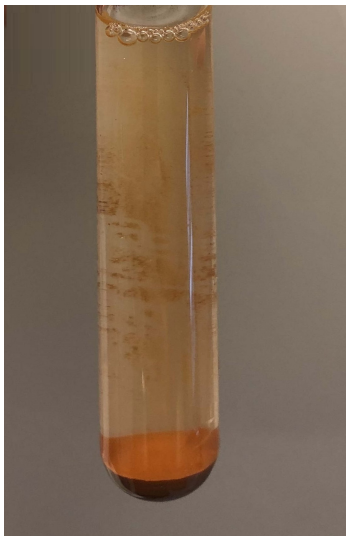

Figure B.6: 1.0 wt.% of Fe_2O_3 with 1.0 wt.% SDS.

Figure B.7: 1.5 wt.% of Fe_2O_3 without dispersant.

Figure B.8: 1.5 wt.% of Fe_2O_3 with 1.0 wt.% PVP.

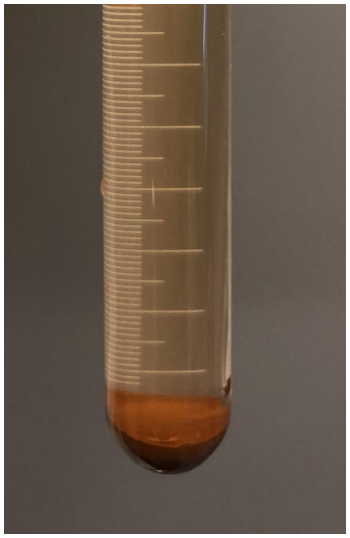

Figure B.9: 1.5 wt.% of Fe_2O_3 with 1.0 wt.% SDS.

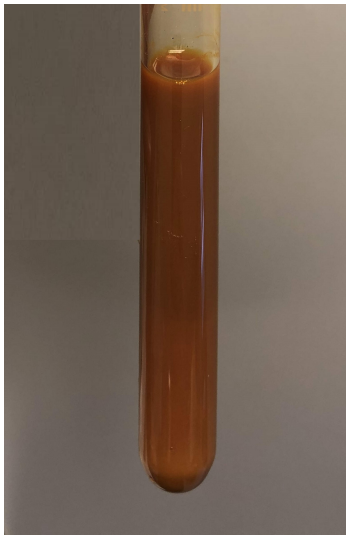

Figure B.10: 2.0 wt.% of Fe_2O_3 without dispersant.

Figure B.11: 2.0 wt.% of Fe_2O_3 with 1.0 wt.% PVP.

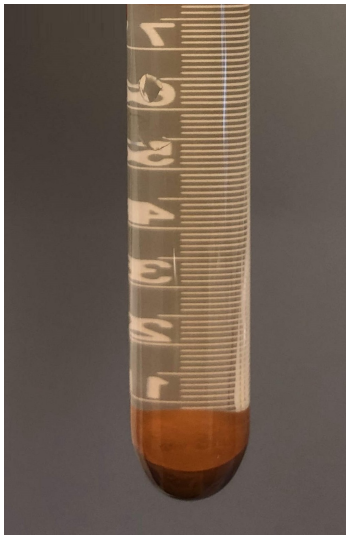

Figure B.12: 2.0 wt.% of Fe_2O_3 with 1.0 wt.% SDS.

B.2 24 hours after sonification

Pictures of the samples 24 hours after sonification.

Figure B.13: 0.5 wt.% of Fe_2O_3 without dispersant.

Figure B.14: 0.5 wt.% of Fe_2O_3 with 1.0 wt.% PVP.

Figure B.15: 0.5 wt.% of Fe_2O_3 with 1.0 wt.% SDS.

Figure B.16: 1.0 wt.% of Fe_2O_3 without dispersant.

Figure B.17: 1.0 wt.% of Fe_2O_3 with 1.0 wt.% PVP.

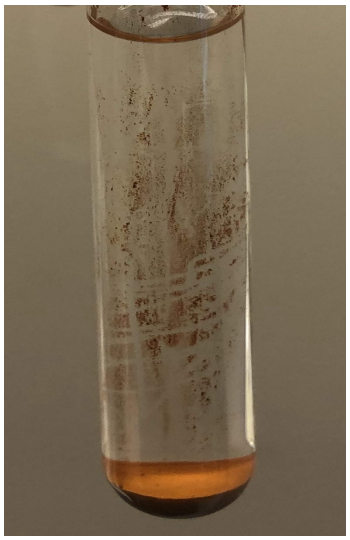

Figure B.18: 1.0 wt.% of Fe_2O_3 with 1.0 wt.% SDS.

Figure B.19: 1.5 wt.% of Fe_2O_3 without dispersant.

Figure B.20: 1.5 wt.% of Fe_2O_3 with 1.0 wt.% PVP.

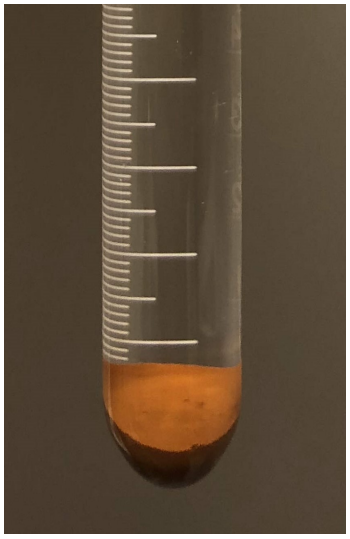

Figure B.21: 1.5 wt.% of Fe_2O_3 with 1.0 wt.% SDS.

Figure B.22: 2.0 wt.% of Fe_2O_3 without dispersant.

Figure B.23: 2.0 wt.% of Fe_2O_3 with 1.0 wt.% PVP.

Figure B.24: 2.0 wt.% of Fe_2O_3 with 1.0 wt.% SDS.

Appendix C

Measured temperatures for the vertical case

C.1 Temperature distribution

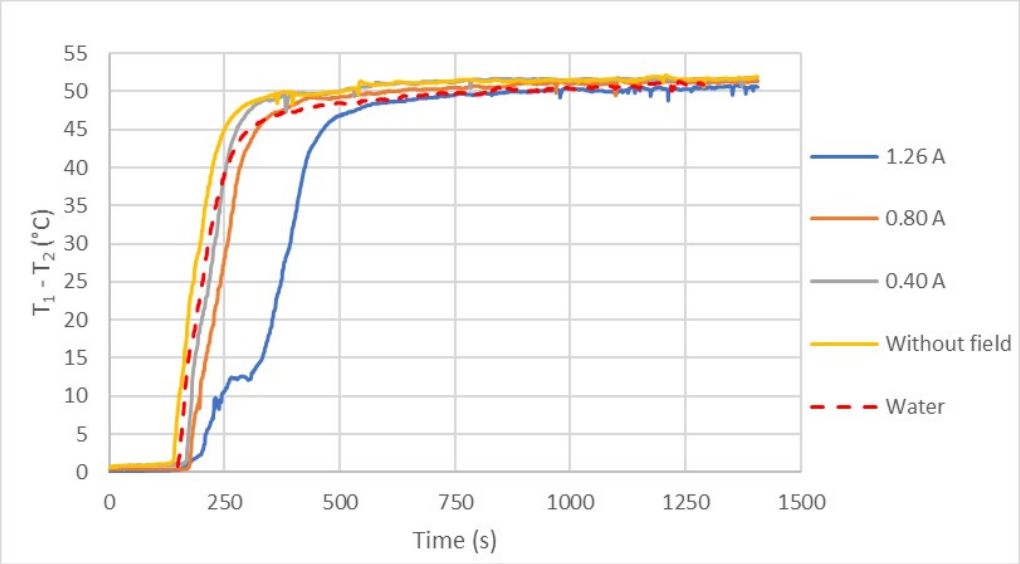

Figure C.1: Temperature differences for the concentration of 0.5 wt.% without and with different solenoid electrical currents.

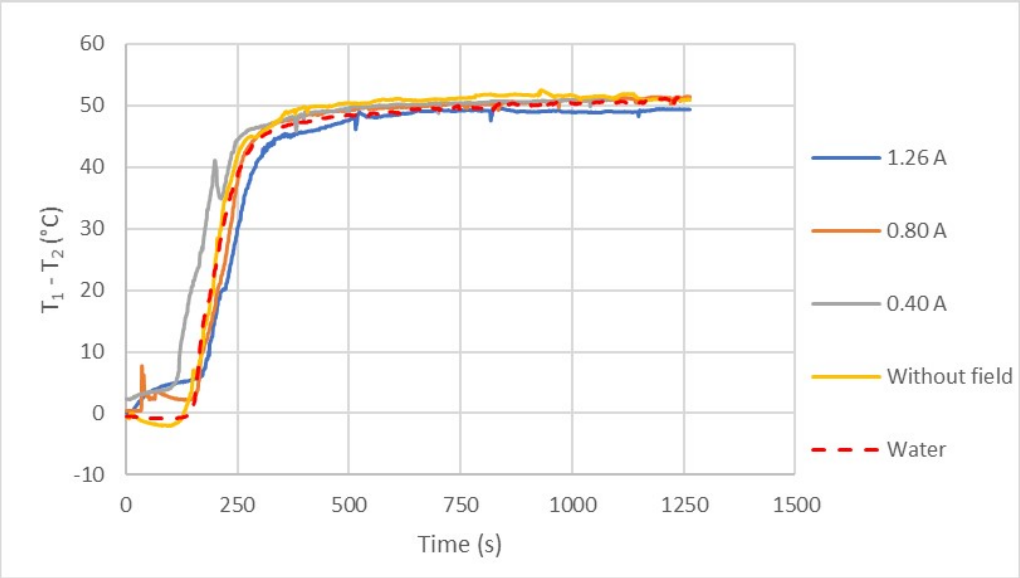

Figure C.2: Temperature differences for the concentration of 1.0 wt.% without and with different solenoid electrical currents.

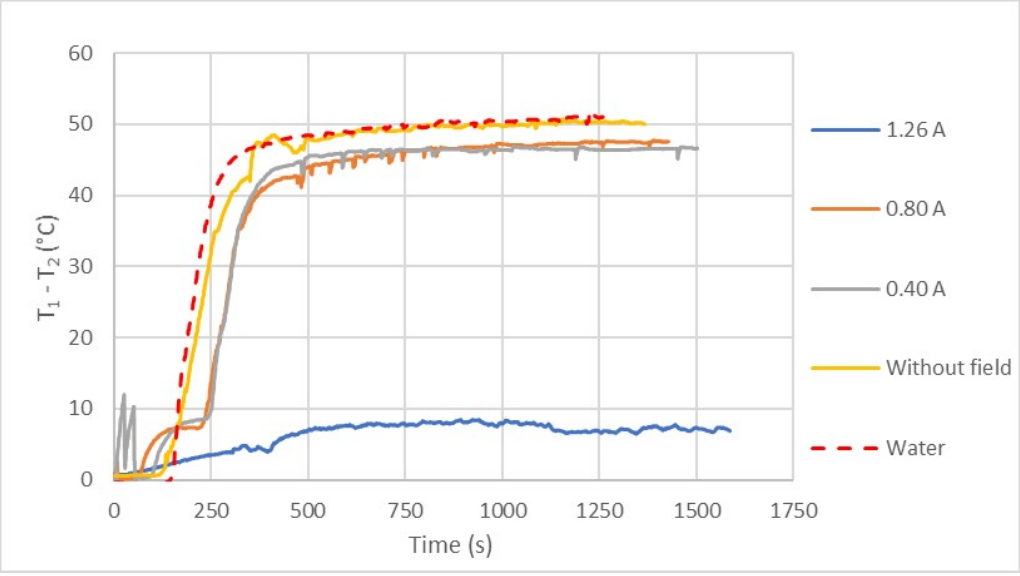

Figure C.3: Temperature differences for the concentration of 1.5 wt.% without and with different solenoid electrical currents.

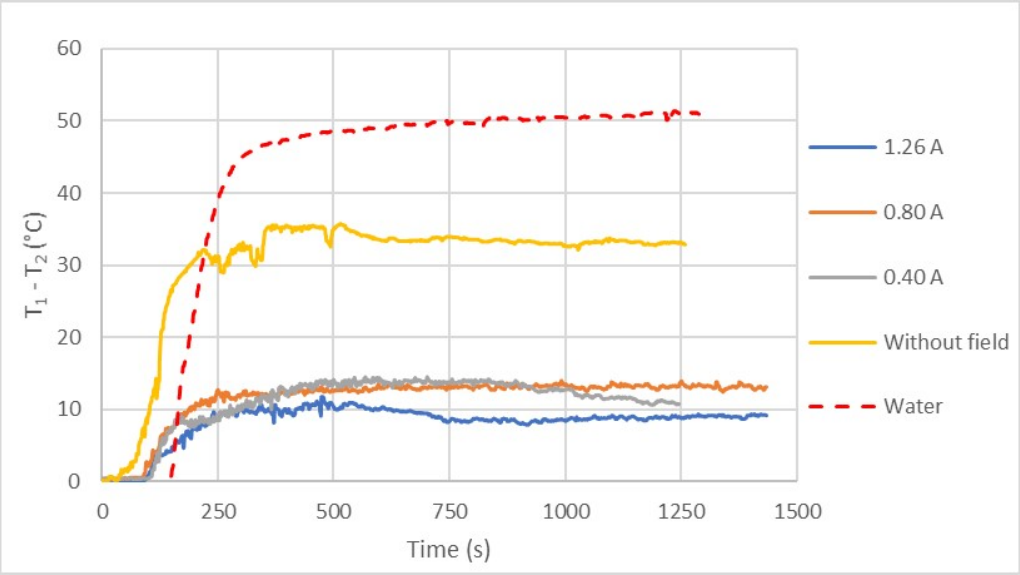

Figure C.4: Temperature differences for the concentration of 2.0 wt.% without and with different solenoid electrical currents.

Appendix D

Additional results from CFD

D.1 Comparison between experimental and simulated temperature differences

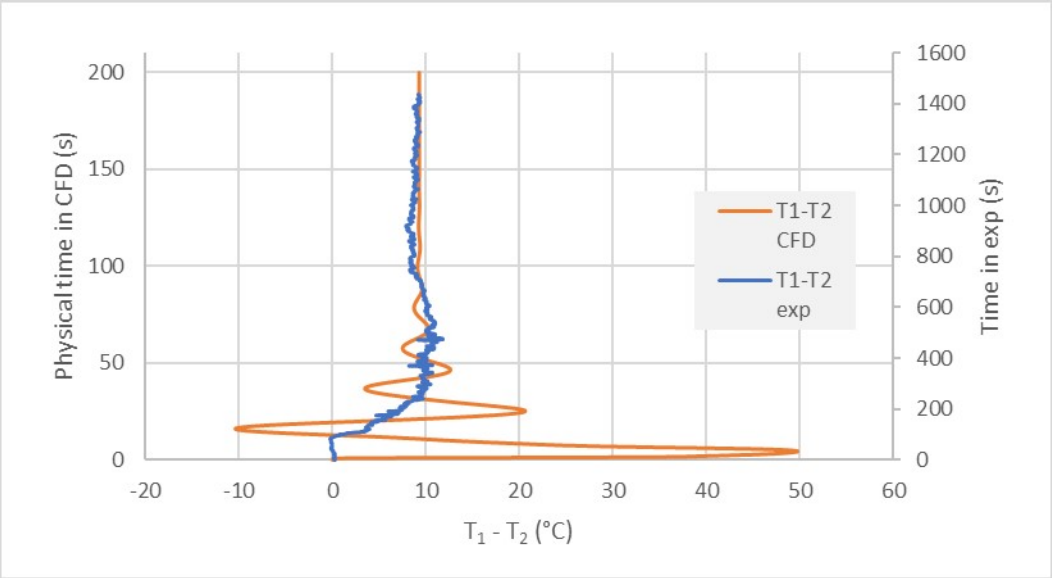

Figure D.1: The simulated and experimental temperature differences over time for 2.0 wt.% of Fe_2O_3 with a solenoid electrical current of 1.26 A.

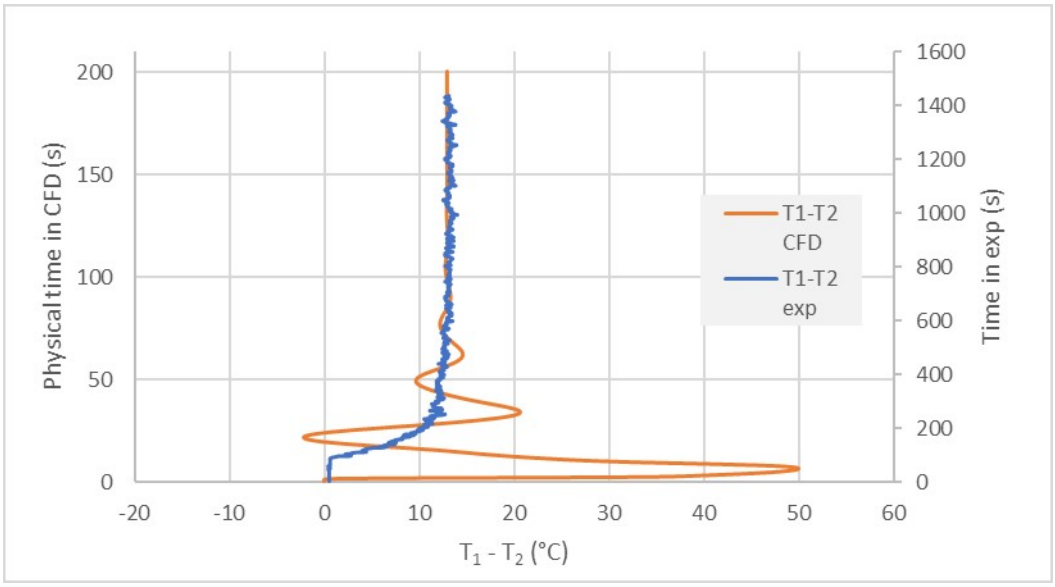

Figure D.2: The simulated and experimental temperature differences over time for 2.0 wt.% of Fe_2O_3 with a solenoid electrical current of 0.80 A.

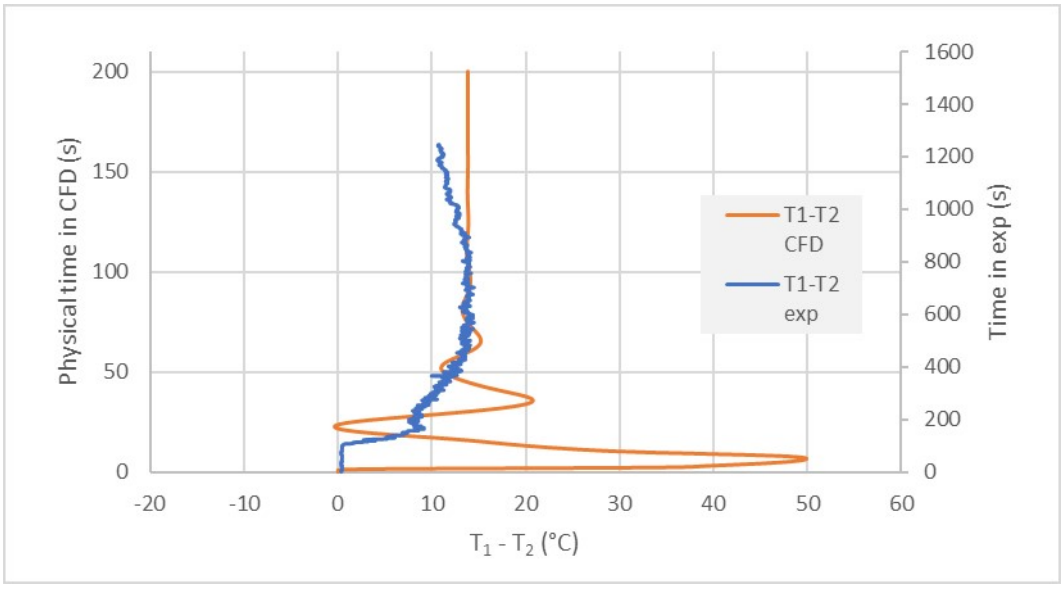

Figure D.3: The simulated and experimental temperature differences over time for 2.0 wt.% of Fe_2O_3 with a solenoid electrical current of 0.40 A.

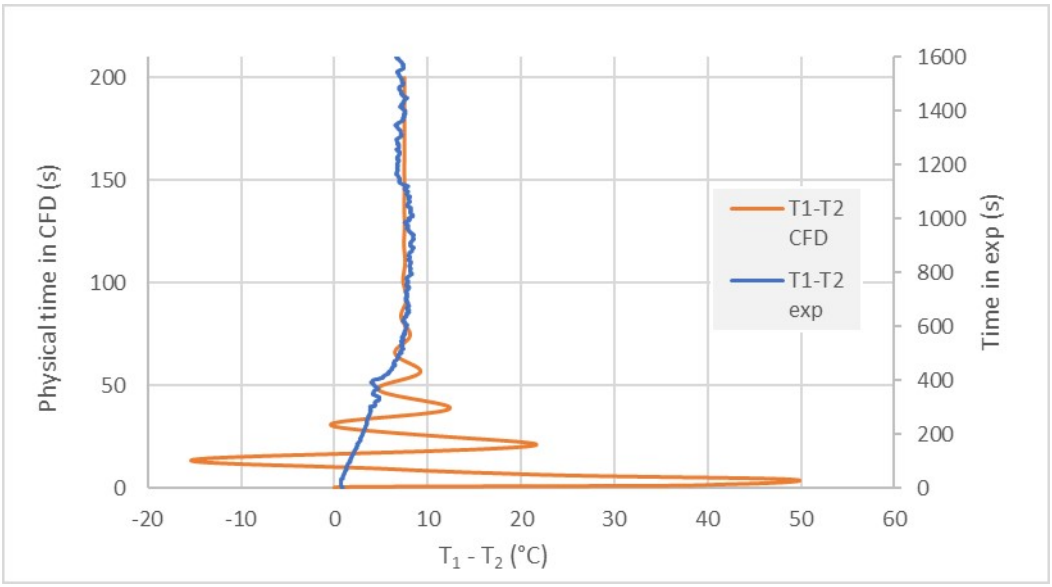

Figure D.4: The simulated and experimental temperature differences over time for 1.5 wt.% of Fe_2O_3 with a solenoid electrical current of 1.26 A.

D.2 Temperature profile

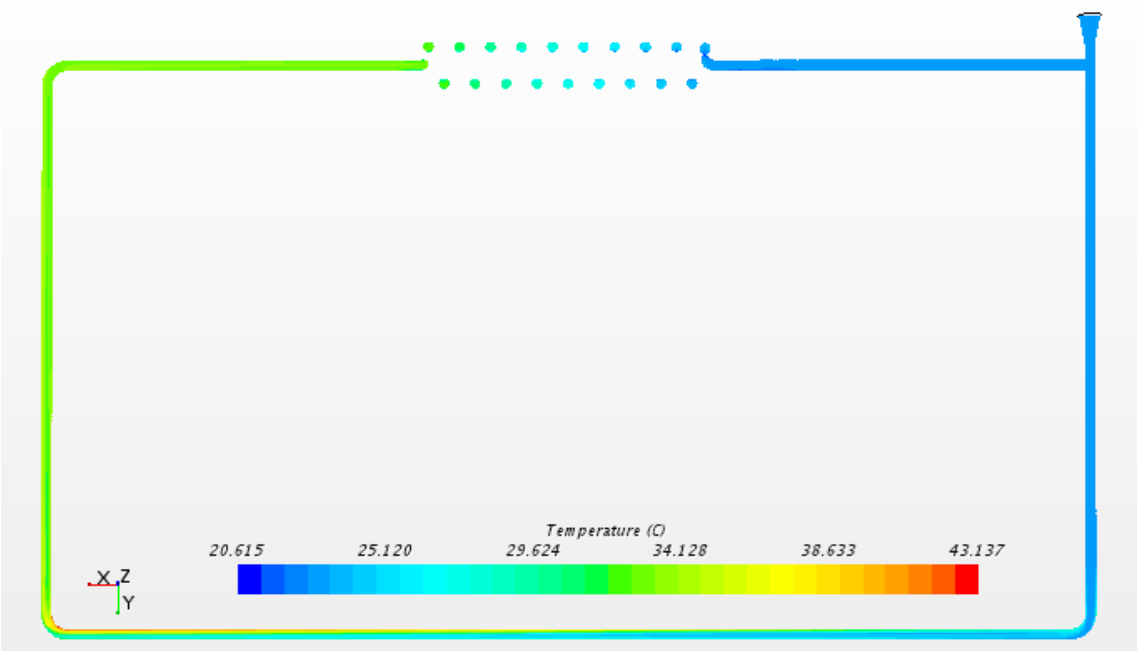

Figure D.5: Temperature profile on the geometry for 2.0 wt.% of Fe_2O_3 with a solenoid electrical current of 1.26 A, after 200 s in physical time in CFD.

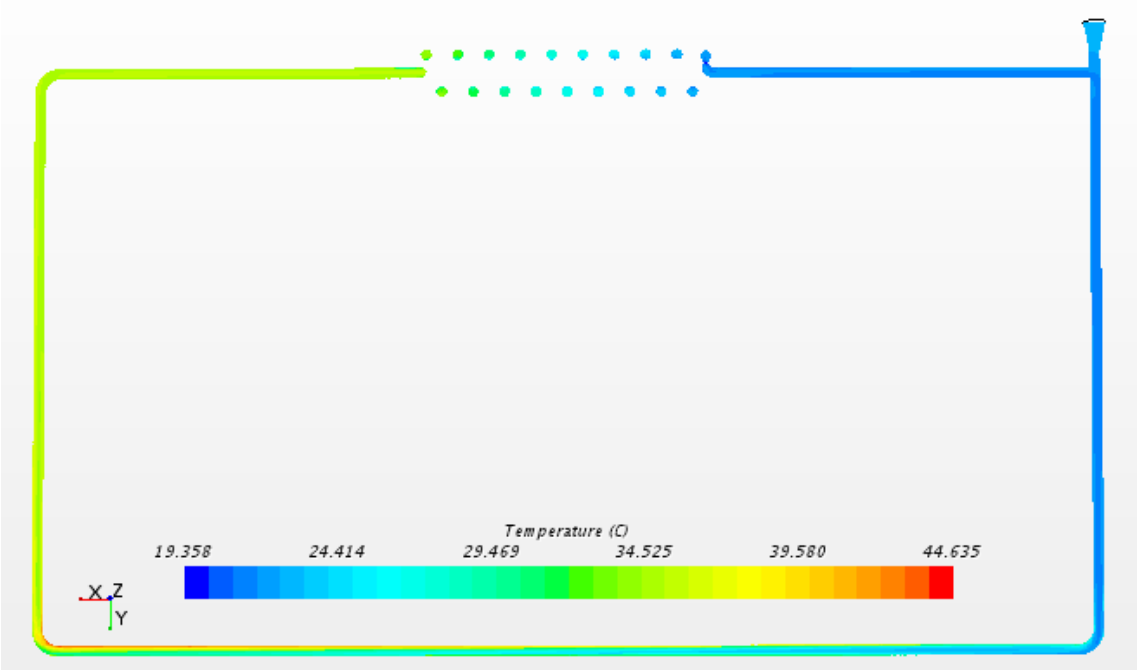

Figure D.6: Temperature profile on the geometry for 2.0 wt.% of Fe_2O_3 with a solenoid electrical current of 0.80 A, after 200 s in physical time in CFD.

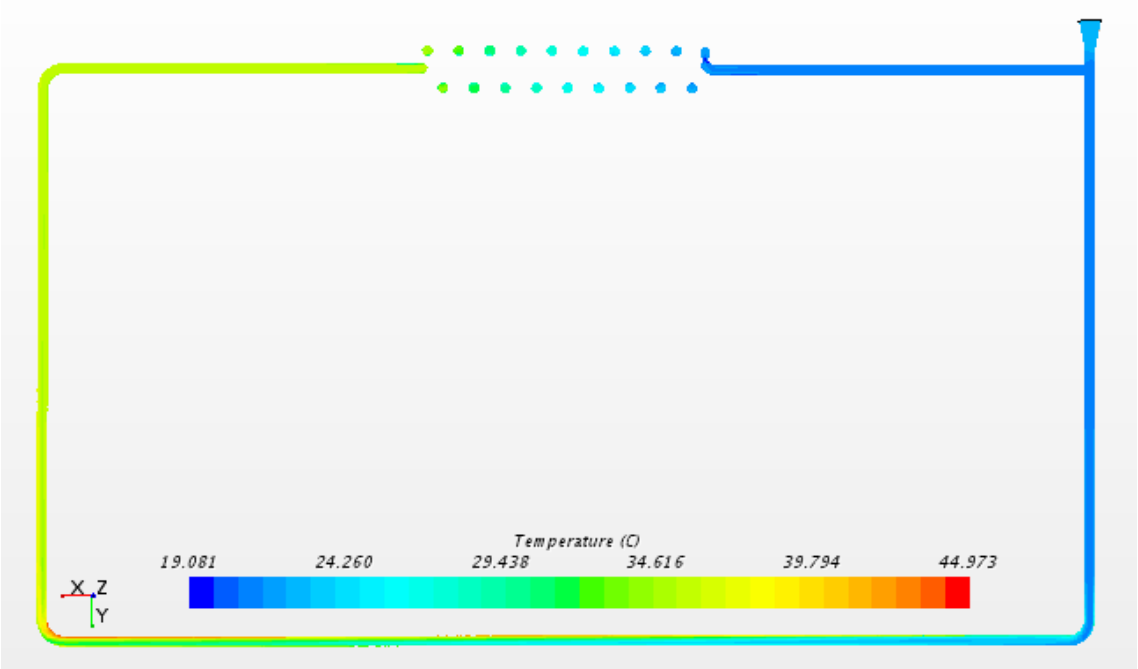

Figure D.7: Temperature profile on the geometry for 2.0 wt.% of Fe_2O_3 with a solenoid electrical current of 0.40 A, after 200 s in physical time in CFD.

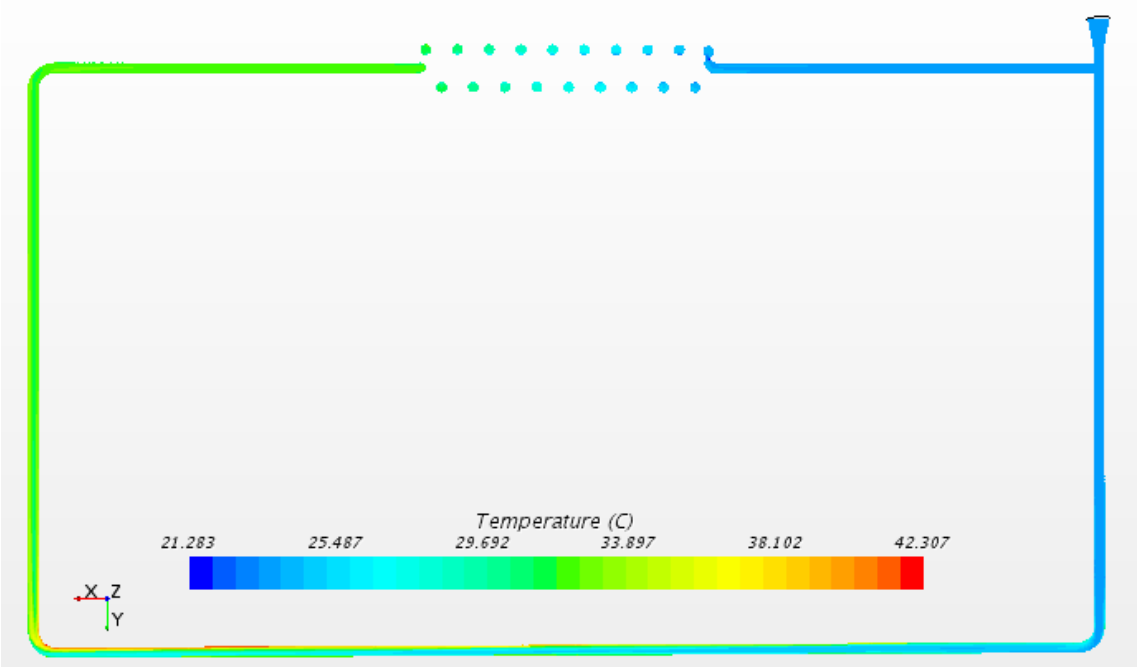

Figure D.8: Temperature profile on the geometry for 1.5 wt.% of Fe_2O_3 with a solenoid electrical current of 1.26 A, after 200 s in physical time in CFD.

D.3 Fluid velocity profile

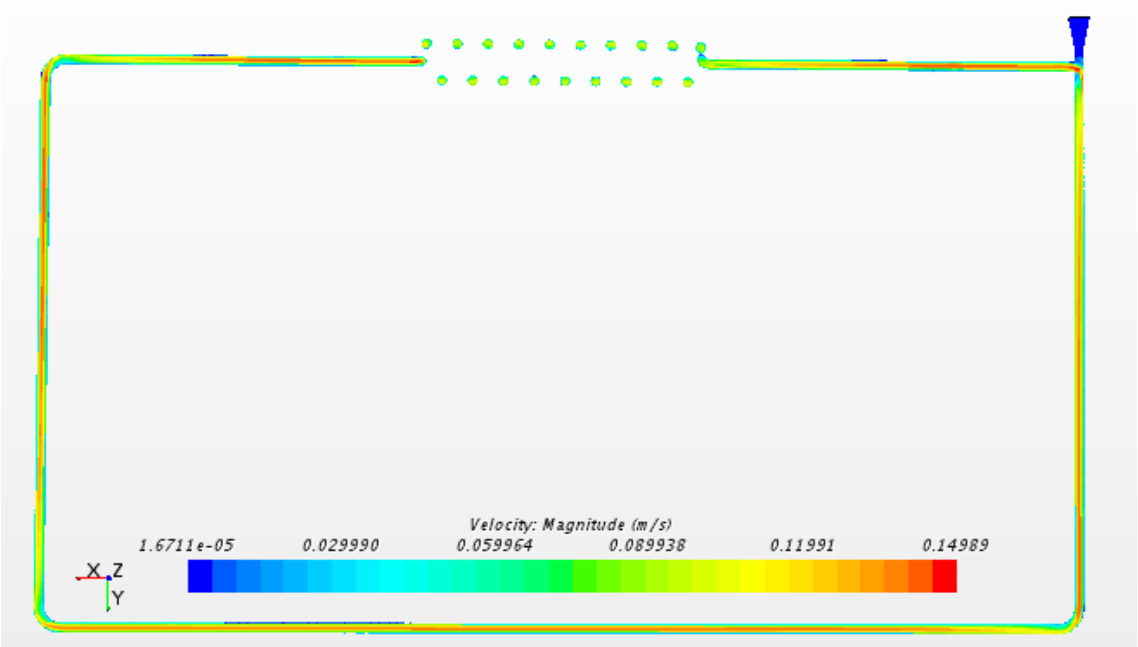

Figure D.9: Velocity profile on the geometry for 2.0 wt.% of Fe_2O_3 with a solenoid electrical current of 1.26 A, after 200 s in physical time in CFD.

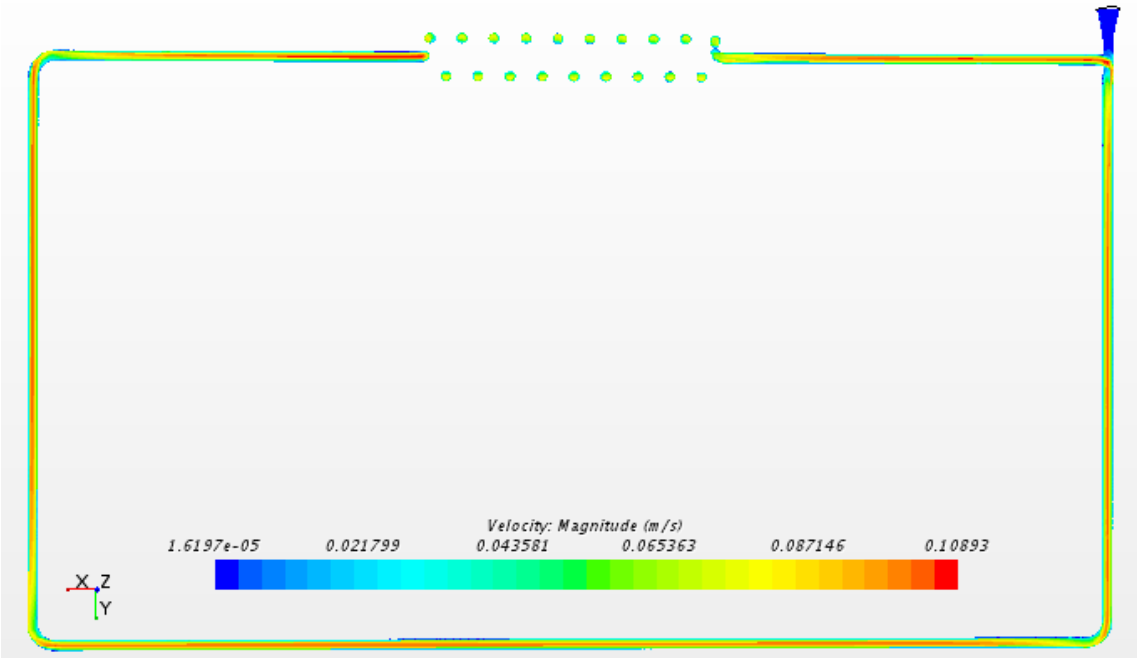

Figure D.10: Velocity profile on the geometry for 2.0 wt.% of Fe_2O_3 with a solenoid electrical current of 0.80 A, after 200 s in physical time in CFD.

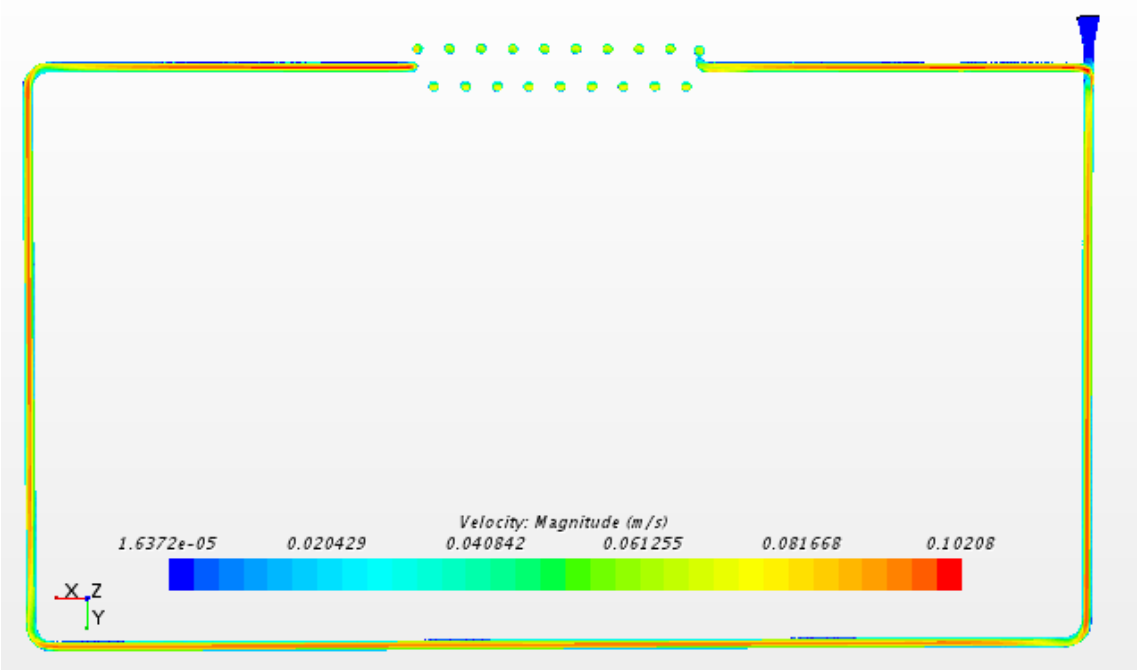

Figure D.11: Velocity profile on the geometry for 2.0 wt.% of Fe_2O_3 with a solenoid electrical current of 0.40 A, after 200 s in physical time in CFD.

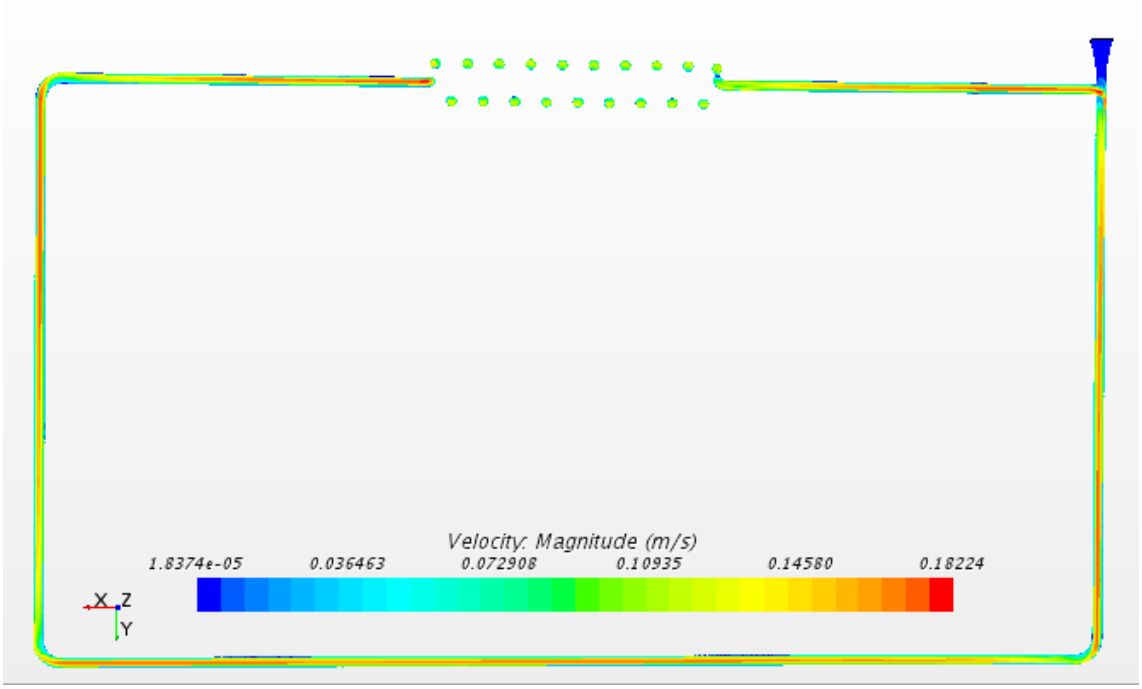

Figure D.12: Velocity profile on the geometry for 1.5 wt.% of Fe_2O_3 with a solenoid electrical current of 1.26 A, after 200 s in physical time in CFD.

Appendix E

Measured temperatures for the horizontal case

E.1 Temperature distribution

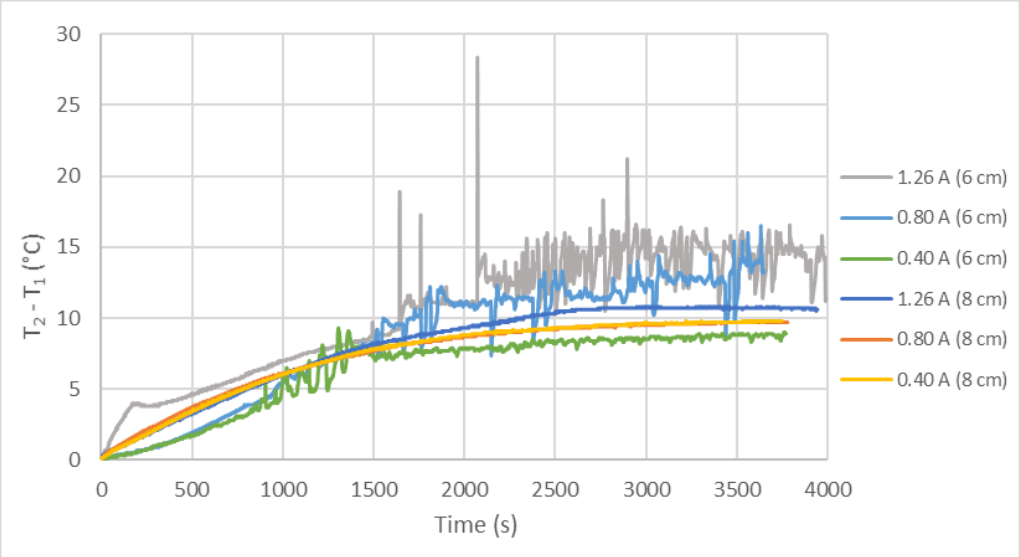

Figure E.1: Temperature differences for the concentration of 0.5 wt.% with different solenoid electrical currents and irradiation distances.

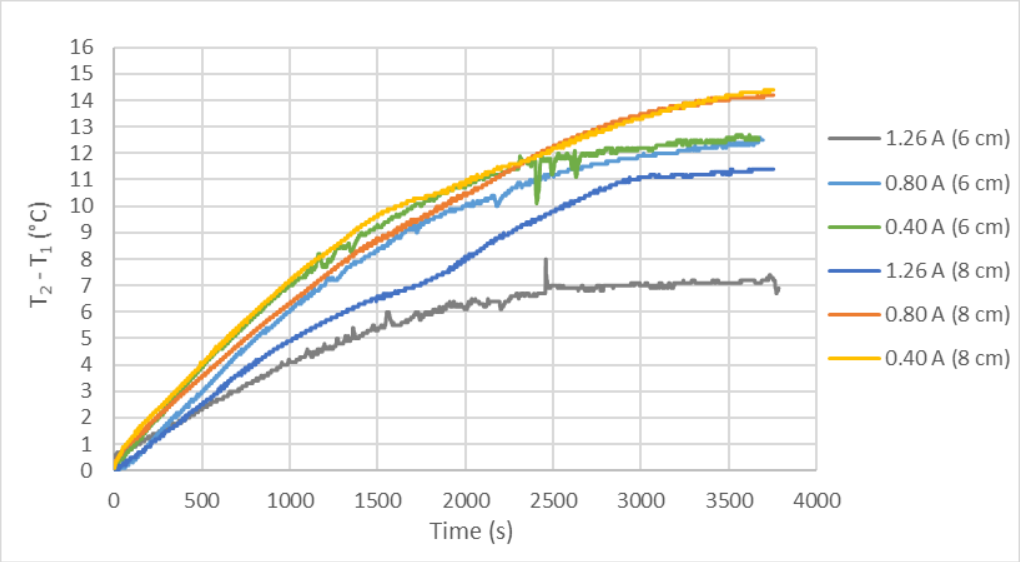

Figure E.2: Temperature differences for the concentration of 1.0 wt.% with different solenoid electrical currents and irradiation distances.

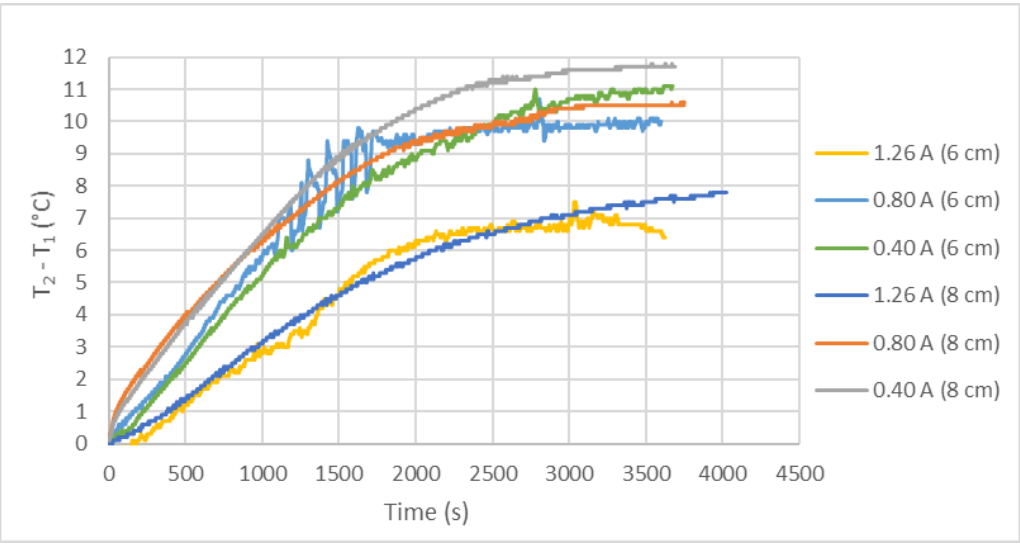

Figure E.3: Temperature differences for the concentration of 1.5 wt.% with different solenoid electrical currents and irradiation distances.

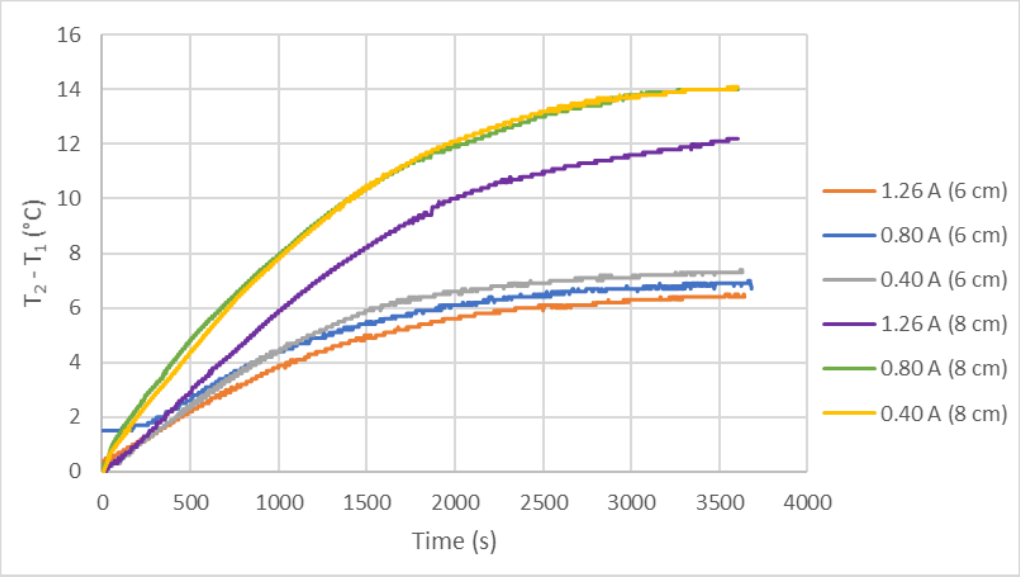

Figure E.4: Temperature differences for the concentration of 2.0 wt.% with different solenoid electrical currents and irradiation distances.